Modeling of Heat Pipes in Steady-State & the Effects of Sloshing

MSc Thesis

Doruk Kural

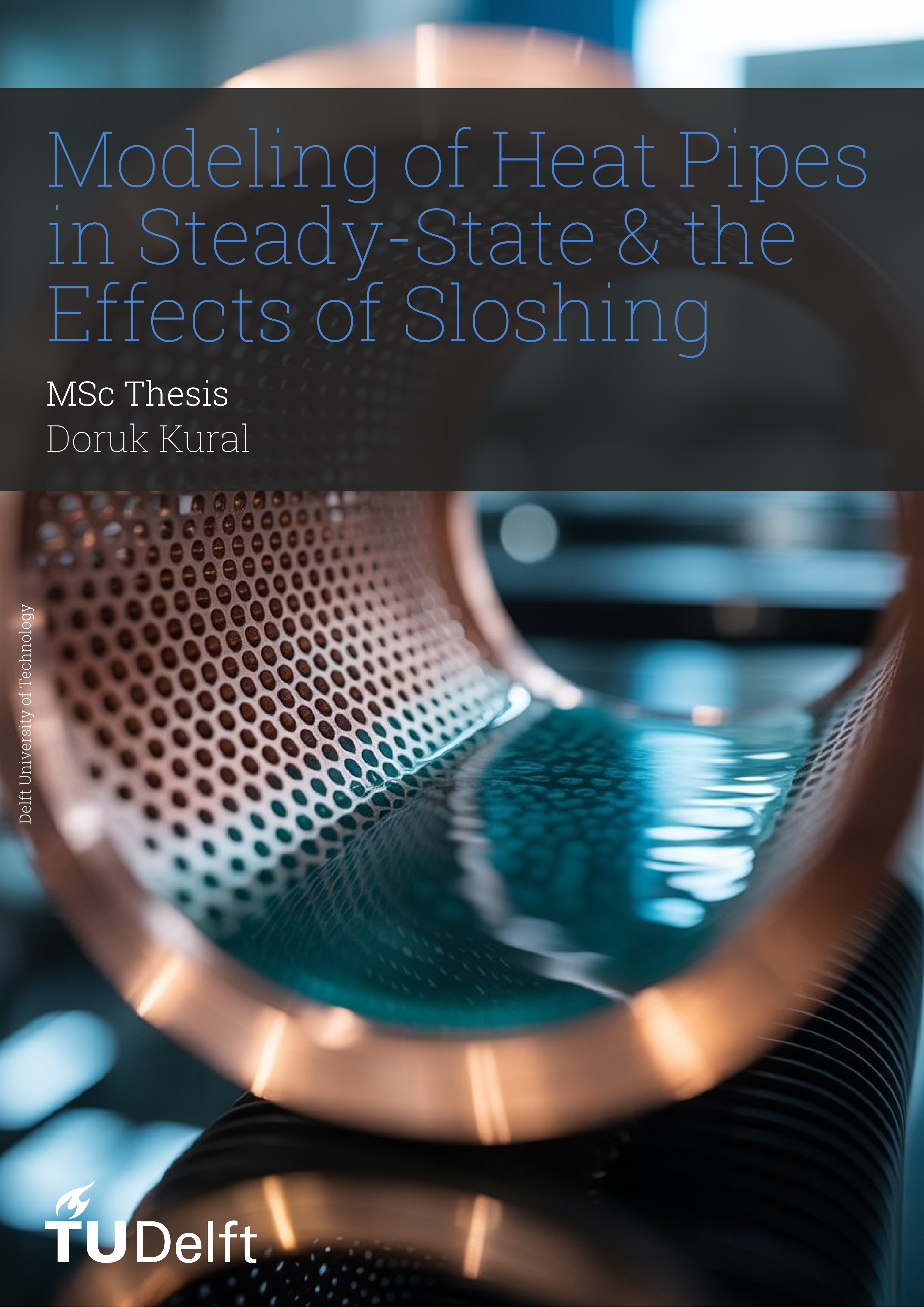

Delft University of Technology

Modeling of Heat Pipes in Steady-State & the Effects of Sloshing

by

Doruk Kural

to obtain the degree **Master of Science**

at the **Delft University of Technology**,

to be defended publicly on Monday December 1st, 2025 at 10:00 AM.

Student Number: 6053742
Thesis Duration: Feb. 3rd – Dec. 1st, 2025
Faculty: Mechanical Engineering
Department: Process & Energy

Thesis Committee:	Dr. Lorenzo Botto	TU Delft, Supervisor
	Dr. Ron van Ostayen	TU Delft
	Dr. Emanuele Zanetti	TU Delft
	Can Tümer	ASML, Supervisor

Cover: Generated by Gen-AI model Nano Banana (2025) by Google DeepMind

Preface

I would like to start by thanking my family for their support through thick and thin, especially in my academic endeavors. To my Mom and Dad, be it my doubts, shortcomings, exams, or my awards, ceremonies, and certificates, you were always there, in every way. For that, I am in debt until the end of time. To my Brother, I thank you for being my guide when I felt like there was no one I could turn to. To my late Grandpa, I learned so much from you, some of which I can not even put into words. I know you would've been incredibly proud of me today, and I promise to do my best to live up to your expectations. To my Grandma, Uncle, Aunts, Cousins, and countless others, I am so glad to have you see me here today, and I wish to share with you all the accomplishments and happiness I am to have in the future.

To all my friends back home: I thank you with my deepest regards. If not for you, I wouldn't be here. You've pushed me, guided me, scolded me, and most of all, made me stand up when I fell. Words are unworthy of the emotions I have for you, so I will carry all of it through my life. To a particular group of people, my fellow P&E students: I thank you for making this journey bearable. Quite to my surprise, in retrospect, it was joyful. I wish all of you the best of success, happiness, and exploration of life.

To the academic staff who contributed to the program in any way, I thank them for their efforts. Every course I have done has left an impact on me, and of course, challenged me beyond my imagination. To Dr. Lorenzo Botto, thank you for the unwavering guidance throughout my thesis; without your help, I could not have done it. To all my colleagues and mentors throughout the internships, I also thank you for being there with me and showing me a glimpse of my future, which I could not be more excited for. I've learned from you immensely, both professionally and about life.

I finally thank everyone who does not fall into these groups. Loved ones who are not family, teachers who are not academic staff, and friends who are not here today. I finally close the chapter on my academic life, and start a new one.

This degree has made me sacrifice a lot of things; for that, I am grateful, as it taught me priceless lessons. If I had the chance to begin this journey from square one again, I would not hesitate, even for a second.

To anyone in doubt, fear, darkness, or hopelessness, I would like to end the preface with a saying that I've heard from my father hundreds of times over the years, which was originally said by the one of the greatest people who ever lived:

"Muhtaç olduğun kudret, damarlarındaki asil kanda mevcuttur." -Mustafa Kemal Atatürk

Doruk Kural
Delft, November 2025

Abstract

This MSc thesis investigates the performance of a sintered-powder wick copper-water heat pipe by focusing on two primary areas: a hypothetical exploration of the inner dynamics under high-acceleration conditions, specifically the effects of sloshing, and the detailed mathematical & computational modeling of its steady-state operation.

The effects of a sloshing motion were analyzed through a series of analytical ”thought experiments.” These investigations defined and modeled potential phenomena, including, but not limited to, pressure-induced liquid ”leakout” from the wick and the re-wetting of the undersaturated wick. A 2D axisymmetric computational model of the heat pipe was also developed in COMSOL Multiphysics for simulating steady-state operation. The model solves the coupled equations for heat transfer and fluid flow, accounting for the solid casing, the liquid-saturated porous wick, and the compressible vapor core.

The dynamic analysis revealed that under high accelerations, significant wick dryness can occur, with its severity being highly dependent on wick permeability. Furthermore, the theoretical results indicate that the leaked liquid can shorten the re-wetting period of the wick, possibly leading to a rapid recovery of thermal performance. The steady-state computational model was also successfully validated against existing literature, demonstrating accurate predictions of temperature, pressure, and velocity profiles.

The study successfully provides a validated steady-state model and a preliminary mathematical framework for understanding the complex physics of sloshing in heat pipes. While the final objective of coupling the dynamic and steady-state models was not achieved, this work lays the critical groundwork for future transient multiphysics simulations of heat pipes.

Contents

List of Figures

List of Tables

Nomenclature

List of Symbols and Definitions

Symbol	**Definition**	**Unit**
A	Area	m^2
a	Acceleration	m/s^2
c	Speed of sound	m/s
c_p	Specific heat capacity at constant pressure	$J/(kg \cdot K)$
D	Penetration depth	m
g	Gravitational acceleration	m/s^2
H	Length of liquid saturated porous medium	m
h_{fg}	Latent heat of vaporization	J/kg
I	Identity matrix	-
k	Thermal conductivity	$W/(m \cdot K)$
K	Wavenumber	m^{-1}
L	Leakout length	m
l	Length	m
M	Molecular mass	kg/mol
$\dot{m}$	Mass flow rate	kg/s
$\dot{m}''$	Mass flux per unit area	$kg/(m^2 \cdot s)$
P, p	Pressure	Pa
$\dot{Q}$	Heat transfer rate	W
$\dot{q}$	Heat flux	W/m^2
R	Universal gas constant	$J/(mol \cdot K)$
R_s	Specific gas constant	$J/(kg \cdot K)$
R_{th}	Thermal resistance	K/W
r	Radial coordinate	m
T	Temperature	K or $^\circ C$
t	Time	s
u	Velocity (r-direction)	m/s
V	Volume	m^3
w	Velocity (z-direction)	m/s
W	Wave amplitude	m/s^2
z	Axial coordinate	m
	Greek Symbols	
α	Accommodation coefficient	$-$
Γ	Ratio of specific heats	$-$
Δ	Change	$-$
ε	Porosity	$-$
ζ	Decay constant	m^{-2}
θ	Contact angle	$^\circ$
κ	Permeability	m^2
λ	Wavelength	m
μ	Dynamic viscosity	$kg/(m * s)$
ρ	Density	kg/m^3
Σ	Growth rate	s^{-1}
σ	Surface tension coefficient	N/m
τ	Shear stress	$kg/(m * s^2)$
ϕ	Angle of inclination	$^\circ$
χ	Characteristic time	s
Ω	Mathematical domain	$-$
$\partial\Omega$	Boundary of a domain	$-$

List of Subscripts and Superscripts

Symbol	Definition
a	Adiabatic section
o	Condenser section
e	Evaporator section
eff	Effective
l	Liquid phase
sat	Saturation condition
v	Vapor phase / vapor core
w	Wick
c	Casing section
we	Wetting phase
nwe	Non-wetting phase
wv	Wick-Vapor interface
wc	Wick-Casing interface
p	Pore

List of Dimensionless Numbers

Symbol	Definition	Formula
A	Atwood Number	$(\rho_l - \rho_v)/(\rho_l + \rho_v)$
Bo	Bond Number	$\Delta \rho g L^2/\sigma$
Ca	Capillary Number	$\mu_{we} u/\sigma$
Kn	Knudsen Number	$\sqrt{0.5\pi\Gamma} \cdot Ma/Re$
M	Viscosity Ratio	μ_{we}/μ_{nwe}
Ma	Mach Number	u/c
Re	Reynolds Number	$\rho u L/\mu$
We	Weber Number	$\rho u^2 z/\sigma$
Z	Compressibility Factor	$PM/\rho RT$

List of Abbreviations

Abbreviation	Definition
CAGR	Compound Annual Growth Rate
CC	Clausius-Clapeyron
CFD	Computational Fluid Dynamics
FEM	Finite Element Method
FOM	Figure of Merit
FR	Filling Ratio
GDP	Gross Domestic Product
GMM	Geometric Mean Model
LU	Lower-Upper
NIST	National Institute of Standards and Technology
ODE	Ordinary Differential Equation
PARDISO	Parallel Direct Solver
PDE	Partial Differential Equation
PIV	Particle Image Velocimetry
RO	Research Objective
RTI	Rayleigh-Taylor Instability
USD	United States Dollar

1

Introduction

1.1. Background & Motivation

Heat pipes are efficient thermal management products, used for their ability to transfer heat over both short and long distances with minimal temperature gradients. These devices utilize the principles of phase change and capillary action, which are crucial in certain applications. The demand for efficient thermal management solutions, such as heat pipes, has increased significantly in engineering and industrial applications in the last few decades and is projected to grow continuously over the next decade. The global market share of thermal management systems is currently estimated to be 17 billion USD, and is expected to become 40 billion USD by the end of 2034, with a compound annual growth rate (CAGR) of 10.1% [1].

Heat pipes require no external power, and have long lifetimes as well as high durability, which make them perfect heat transfer conduit candidates for application areas such as electronics cooling [2], solar thermal collectors [3] [4], and aerospace applications, which are areas that require high-performance operation. A sector where heat pipes are used extensively is the high-tech industry, which employs 10% of the Dutch workforce and makes up 11% of the Dutch economy [5], while making up 9% of the GDP (Gross Domestic Product) of the United States [6] at 2 trillion USD.

These heat transfer devices are made up of a hollow solid pipe with a wick structure on the inner wall of the pipe. This wick is a conduit for liquid flow, and is often made up of a metal such as copper, like the pipe. In the core of the heat pipe, the working fluid operates in a specified temperature range, constantly moving inside the pipe in both liquid and gas phases. The device can be simplified into a schematic, as shown in Figure 1.1, in a horizontal orientation. It consists of three sections, namely the Condenser, Adiabatic, and Evaporator. The Evaporator section is where heat is transferred to the heat pipe during operation. Here, the working fluid is evaporated and turned into vapor through the conduction of heat. As the vaporization causes the local vapor pressure to increase, the vapor starts moving inside the core toward the Condenser, which has lower pressure, carrying the latent heat of vaporization. At the Condenser, the vapor condenses into the working fluid due to the lower temperature and releases the latent heat, which is extracted. The condensed working fluid then moves towards the Evaporator side again through the Adiabatic Section inside the wick, completing the flow cycle.

The performance of these devices is calculated very simply: the temperature drop between the Evaporator and Condenser sections with respect to the heat input to the system, formulated as below in Equation 1.1, which is also known as thermal resistance:

$$R_{th} = \frac{T_{hot} - T_{cold}}{\dot{Q}_{in}} \; [K/W] \tag{1.1}$$

It is also beneficial to understand why these devices are used, as they employ a more complex design compared to a regular metal rod. To simply calculate, a copper rod of 1.6 cm diameter and 25 cm

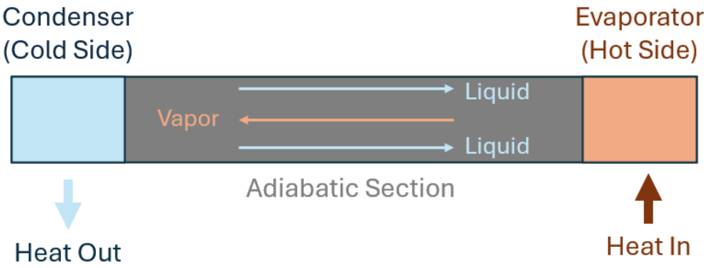

Figure 1.1: Basic heat pipe schematic

length, with a thermal conductivity of 400 $W/(m*K)$ would observe a temperature difference of 78 K on its two ends for an input of 100 W, calculated by Fourier's law of conduction:

$$\Delta T = \frac{\dot{Q} * \Delta x}{k * A} = \frac{100 * 0.25}{400 * \pi * 0.016^2} \approx 78K \tag{1.2}$$

To compare, a sintered wick copper heat pipe with the same dimensions and operating conditions was experimentally measured to have a thermal resistance of 0.2 K/W [7], meaning that the temperature difference would be 20 K, rather than 78 K, resulting in a reduction of approximately 75%.

Another simple comparison would be to compare the specific heat of a liquid versus the latent heat. Water, for instance, at 1 atm and $25°C$ has a specific heat of 4.18 $kJ/(kg*K)$, whereas its latent heat of vaporization is 2.26 MJ/kg. This means that a kilogram of evaporated water can carry more than 4 times the energy of the same amount of water that experiences a temperature increase of $100°C$. This further shows that the phase change phenomenon is a much more efficient way of transferring heat under certain situations, such as the case for the high-tech industry, where efficiency is paramount. The effective thermal conductivity of heat pipes in certain applications can also reach magnitudes over 10^4 $W/(m*K)$ [8], whereas the highest thermal conductivity material found on earth is diamond, with a value of 2000 $W/(m*K)$. These factors make heat pipes incredibly useful in the mentioned industries by combining a low temperature drop, a high thermal conductivity, and an efficient heat transfer method.

The first patented "heat pipe" was designed by George Grover at the Los Alamos National Laboratory in 1963 [9], noting that the device could be of interest in space applications due to its usage of capillary action, where gravitational forces have no effect. In over 60 years of research and improvements, heat pipes have improved drastically. Today, there are dozens of types of heat pipes, such as variable-conductance heat pipes, loop heat pipes, thermosiphons, vapor chambers, etc, and even more alternatives for the wick structures, as well as the material combinations for the working liquid and casing. Although the available research is very thorough, as will be shown later on, the modelling of heat pipes still has more aspects to uncover.

One such aspect is the thermal performance effects resulting from the application of extreme acceleration conditions on heat pipes. This topic is crucial to cover, as applications of heat pipes in certain industries, such as high-speed machinery and aerospace, observe local instantaneous accelerations larger than $40g$'s. At these accelerations, the inner dynamics of heat pipes change drastically compared to their steady state operation conditions. To understand the extent of such effects, studies have been conducted on heat pipes under different acceleration conditions, such as shaking or rotating. One experimental research shows that even under very low accelerations, such as $0.5g$, the thermal resistance of a sintered heat pipe in horizontal configuration increases by 74%, whereas a screen-covered groove heat pipe observes a thermal resistance reduction of 32% [10].

This observation raises the question of "why so?". Currently, there is no state-of-the-art research that can successfully answer this question, and further research is constantly recommended among literature studies to understand the complex underlying physics of this effect. Thus, this thesis aims to aid in filling the gap in the ongoing research on heat pipe technology, focusing on the dynamics of extreme acceleration conditions.

1.2. Research Objectives

This thesis has three research objectives, and considers a sintered-powder wick copper-water heat pipe. The main and ultimate objective is to get the transient model of a heat pipe operating under high acceleration conditions. This final model's aim is to successfully represent the time-dependent response of the heat pipe to externally applied accelerations, giving insight into the thermo-fluid effects of sloshing. This is a very complex objective that requires a multifaceted approach.

To tackle this main objective, the first objective is to define the different possible physical phenomena happening inside a sintered-powder wick under high acceleration conditions. The physics will be defined in terms of flow cases, and they will be carefully defined mathematically and visualized through sketches. The possible resulting thermal effects of these flow regimes will also be discussed. The obtained dynamics must also be incorporated in a robust computational model, such that results can be obtained, which requires a second objective.

The second objective is to first mathematically model the steady-state operation of this heat pipe in an axisymmetric two-dimensional geometry, defining pressure, temperature, velocity, and density fields. This mathematical model is then implemented in a computational model and validated against the literature. This validated and accurate model can be used for future studies and provides a concrete baseline for the implementation of the dynamic effects into a computational model. Under the light of the research objectives, the flowchart of the formulation of the thesis can be shown as in Figure 1.2, and the objectives are briefly listed as follows:

- **RO1**: Define the possible unsteady inner dynamics of sintered-wick heat pipes under high axial accelerations and build mathematical models that capture the relevant physics.
- **RO2**: Build an accurate computational steady-state heat pipe model, validated against literature.
- **RO3**: Couple the two systems to obtain a transient heat pipe model, focused on the dynamic effects of high accelerations and the resulting thermo-fluid effects.

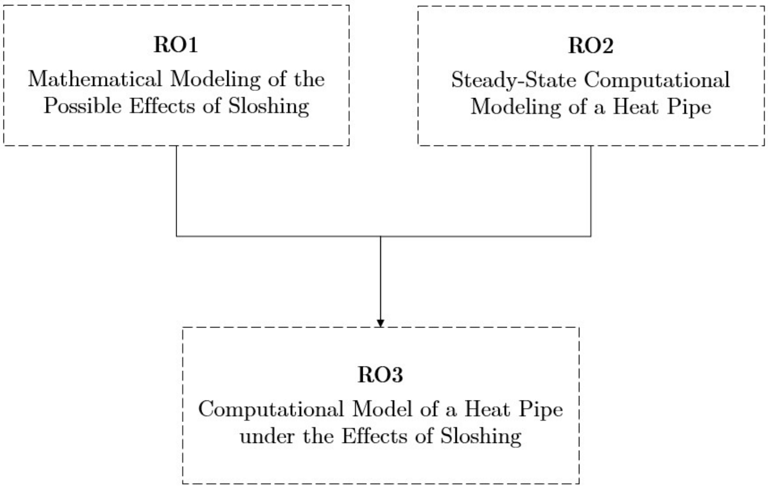

Figure 1.2: Flowchart of the research objectives of the thesis

1.3. Structure of the Thesis

The outline of the thesis is as follows:

- **Chapter 1: Introduction -** This chapter gives a brief background on the topic of heat pipes. Their high thermal conductivity and low temperature drops make them perfect candidates for passive heat transfer devices in industry. The research objectives are defined, following the reasoning of the lack of investigation on the modeling of sloshing in heat pipes.
- **Chapter 2: Overview of Relevant Literature -** Crucial foundations for understanding the physics of heat pipes are laid in terms of fluid dynamics and heat transfer. Theoretical approximations are presented, as well as complex multiphase behavior. Previous literature work done on different heat pipes under various adverse acceleration conditions is presented to obtain an overview of the main problem being investigated.
- **Chapter 3: Description of the Models and Numerical Results -** The first section of the third chapter defines all the thought experiments modeled mathematically throughout the thesis for the extreme condition dynamics and aims to provide a thorough explanation and modeling of each case through sketches. The expected effects on thermal performance are also discussed, along with the important timescales obtained. The second section presents the mathematical and computational model of a heat pipe in steady-state, detailing the governing equations, boundary conditions, and the solution method. Relevant results and validations are also put forward.
- **Chapter 4: Conclusions & Recommendations -** The study's key findings are summarized in the fourth chapter, with possible implications for the research area of heat pipe modeling. The limitations and the scope of the thesis are stated, and the shortcomings are discussed. A set of recommendations for possible future work is finally listed.

2

Overview of Relevant Literature

A more detailed cross-section visualization of a cylindrical heat pipe in a non-horizontal orientation can be seen in Figure 2.1, where the geometrical sections are denoted (condenser, adiabatic, evaporator), as well as the names of the physical domains (casing, wick, vapor core), and the side walls are closed.

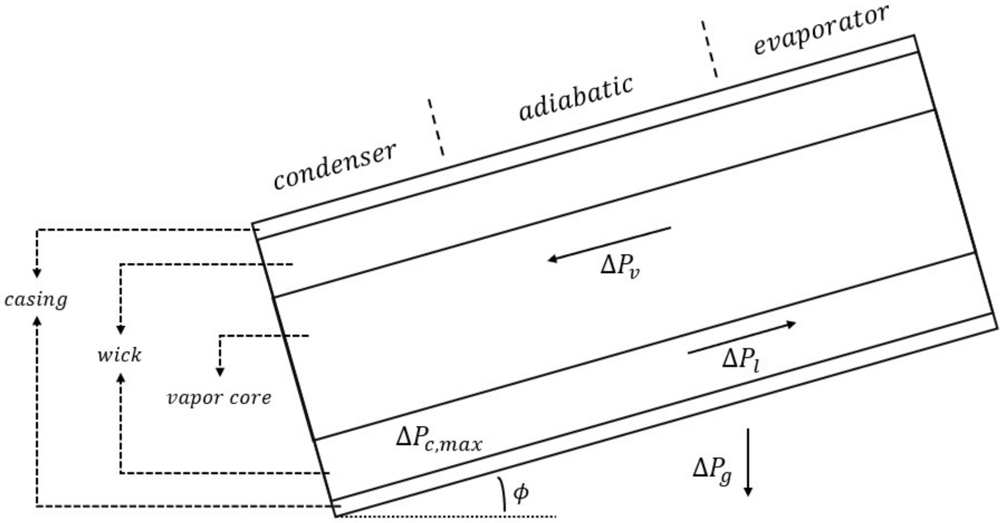

Figure 2.1: Simple cross section of a heat pipe

The overall thermal resistance scheme of a heat pipe can be described as in Equation 1.1. As such, a heat pipe's primary purpose is to transfer a certain amount of heat, $\dot{Q}$, with a corresponding temperature drop, ΔT, between the evaporator and condenser sections. However, it is critical to ensure that the device can operate under the designated conditions. Furthermore, the maximum capillary pressure drop, $\Delta P_{c,max}$ (Pa), must be sufficient to overcome certain pressure drops when moving the fluid phases inside the heat pipe, which can be characterized as:

- ΔP_l: Pumping the liquid through the wick from the condenser to the evaporator
- ΔP_v: Driving the vapor in the core to flow from the evaporator towards the condenser
- ΔP_g: Counteracting (or getting help from) gravitational effects due to the heat pipe orientation

Thus, for correct operation, it can be written that

$$\Delta P_{c,max} \geq \Delta P_l + \Delta P_v + \Delta P_g \tag{2.1}$$

In the case that this condition is not met, the wick will dry out in the evaporator section, and operation will deteriorate, possibly ceasing. This condition is also referred to as the capillary limit of heat pipes, and will be explained later in this section, along with the other operational limits. As heat pipes have multiphysical operation principles, it is appropriate to first explore the fluid dynamics and heat transfer aspects of them separately. In this chapter, the former will be investigated to understand the pressure drop terms and crucial flow regimes based on fluid dynamics theory and literature. The latter will shed light on the central thermal performance characteristic of heat pipes, based on fundamental laws and further literature-based knowledge. The chapter will also delve into research on applying different motion types to heat pipes, showcasing the possible effects of accelerations on heat pipes.

2.1. Fluid Dynamics in Heat Pipes

This section will analyze the pressure terms given in Equation 2.1 for heat pipes, the fundamental working principles of these devices, and how to characterize flow regimes inside porous media, which is a crucial aspect for undersaturated multiphase flows.

2.1.1. Single-Phase Flow in Wicks

Wicks are a crucial component of heat pipes. It is where the liquid phase is transported between the condenser and evaporator sections, such that a continuous supply of molecules is provided for phase change. These wicks can come in many different shapes and designs, with the most popular ones being sintered powder wicks, groove wicks, and compound wicks. Examples for each can be seen in Figure 2.2[11]. The type of wick that the thesis is interested in is a sintered powder wick, which is essentially a porous medium. Porous media are a specific type of media where the solid phase provides a matrix of pathways for one or more fluids to flow through. These pathways are often called voids, and the most defining characteristics of porous media are their porosity and permeability. Porosity, ε, is defined as the ratio of the volume of the voids with respect to the total volume of the medium, and ranges between 0 and 1. Permeability, κ (m^2), is a more intrinsic measure of how well-connected these voids are, and can be imagined as the "conductivity" of the medium. A higher permeability, thus higher conductivity, allows for higher transport rates.

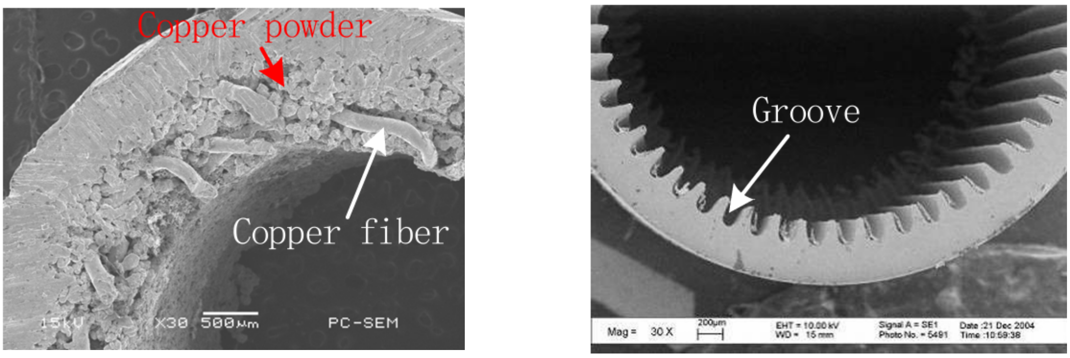

(a) Compound Wick

(b) Groove Wick

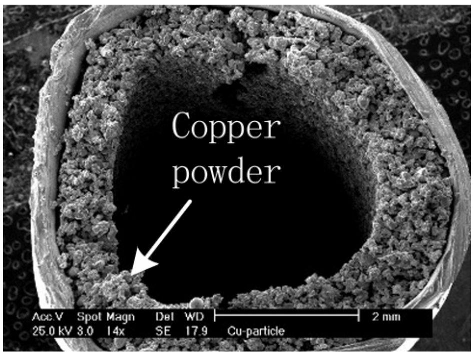

(c) Sintered Powder Wick

Figure 2.2: Different types of wicks [11]

As there is no significant transport of liquid at the end caps (side walls) of the heat pipe, a more applicable length, l_{eff} [12], for calculations is often defined rather than the geometrical length of the heat pipe at optimal operating conditions. It should be noted that the effective length of a heat pipe can vary depending on the operation conditions, for example, the existence of partial dryout in the evaporator can reduce this length. This length is given by $l_{eff} = l_a + (l_o + l_e)/2$, where l_a, l_o, and l_e are the lengths (m) of the adiabatic, condenser, and evaporator sections, respectively. Then, the fluid flow inside this porous medium, with an effective length l_{eff}, must be analyzed. It is often observed that single-phase flow in heat pipe wicks is strictly laminar, creeping, and incompressible, meaning that the material derivative term (i.e., inertial terms) is negligible under the assumption that the Reynolds number, Re, given by $Re = \rho u L/\mu$ is sufficiently low. Here, ρ (kg/m^3) is the fluid density, u (m/s) is the maximum fluid velocity, L (m) is the characteristic length for the system, and μ ($kg/m * s$) is the dynamic viscosity of the fluid. For the above-described assumption to be justifiable, the necessary condition for the Reynolds number is $Re \ll 1$. It should be noted that this condition is not met for every wick-liquid combination, and the simplifications cannot be made, which is not in the scope of the thesis.

Moreover, in incompressible low-Mach flows, Stokes' hypothesis can be applied in most cases for common fluids, which states that the bulk viscosity term can be neglected, further simplifying the Navier-Stokes equations. At low Re, where Stokes's hypothesis applies, the resisting viscous force also varies linearly with velocity (known as Stokes' Drag), used frequently for calculating the drag force on a sphere in a viscous fluid. For isotropic porous media with porosity ε, the permeability tensor has no diagonal terms, and the Navier-Stokes equation finally reduces to Equation 2.2, known commonly as Darcy's Law as

$$\mathbf{u} = -\frac{\kappa}{\varepsilon\mu}\boldsymbol{\nabla} p \tag{2.2}$$

For thin-walled heat pipes, heat transfer through conduction in the wick and casing is significantly lower than phase change heat transfer. This means that the heat input is largely absorbed for phase change; thus, the steady-state mass flow rate can be approximated through $\dot{m} = \dot{Q}/h_{fg}$ $[kg/s]$, where h_{fg} is the latent heat of vaporization for the fluid (J/kg). As the mass flow rate of the fluids inside the system is constant at steady state, it can also be written that the mass change per time across a constant cross-section with a porosity is $\dot{m} = \rho A_f u$. Here A_f is the cross-sectional area of the wick (m^2) for fluid flow, defined as $A_f = A_w\varepsilon = \varepsilon\pi(r_w^2 - r_v^2)$, where r_w and r_v are the radii of the wick and vapor core sections, respectively, and A_w is the wick cross-sectional area. Inserting this expression into Darcy's law, and stating that the pressure gradient in Equation 2.2 is equivalent to the liquid pressure drop along l_{eff}, gives the necessary pressure drop equation

$$\Delta P_l = \frac{\dot{m}\mu}{A\rho\kappa} l_{eff} \tag{2.3}$$

As seen from the equation, the geometry and properties of the wick, as well as the choice of the working fluid, are crucial for heat pipes. There is a wide range of fluids that are used in heat pipes. However, there are certain considerations for these fluids, such as [13]:

- Operating Temperature Range
- Expected Body Force Range
- Material Compatibility

Evidently, heat pipes must operate between the freezing and critical point (where the physical properties of the phases change drastically) for consistent and steady operation as the liquid and vapor phases are utilized in tandem. It is also crucial that the fluid must overcome the body forces such as acceleration and gravity, dominated by the density of the fluid, ρ. This can be done by the fluid through capillary action (which will be explained later), utilizing the surface tension of the fluid, σ. Finally, it is worth considering the system's compatibility and stability as a whole, i.e., if electronics are present, it could be beneficial to consider a dielectric fluid, or non-corrosive and non-erosive fluids if the metal is prone to chemical decomposition.

It is also important to consider the viscosity and latent heat of the chosen fluid too [14]. Viscous forces act against both the liquid and vapor flow in the heat pipe. The evaporated vapor must overcome viscous forces such that it can move towards the condenser, and this is especially difficult at lower temperatures, which causes startup problems. Jang and Faghri [15] have shown in their paper that a small heat input at the condenser section helps solve startup problems from a frozen state, as the inside of a heat pipe is initially in a vacuum. Viscosity also counteracts the capillary forces inside the wick, which surface tension must also overcome. The latent heat of the fluid is also crucial as this governs the amount of heat the vapor phase can carry per weight, limiting the heat transfer capacity [16]. To combine all of these properties of the working fluid and understand the different behaviors of the available options, Reay et. al. [12] present an expression for the figure of merit for choosing a fluid when designing a heat pipe, FOM, given by

$$FOM = \frac{\rho \sigma h_{fg}}{\mu} \quad [W/m^2] \tag{2.4}$$

For an optimal heat pipe design, the aim must be to maximize this value (assuming vapor and gravitational pressure drops are negligible), and as these properties for fluids are functions of temperature, calculating this value along the operable temperature ranges is necessary, as seen below in Figure 2.3.

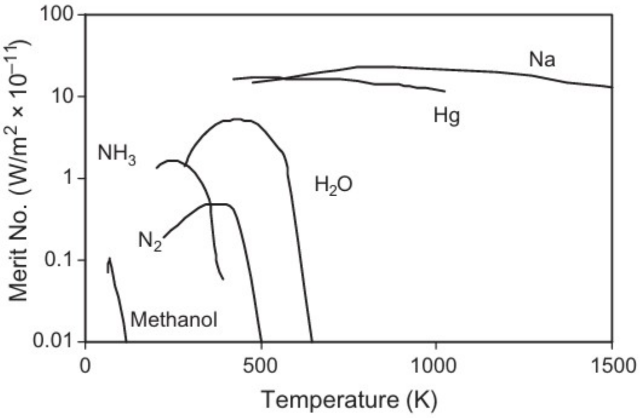

Figure 2.3: Merit number of certain fluids [12]

As seen from the figure, it is evident that some of the most common working fluids are ammonia [17] (NH_3), water (H_2O), and, in some high-temperature cases, sodium (Na) [18]. It is re-emphasized that the working fluid must be compatible with the heat pipe wick/casing material. Certain combinations can lead to corrosion and degradation over time, such as the case for an aluminium-water heat pipe operating at high temperatures, which is reported to be incompatible by Reay [19]. For more detailed fluid-solid combinations regarding heat pipe design, Table 3.3, page 184 in Zohuri's book [13] is recommended.

As mentioned, observing Equation 2.3 shows that the permeability of the wick is a crucial aspect of the pressure drop, with an inversely correlated relationship. This is expected, as a less permeable (i.e., less conductive) medium requires a larger gradient to supply sufficient flux. For a random packing of perfect spheres, with an example being Figure 2.2c, the permeability is calculated by the semi-empirical Kozeny-Carman equation throughout the literature of heat pipes with sintered wicks by

$$\kappa = \frac{\varepsilon^3 r_p^2}{37.5(1-\varepsilon)^2} \tag{2.5}$$

This shows that the permeability of a sintered wick is strongly connected to its porosity, as well as the size of the pores. Thus, when choosing or designing a wick, these two parameters must be considered carefully for the permeability of the wick, which might not be known straight away. Depending on the application, different wick types, some shown in Figure 2.2, might be more beneficial and must be selected correctly.

2.1.2. Multiphase Flow in Porous Media

So far, the flow inside the porous medium was considered to be single-phase. However, for heat pipes, this might not be the case at all times. The filling ratio, FR, of a heat pipe is how saturated the porous medium is, given by $FR = V_{fluid}/V_{pores}$, where V_{fluid} $[m^3]$ is the volume occupied by the liquid phase and V_{pores} $[m^3]$ is the total available volume in the porous medium.

Most often, when two fluids are inside a porous medium, one phase is denoted as the invading (wetting, subscript we) phase, and the other as the defending (non-wetting, subscript nwe) phase. The invading phase has a higher viscosity, which saturates the porous medium with its own molecules. The defending phase acts against this increasing saturation, and the result is the formation of an interface between the two fluids. This interface can have many different shapes, and the main categories are described as capillary fingering, viscous fingering, and stable displacement. The shape mainly depends on two dimensionless numbers, Ca and M. $Ca = \mu_{we}u/\sigma$ is the capillary number, which compares the effect of viscous forces against surface tension forces, where σ (kg/s^2) is the surface tension coefficient. M is the viscosity ratio of the two fluids, given by $M = \mu_{we}/\mu_{nwe}$. The combination of the two numbers represents the possible flow regime in porous media.

These regimes were categorized initially by Lenormand et. al. [20] in 1988, and their results are still used throughout the literature. More recent studies by Hu et. al. [21] and Zhang et. al. [22] have aimed to define the zones more definitively through rigorous experimentation and numerical studies. Lyu et. al. [23] have visualized these zones while conducting their own study, as seen in Figure 2.4.

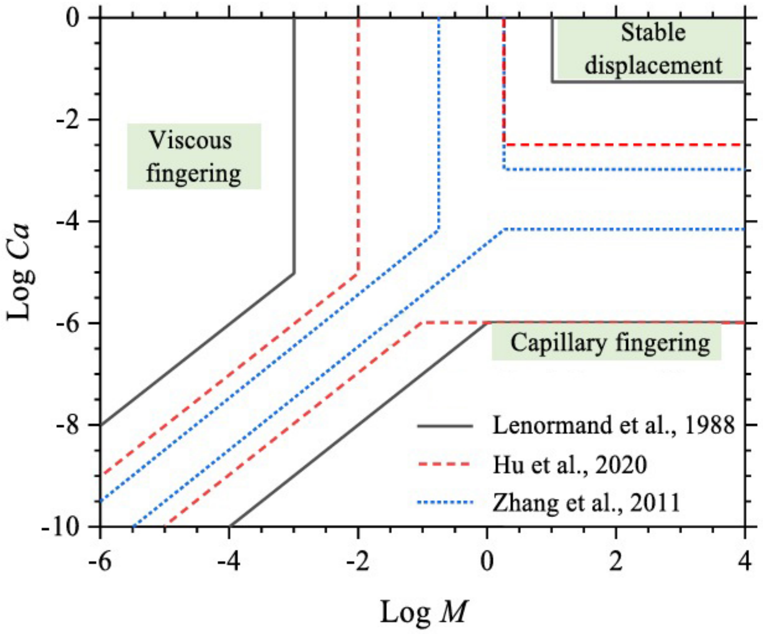

Figure 2.4: Capillary number and viscosity ratio on multiphase porous media flow [23]

These flow regimes and the transition between them were investigated experimentally by Nishizawa et. al. [24], shown in Figure 2.5. For two values of constant M, they investigate changing Ca. This is essentially moving vertically on a line at two different M values. Their results show very clear transition profiles between characteristic flow regimes, especially pronounced for stable displacement.

Seen from the figure, the change from stable displacement to the fingering regimes is very drastic. Investigating the first row of Figure 2.5, a viscous moving front at a high M starts developing a capillary penetration profile when the surface tension forces start dominating the viscous forces (Ca becomes smaller). Still, a more or less defined front is observed at very low Ca. The effect is more visible when starting from a low M in the second row, while reducing Ca. The viscous fingers due to low viscosity wetting phase is again overtaken by capillary action at low Ca, however, this time, as the wetting phase viscosity is low, the same capillary fingering regime is observed at a higher Ca. The last

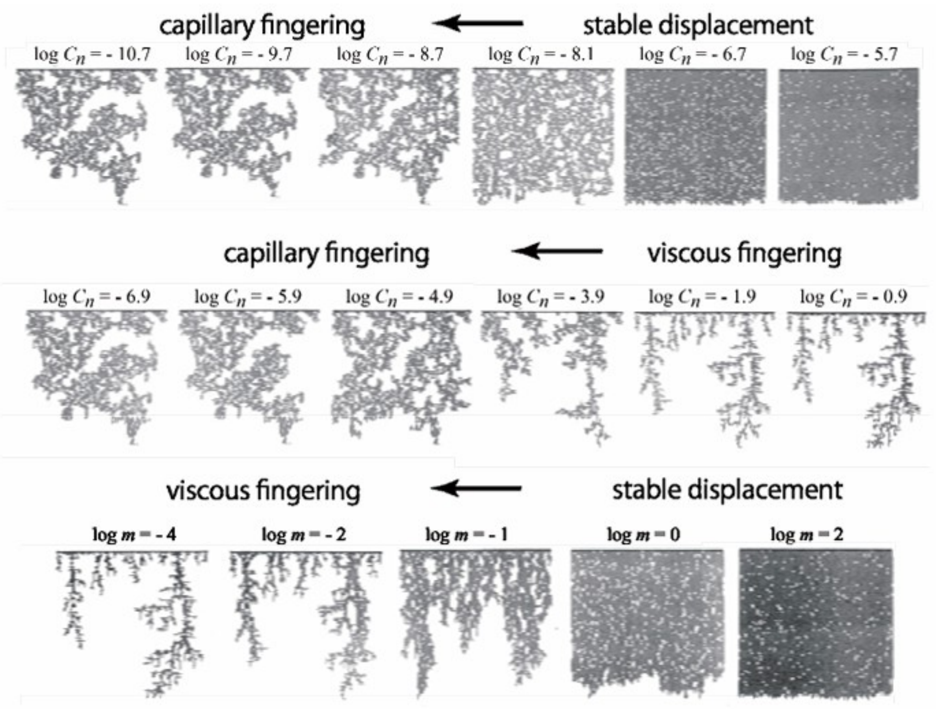

Figure 2.5: Multiphase flow types in porous media and transition profiles [24]

row shows that for high Ca, a reducing M visibly shows how much the stable front disappears, and it becomes difficult to define a single interface.

A study by Zhao et. al. [25] experimentally investigated the injection of water into a porous medium containing silicone oil. The porous medium was a wafer with 100 μm gaps, having a porosity of 0.45 and permeability of $2.4 \cdot 10^{-10}$ m^2. They also investigated the effect of the contact angle, θ, defining it from strong drainage (high contact angle) to strong imbibition (low contact angle). At a combination of $Ca = 3 \cdot 10^{-3}$, $M = 340$, and $\theta = 60°$, their results showed an interface strongly resembling a mixture of stable displacement and capillary fingering, seen in Figure 2.6 with high saturation of the invading phase. Their results also resemble the findings of Nishizawa [24], focusing on the 4^{th} image from left to right on the top row in Figure 2.5, although their values do not match exactly.

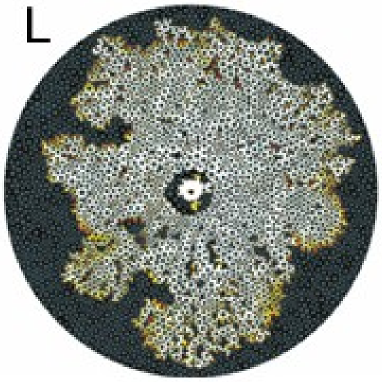

Figure 2.6: Flow for $log(Ca) = -2.52$, $log(M) = 2.53$, and $\theta = 60°$ [25] (White color represents the invading phase (water) at full saturation, with the saturation reducing towards a reddish color. Dark blue represents the defending phase (oil))

These findings show that it is important to understand the possible flow regime inside a porous medium when a multiphase flow is expected. For the case of heat pipes, a filling ratio of less than 100% most often will lead to multiphase flow, which must be correctly modeled, depending on the case.

2.1.3. Hydrostatic Pressure

A tube filled with a liquid experiences a pressure at the bottom of the tube, defined as hydrostatic pressure, also known as Pascal's law. In heat pipes, the pressure drop due to gravity can be negative, positive, or zero, depending on the vertical distance between the condenser and evaporator sections. This pressure difference is defined as

$$\Delta P_g = \rho_l g l \sin\phi \tag{2.6}$$

where ρ is the liquid density, g is the gravitational acceleration (9.81 m/s^2), l is the heat pipe length (m), and ϕ is the angle between the heat pipe and the horizontal axis, which is positive when the condenser is lower than the evaporator (as seen in Figure 2.1), such that a larger capillary pressure drop is required when the liquid must be pumped against gravity.

It is often observed in heat pipes that when the evaporator is below the condenser, the inverse of the configuration shown in Figure 2.1, performance becomes significantly enhanced. As the heat pipe must pump the liquid from the condenser to the evaporator, the assistance of gravity in such a vertical orientation becomes crucial, especially when the heat pipe length is large. In some heat pipes, this body force induced by gravity is the main method of pumping the liquid, which essentially replaces the requirement for a wick. Such heat pipes are called gravity-assisted heat pipes, or more popularly known in industry as thermosiphons.

2.1.4. Vapor Pressure Drop

The analysis of the vapor phase in heat pipes is one of the most crucial points. The flow characteristics must be investigated carefully, along with the pressure drop, and if necessary, the effects of compressibility must be taken into account. The total pressure drop ΔP_v inside the vapor core can be set as equivalent to the separate pressure drops in the evaporator, adiabatic, and condenser sections, namely ΔP_{ve}, ΔP_{va}, and ΔP_{vo}. These pressure drops will be investigated separately, such that a final single equation can be written. The first step is to calculate the radial Reynolds number in the evaporator section, given by $Re_r = \rho_v u_r r_v / \mu_v$. This specific Reynolds number allows one to understand the initial flow regime of the vapor when it changes phase and exits the surface of the wick. This value was found to fundamentally govern most of the pressure changes inside a heat pipe by multiple researchers, as will be shown in Figure 2.3. Here, u_r is the radial exit velocity at the evaporator surface, which can also be calculated as (assuming evaporation occurs uniformly, and only at the evaporator) $u_r = \dot{m}/2\pi\rho_v r_v l_e$. When this expression is inserted into the previous approximation $\dot{m} = \dot{Q}/h_{fg}$ and combined with the radial Reynolds number, it becomes $Re_r = \dot{Q}/2\pi l_e \mu_v h_{fg}$. The value and range of this dimensionless number, which affects the pressure drop calculations, will be explained later in this section.

The first pressure drop term to investigate is in the evaporator section. The vapor leaving the wick interface must be accelerated such that an axial flow into the core is sustained. As the initial vapor has no velocity, and then reaches a velocity u in the axial direction, the pressure required to accelerate the flow is simply given by $\rho_v u^2$. The accelerated flow then becomes a developed flow along the core, and results in a Hagen-Poiseuille type of pressure drop, $4\mu_v \dot{m} l_e / \pi \rho_v r_v^4$. Here, the coefficient that is typically 8 is 4, which is caused by following the same reasoning as taking into account the effective length of sections where certain characteristics are stabilized. Assuming the fully developed incompressible laminar flow continues along the adiabatic section, the pressure drop is again calculated by the Hagen-Poiseuille equation. If the flowing vapor is perfectly decelerated (full pressure recovery) in the condenser section from u to stationary at the interface, a similar approach as the evaporator section is followed. Combining these equations gives the final pressure drop inside the vapor core for incompressible, laminar, complete pressure recovery flow as

$$\Delta P_v = \Delta P_{ve} + \Delta P_{va} + \Delta P_{vo} = \frac{8\mu_v \dot{m}}{\pi \rho_v r_v^4} l_{eff} \tag{2.7}$$

This equation is essentially the viscous pressure drop along a cylindrical pipe with length l_{eff}, which is the Hagen-Poiseuille equation. Cotter [26] states this equation strictly holds for $Re \ll 1$. He further shows that for $Re_r \gg 1$, full pressure recovery is realistically not possible due to the different flow profiles at the evaporator and condenser sections, like end effects when the flow is not decelerated enough, leading to a certain build-up of vapor mass at the end of the heat pipe in the condenser section. He then shows that the coefficient of the inertial term ($\rho_v u^2$) becomes $4/\pi^2$ in the condenser section, recovering approximately 40% of the initial inertial pressure drop at the evaporator, resulting in Equation 2.8. The comparison between full recovery and Cotter's partial recovery calculations can be visualized as seen in Figure 2.7. It is also interesting to observe that the lengths of the evaporator/condenser sections are irrelevant for the pressure drop/recovery in Cotter's formulation, which reduces its applicability as he assumed the sections to be equal in length.

$$\Delta P_{v,Cotter} = \left(1 - \frac{4}{\pi^2}\right) \frac{\dot{m}^2}{8\pi\rho_v r_v^4} + \frac{8\mu_v \dot{m}}{\pi\rho_v r_v^4} l_a \tag{2.8}$$

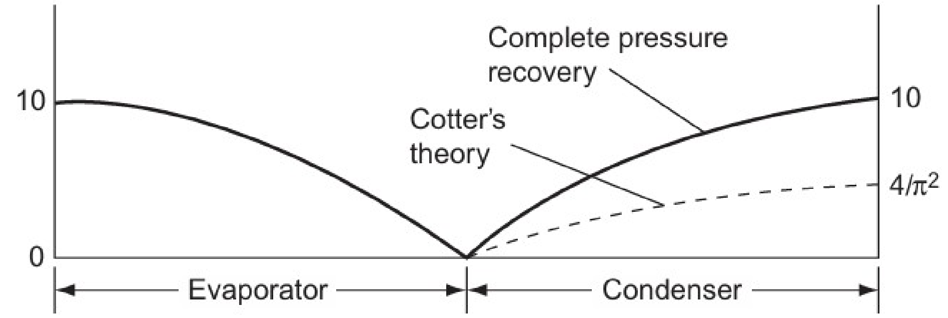

Figure 2.7: Full vs. Partial pressure recovery (adiabatic section redacted) [12]

Bankston and Smith [27] show that at the condenser section, it is possible that even for $Re_r > 2.3$, the flow might reverse in the axial direction, especially at high evaporation/condensation rates. They go on to show that Busse's (1967) calculations[1] matches the Hagen-Poiseuille equation quite well for $Re_r < 10$. This is seen in Figure 2.8, where the pressure drop in symmetrical and cylindrical heat pipes with different aspect ratios (length/radius) can be observed. For higher aspect ratios, it is also seen that the approximation holds even better.

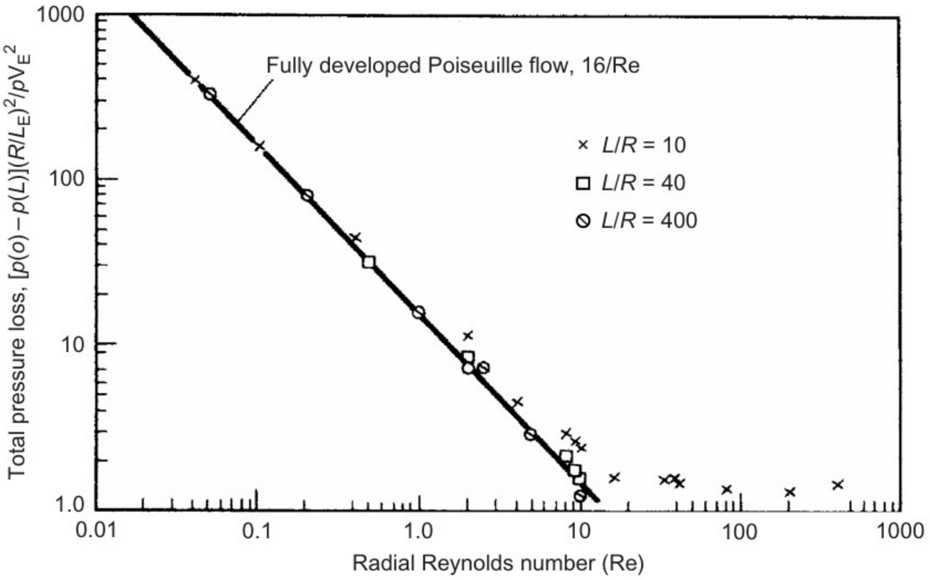

Figure 2.8: Pressure drop in heat pipes with predicted Poiseuille flow [12][27]

---

[1] Busse's paper could not be found online, although many papers have cited it.

Until now, only incompressible laminar flows have been considered. However, in certain applications, this could be a wrong assumption. Furthermore, many recent papers have considered the vapor phase as a compressible gas, in some cases becoming turbulent and also supersonic. Inherently, all real fluids are compressible. To understand if the density change of the fluid is important, the Mach number, given as $Ma = u/c$, must be checked, where u is the local flow velocity (m/s), and c is the speed of sound in the medium (m/s). For $Ma < 0.3$, fluids are generally considered incompressible, which means that their density is reasonably constant. However, gases are much more compressible than liquids in general. So much so that near saturation points, a pressure increase of 500 Pa for steam can induce a density increase of 33%. When considering the effects of compressible flow, the density term inside the material derivative in mass and momentum conservation equations can't be neglected, which results in the compressible Navier-Stokes equations.

When dealing with compressible flows, it is only natural to additionally consider the compressibility factor of gases. This factor, Z, commonly utilized in thermodynamics that describes the deviation towards a real gas from an ideal gas assumption, is defined as $Z = PM/\rho RT$, where M is the molecular mass of the species (kg/mol), R is the universal gas constant $(8.314\ J/(mol * K))$, and T is the temperature (K). For $Z = 1$, a gas can be considered ideal, meaning that the ideal gas theorem applies. The ideal gas theorem, which defines a relationship between the pressure, temperature, and density of the gas, is given by $P = nRT/V = \rho R_s T$. Here V is the volume of the gas (m^3), n is the number of moles (mol), and R_s is the specific gas constant $(J/(kg * K))$, calculated by $R_s = R/M$, where also $\rho = n/MV$.

The ideal gas theorem is a crucial equation for compressible flows. As density in the compressible Navier-Stokes equation becomes a variable, the number of equations that must be solved for increases by one. If the ideal gas theorem applies, the system is automatically closed once again. If the gas is non-ideal, then another equation of state must be chosen that is suitable for the system, which is most often called the cubic equations of state, such as the Peng-Robinson equation.

Another condition to investigate is the Knudsen number, Kn, which determines if continuum mechanics holds for a gas, or if it's more appropriate to formulate the gas in terms of statistical mechanics. This number, with Γ being the ratio of specific heats, is defined as $Kn = \sqrt{0.5\Gamma\pi} \cdot Ma/Re$ utilizing the Mach and Reynolds numbers. For $Kn < 0.01$, continuum mechanics holds well, whereas for $Kn > 10$, free molecular flow is a better approach, although it is stated to be problem dependent and recommended to be investigated specifically [28]. Depending on the combination of predicted Re, Ma, Z, and Kn, a proper approach to the problem of vapor flow must be chosen. For the case where a flow is considered compressible, statistical mechanics apply, and the gas is ideal, the system of equations can be closed by the Navier-Stokes equations coupled with the ideal gas law.

2.1.5. Surface Tension & Capillary Action

The final and sustaining factor of the pressure balance in the system, given by Equation 2.1, is the pressure difference caused by capillary action. Molecules of the same fluid attract one another, and at an interface, this attraction is no longer balanced as the closeness of the molecules is different in a certain direction. At this interface, the liquid aims to minimize its surface area by creating a curved interface shape. This causes a pressure difference across the inner and outer sides of the interface as work is done to curve the interface. This pressure difference can be described with the Young-Laplace equation $\Delta P = -\sigma(1/R_x + 1/R_y)$. Here, R_x and R_y are the radii of curvature of a 3D surface perpendicular to each other, in the x and y directions, as an example. "Wetting" fluids, such as water, when in contact with many materials, create a concave interface when looking from the liquid side; thus, the radii of curvature become negative. This means that the pressure change is positive when looking from the liquid side, meaning that the gas pressure is higher than the liquid pressure. For "Non-wetting" materials, on the other hand, like mercury, the interface is convex, meaning that the pressure inside the fluid is larger than outside. In narrow cross-sections, with sufficiently low Bond numbers $(Bo < 1)$, given by $Bo = \Delta\rho g L^2/\sigma$, the curvature resembles a spherical cap, seen in Figure 2.9, also known as a meniscus. Here, $\Delta\rho$ is the density difference between the two phases making up the interface (kg/m^3), and L is the characteristic length (m), such as the radius of a capillary tube.

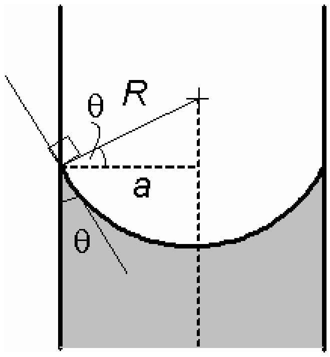

Figure 2.9: Forming of a meniscus at a capillary interface [29]

As the two radii of curvature of a sphere are equal to each other, R, the Young-Laplace equation simplifies into $\Delta P = 2\sigma/R$. The radius of curvature R, seen in Figure 2.9, can also be written as $R = a/\cos\theta$. The final equation for the pressure drop across the spherical interface is then $\Delta P = 2\sigma\cos\theta/a$.

As seen from the simplified Young-Laplace equation, the three factors that affect the surface tension pressure drop are the surface tension coefficient of the fluid (which is a function of temperature), the angle it makes with the surrounding solid, and the radius of the characteristic gap. As seen in Figure 2.10, all three of these could be different at the two ends of a wick, due to geometrical differences as well as temperature changes. Thus, the pressure drop due to capillary action in a wick can be written as the difference in surface tension pressure drops along the interfaces of the evaporator and condenser sections as in Equation 2.9.

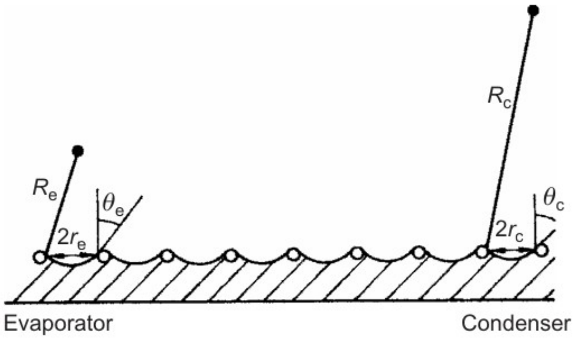

Figure 2.10: Surface tension variation along a heat pipe wick [12]

$$\Delta P_c = \Delta P_{c,e} - \Delta P_{c,o} = \frac{2\sigma_e\cos\theta_e}{r_{p,e}} - \frac{2\sigma_o\cos\theta_o}{r_{p,o}} \tag{2.9}$$

Ideally, maximum pressure difference is obtained when a flat interface occurs at the condenser, such that $\theta_c = 0$. This means that at the condenser section, the pressures of the two phases are roughly equal. Most often, the radius of the pores, r_p, in a sintered wick can also be considered constant, meaning that $r_c = r_e = r_p$. Then, the maximum possible capillary pressure difference is obtained by

$$\Delta P_{c,max} = \frac{2\sigma_e\cos\theta_e}{r_p} \tag{2.10}$$

For a sintered wick heat pipe, with a non-horizontal orientation, laminar and incompressible flow in both the wick and vapor core with full pressure recovery, the final pressure balance that must be satisfied can thus be written considering all previous approximations and simplifications as

$$\frac{2\sigma_e \cos\theta_e}{r_p} \geq \frac{\dot{m}\mu_l}{A_w \rho_l \kappa} l_{eff} + \frac{8\mu_v \dot{m}}{\pi \rho_v r_v^4} l_{eff} + \rho_l g l \sin\phi \tag{2.11}$$

This equation is the simplest pressure balance in a heat pipe, as the assumptions that have been made were mostly for ideal cases, with strong simplifications. A first look at the formation shows that the pressure drop in the liquid phase is most often the dominant one, as the permeability of the wick can go down to orders of magnitude such as 10^{-12}. Because of this, in some cases, the other pressure drop terms are neglected when designing a heat pipe. However, an accurate model must take into account each and every effect, and to do so, conservation equations must be used. Thus, this pressure balance is used as a reference throughout the literature, especially in design studies.

This pressure balance can also be visualized with Figure 2.11, which shows the relevant pressure drops qualitatively. The terms $\Delta P_{c,\delta}$ and $\Delta P_{e,\delta}$ are the pressure drops due to the phase change in the evaporator and condenser sections, respectively. These terms are usually neglected [16], but they will be briefly mentioned in the next section.

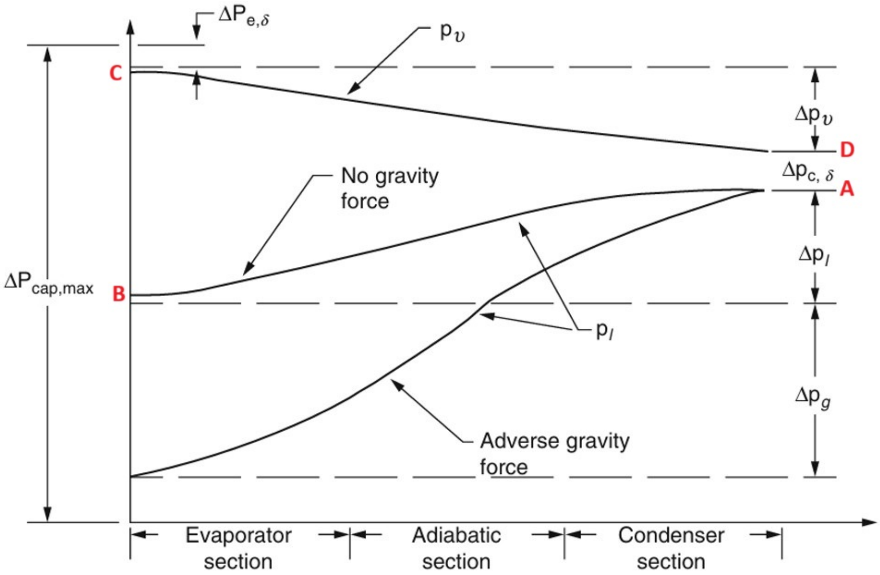

Figure 2.11: Arbitrary heat pipe pressure balance [13][16]

It is seen that in the existence of adverse gravitational forces, the capillary pressure necessary for operation can become considerably higher, depending on the liquid density and heat pipe length. For the case where the heat pipe is horizontal, the flow of fluids can be thought to follow the lines denoted in the figure as $A \rightarrow B \rightarrow C \rightarrow D \rightarrow A$: The fluid at the condenser flows through the wick, dropping in pressure until the evaporator. Then, it evaporates and gains pressure due to the increased thermal energy, and flows through the core while losing a small amount of pressure. It again loses pressure while condensing and becomes a liquid at the condenser section. This path is how a heat pipe operates fundamentally, in terms of its working fluid.

2.2. Heat Transfer in Heat Pipes

Heat transfer in heat pipes is the second most crucial topic to cover in terms of the fundamentals and background knowledge. Depending on the heat pipe design, the heat transfer characteristics change, especially in the wick. There are simple temperature drops associated with the solid casing due to the heating/cooling of the heat pipe. The complex structure of wicks is also crucial to understanding the thermal behavior, which will be explained in detail. The liquid-vapor interface, as well as the vapor itself, also provides further thermal resistance to the heat pipe. The simultaneous effects of these phenomena result in the thermal performance of the system. With the fluid dynamics fundamentals set, the heat transfer aspects will now be covered.

2.2.1. Conduction Through Solids

The casing of heat pipes is most often made of solid metals. When modelling heat transfer in solids, the most common method is to investigate Fourier's law of conduction, which is $\dot{\boldsymbol{q}} = -\boldsymbol{k}\boldsymbol{\nabla}T$. This states that a given heat flux, depending on the thermal conductivity of the material, causes a temperature gradient. The thermal conductivity, $\boldsymbol{k}$ $(W/(m * K))$, can be isotropic or anisotropic. In common solid metals, it is most often isotropic, and anisotropic in some composite materials. For cylindrical metal shells, such as the case for the heat pipe of this study, the heat rate, using one-dimensional Fourier's law, can be defined as $\dot{Q} = -kA_h dT/dr$. Here, A_h is defined as the surface area of the heated section (mostly the evaporator), given by $A_h = 2\pi r_c l_e$, where r_c is the radius of the casing. Rearranging this equation and integrating gives $\dot{Q} = 2\pi k l_e \Delta T/ln(r_c/r_w)$. In this case, $T_1 - T_2 = \Delta T$ is the temperature drop along the radial direction of the solid casing.

With this equation, if the temperature at the outer surface of the casing is known along with the heat input, the temperature on the interface between the wick and the casing can be determined. At steady state, assuming that the heating and cooling happen at the evaporator and condenser sections, respectively, the sum of the heat rates at these two sections is zero. This means that for constant material properties, the temperature gradients observed at the evaporator and condenser sections in the casing are equal in magnitude and opposite in sign.

2.2.2. Effective Properties of Wicks

The wick section of heat pipes can come in many different sizes and shapes. A few examples were given in Figure 2.2. Many other configurations are possible, but for the purpose of this study, only sintered metal powder wicks will be considered.

All materials have many different properties, such as density, temperature, mass, and electrical conductivity. These properties are better understood when divided into groups, namely: intensive and extensive. Intensive properties are independent of the amount of matter, whereas extensive properties are not. Considering a simple block of solid copper, its density is intensive, as it will be the same when the sample size is one gram or one tonne. However, mass and volume are extensive properties and depend on the size of the sample, as described above. Some intensive properties can also be calculated from extensive properties, depending on their function. Density, for example, is an intensive bulk property, calculated by the division of two extensive properties, mass and volume: $\rho = m/V$.

For porous materials, density and specific heat capacity are important intensive bulk properties when considering heat transfer. Most often, these porous structures are made of two distinct materials, both having their own material properties. To obtain the effective bulk properties of such porous materials, the rule of mixtures can be applied, defined as

$$\phi_{eff} = \varepsilon\phi_1 + (1 - \varepsilon)\phi_2 \tag{2.12}$$

- ϕ_{eff}: effective bulk property
- ε: volume fraction of material 1 (or porosity), defined as $\varepsilon = \frac{V_1}{V_1+V_2} = \frac{V_1}{V_{total}}$
- ϕ_1: value of property for material 1
- ϕ_2: value of property for material 2

In the case of sintered metal powder wicks, the wick is considered as a porous medium, with the porosity ε defining the volume fraction of the fluid phase. Thus, the density and specific heat capacity of the sintered wick are simply calculated through the rule of mixtures.

Furthermore, properties can also be divided into their functional groups, such as thermodynamic, transport, mechanical, etc. These properties are subsets of intensive and extensive properties, depending on their function. Thermal conductivity, for example, is an intensive transport property, but it is not a result of different extensive properties. Such transport properties are independent of the sample size, and they are, in general, strongly dependent on the connection of the phases, which allows for the ”transport” of heat, fluid, current, etc. Often, these transport properties are seen in equations where they relate a flux to a gradient. Such is the case for thermal conductivity, which relates heat flux to a temperature gradient, and for permeability, which relates Darcy flux to a pressure gradient.

Due to the intrinsic importance of connections, a more detailed approach must be conducted for calculating such properties. For isotropic two-phase materials, Hashin-Shtrikman bounds [30] give the upper and lower possible values for effective transport properties, but in cases where the properties of the two materials are separated by multiple orders of magnitude, these bounds result in a large uncertainty field of possible values. In these cases, research has been conducted on specific configurations. The sintering process consists of randomly dispersing spherical metal powders onto a surface, which are fused together by heating. Such random distribution of spherical particles was investigated originally by Maxwell [31], assuming that the solid particles were far apart from each other. He went on to conclude that for such heterogeneous materials, the thermal conductivity can be calculated by Equation 2.13.

$$k_{eff} = k_s \frac{2 + k_l/k_s - 2\varepsilon(1 - k_l/k_s)}{2 + k_l/k_s + \varepsilon(1 - k_l/k_s)} \tag{2.13}$$

$$k_{eff} = \frac{k_l[(2k_l + k_s) - 2(1-\varepsilon)(k_l - k_s)]}{(2k_l - k_s) + (1-\varepsilon)(k_l - k_s)} \tag{2.14}$$

$$k_{eff} = k_s^{(1-\varepsilon)} k_l^{\varepsilon} \tag{2.15}$$

- k_{eff}: effective thermal conductivity
- k_s: solid phase thermal conductivity
- k_l: liquid phase thermal conductivity

Experimental calculations of Hideaki et. al. match Maxwell's calculations well, and they observed that this relation holds for different wick types as well, such as screen meshes [32]. This version of the equation is utilized by Reay [12] in their book too. More recent studies, such as Faghri, Buchko, Chen's, and more [33] [34] [35], use the derivation of Chi [36] for the effective thermal conductivity, which is given by Equation 2.14. The geometrical mean model (GMM) is also a method for approximating the thermal conductivity of porous materials, also known as Kirscher's model. This method is not used throughout the literature of heat pipes, but is common for other topics, including saturated porous media such as soils [37]. This equation is much simpler, in the form Equation 2.15.

These three equations result in drastically different thermal conductivities. For $\varepsilon = 0.5$, $k_l = 0.6\ W/(m*K)$, $k_s = 400\ W/(m*K)$ (50% porosity copper-water porous medium), Maxwell's formulation results in 153 $W/(m*K)$, Chi's results in 2.25 $W/(m*K)$, and GMM results in 13.6 $W/(m*K)$. As seen, these values can range between two orders of magnitude, indicating that no single equation can accurately predict the effective thermal conductivity of porous wicks, resulting in considerable uncertainty in mathematical modeling. Thus, when choosing this property in a model, the effects of the possible range is necessary to investigate.

2.2.3. Liquid-Vapor Interface

At the interface of the two fluids, there exists a phase change phenomenon. This phenomenon is deeply complex, and modelling it in full detail is a challenge on its own. A crucial thing to first understand is the pressure at both sides of the interface. Evaporation and condensation happen at the same rate for a liquid-vapor system in equilibrium; thus, the net mass flux at the boundary is zero. In the case of net evaporation, the surface must be losing mass, and vice versa for net condensation. This is a result of the pressure difference between the two sides of the same interface, which drives the mass flux. The most commonly used equation for calculating the mass flux per unit area at a phase change interface is the Schrage equation. For cases where the Mach number is low (many engineering applications) [38], the simplified and rearranged equation [39] is given by

$$\dot{m}'' = \frac{2\alpha}{2-\alpha} \frac{1}{\sqrt{2\pi R_s}} \left(\frac{p_i}{\sqrt{T_i}} - \frac{p_v}{\sqrt{T_v}} \right) \quad [kg/(m^2 s)] \tag{2.16}$$

- α: accommodation coefficient
- p_i: interface pressure (Pa)
- T_i: interface temperature (K)

The accommodation coefficient α has a value between 0 and 1, and is very sensitive to the system it is measured at [38]. Eames et. al. [40] have reviewed the accommodation coefficient of water for many different studies and configurations, and found that the value ranges between 0.01 and 1. Bongarala et. al. [41] have used $\alpha = 0.3$ for evaporation on a porous interface, which also agrees with Jamieson's work [42] on the condensation of steam. Assuming that the interface pressure is equal to the liquid pressure, and that the temperature difference is negligible due to the square root, such that $T_i \approx T_v$, the final mass flux can be calculated as $\dot{m}'' = \frac{2\alpha}{2-\alpha}\frac{\Delta P}{\sqrt{2\pi R_s T_v}}$.

This equation is similar to the calculations of Dunn & Reay [19], although they utilize a form of the Hertz-Knudsen formula with an accommodation coefficient of $\alpha = 1$. Ytrehus [43] notes that the Hert-Knudsen formula results in a less accurate result for systems that are not close to $Ma = 1$. Dunn & Reay go on to state that utilizing $\dot{q} = \dot{m}'' h_{fg}$, the heat flux at the interface can be written as $\dot{q} = \frac{h_{fg}\Delta P}{\sqrt{2\pi R_s T}}$.

Furthermore, they consider a simplified version of the Clausius-Clapeyron equation at the interface, similar to Equation A.1. The equation they use is in the form $\Delta P/\Delta T = P h_{fg}/R_s T^2$. By plugging in this form of Clausius-Clapeyron, they achieve the heat flux rate at the liquid-vapor interface can be calculated as $\dot{q} = P h_{fg}^2 \Delta T / \sqrt{2\pi R_s^3 T^3}$. This equation is useful for the fact that if one approximates (or calculates) the heat flux into the interface, the temperature drop across the interface can be found, which in turn gives a pressure boundary condition for solving the Navier-Stokes equations.

2.2.4. Vapor Temperature Drop

The vapor temperature changes inside the vapor core, and the most important effect is to consider the vapor temperature at the evaporator and condenser liquid-vapor interfaces. At these interfaces, Reay [19] applies Clausius-Clapeyron in its simplified form again, to state that the temperature drop between the two interfaces is related to the pressure drop as $\Delta T = \Delta P R_s T^2 / P h_{fg}$. The pressure drop ΔP can readily be calculated through an equation such as Equation 2.7; however, no information is provided for calculating the actual vapor pressure P_v. Choosing the average pressure of the medium could be a good approximation, intuitively, as the pressure change in low-temperature cases is also low.

Following the reasoning of this subsection and the previous ones, the temperature drops of each important thermal section of the heat pipe can be calculated. By doing so, a rough estimate of the total temperature drop across the heat pipe can be found, which becomes helpful when designing a heat pipe or conducting a preliminary test to see if the chosen heat pipe is sufficient for the designated purpose.

2.2.5. Operating Limits

Heat pipes inevitably have limits to their operation, which are often related to how much heat flux, $\dot{q}$, can be sustained in a given configuration and operating conditions. This section will go into the important limits and important considerations when choosing/using a heat pipe, by building on top of the previously explained fluid flow and heat transfer theory in heat pipes. The calculation of the limits can be done before experiments or mathematical models, as the relations are simple, and approximate values still result in generally correct limits. The results of these limits and their analysis can be found in the next chapter.

Viscous Limit The first limit to consider is the viscous limit of heat pipes. This limit is often observed at low temperatures, when the viscous effects dominate the fluid flow, leading to a low Reynolds number. This limit is defined by Busse [44] as

$$\dot{q} = \frac{r_v^2 h_{fg} \rho_v P_v}{16 \mu_v l_{eff}} \tag{2.17}$$

The properties are calculated at the evaporator section of the heat pipe, and it is shown that at low vapor pressures, P_v, the pressure drop is dominated by the absolute pressure of the evaporator section. As the interface where vapor is generated is most often assumed to be at a saturation point, the pressure and temperature are directly related. An increasing heat flux means that the temperature of the evaporator section increases, which leads to a higher vapor pressure and lower viscosity of the fluid. Busse's formulation matches the obtained results quite well, and a general recommendation: $\Delta P_v / P_v < 0.1$, is given, which ensures that the viscous limit is not reached. In the case that the viscous limit is reached, vapor flow experiences considerable viscous resistance and cannot establish an inertial flow. This often results in a reduction in performance, although it is not a common limit to observe other than during the start-up of a heat pipe.

Sonic Limit The speed of sound (c) in an ideal gas medium can be defined as $c = \sqrt{\Gamma R_s T}$. This means that at low temperatures, the speed of sound is also reduced. Considering the Mach number, a lower speed of sound increases the possibility of the flow becoming sonic ($Ma = 1$). At sonic conditions, information cannot travel upstream anymore, and thus, any change in the downstream (condenser) conditions does not affect the flow. This means that a larger pressure gradient will not result in a larger flow rate; thus, the flow becomes "choked", and the thermal performance becomes stagnated. Busse [44], assuming ideal gas law and Poiseuille flow, states that the sonic limit is defined as below. Busse states that the equation matches his experimental values well, as well as Levy's [45] formulation of the equation at sonic conditions.

$$\dot{q} = 0.474 h_{fg} \sqrt{\rho_v P_v} \tag{2.18}$$

Capillary Limit The capillary limit is the mass flow rate that can be sustained in a heat pipe. This is dependent on many different factors, which are essentially defined in the pressure balance equation given in Equation 2.11. The heat input to the system primarily drives the evaporation/condensation phenomena in terms of mass flow rate, given by $\dot{q} = \dot{m}'' h_{fg}$. At the capillary limit, the pressure balance equation can be rewritten for the mass flow rate as $\dot{m} =$ .... As $\dot{m}'' = \dot{m}/A_e$, where A_e is the evaporator surface area given by $2\pi r_v l_e$, the capillary limit can be generally written in the form $\dot{q} = \dot{m} h_{fg}/A_e = h_{fg}/A_e$ .... This is the most crucial limit in a heat pipe as described in Section 2.1.5, and very specific to each heat pipe, rather than a straightforward equation. Failure to satisfy the capillary limit most often means that the heat pipe will not operate at the designated conditions.

Entrainment Limit The flowing vapor exerts a shear force on the liquid at the interface. Depending on the properties of the fluids, this force could cause liquid droplets to be entrained and moved back towards the condenser side. Entrainment limit often does not halt the operation of the heat pipe; however, depending on the severity of the total entrained mass of liquid, performance can be limited. To define this limit, the Weber number (We) is commonly defined for a characteristic length z, $We = \rho_v u^2 z/\sigma$. In the case of wick heat pipes, z is the spacing in the wick (in sintered wicks, it is the pore radius r_p). Around the order of $We = 1$, entrainment is expected; thus, the entrainment velocity of the vapor can be written as $u = \sqrt{\sigma/\rho_v r_p}$ for $We = 1$. For the vapor phase, the mass flow rate per unit area can be written as the axial mass flux through the inner evaporator surface, assuming all mass transfer occurs there as $\dot{m}'' = \rho_v u$. Inserting this equation into $\dot{q} = \dot{m}'' h_{fg}$ and combining with the entrainment velocity given above, results in the entrainment limit, also calculated by Marcus [46] as

$$\dot{q} = \sqrt{\frac{\sigma \rho_v h_{fg}^2}{r_p}} \tag{2.19}$$

Boiling Limit At high heat fluxes and temperatures, the flow inside the wick starts to fully boil. At normal operating conditions, wick heat pipes have vaporization only at the interface between the liquid and the vapor. It was theorized and later shown that when boiling, the bubbles that are generated inside the wick sometimes get trapped and, over time, create a sheet. This severely reduces the heat transfer capacity of the heat pipe and potentially leads to the drying of the evaporator section of the wick [19]. Dryness significantly restricts operation, and drying over a prolonged period can be catastrophic to the heat pipe and is a safety concern. This limit was calculated by Marcus [46], and later verified through experimentation on a variable conductance heat pipe by him. The second part of the below equation was previously calculated by Hsu [47], which is the critical temperature increase, ΔT_{cr}, that causes the boiling phenomena. Thus, the boiling limit for a cylindrical heat pipe is given by

$$\dot{q} = \frac{k_w}{r_c \ln(r_w/r_v)} \frac{2\sigma T}{\rho_v h_{fg} r_p} \tag{2.20}$$

These operating limits most often contain temperature-dependent terms and also have temperature as a variable in their formulation. To understand the limitations, the maximum heat flux of each limit can then be calculated as a function of temperature. Plotting these limits as heat flux versus temperature can arbitrarily be visualized as in Figure 2.12, also known as a performance map. For continuous and correct operation, the heat pipe must be in the colored region as shown.

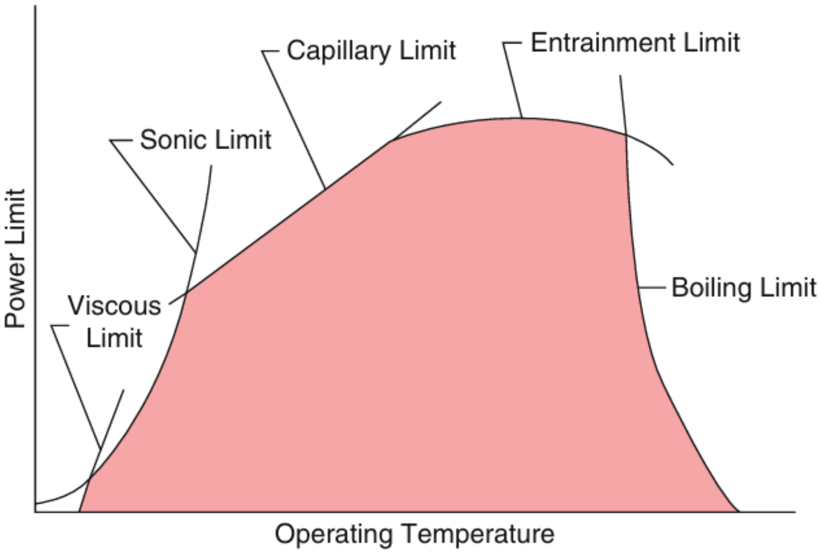

Figure 2.12: Representative operating limits of a heat pipe [13]

2.3. Review of Experimental Studies on Accelerating Heat Pipes

Multiple researchers have experimentally investigated the thermal performance effects of applying different types of acceleration motion profiles to heat pipes. Their results show that the effects are deeply complex and dependent on many factors. This section will aim to develop a fundamental understanding of these effects in order to present the problem that the thesis aims to model.

The most direct and significant influence on heat pipe operation comes from axial acceleration in the literature, which acts parallel to the primary liquid-vapor flow path. When oriented opposing the capillary-driven liquid return from condenser to evaporator, the effect is detrimental to the thermal performance across all studies. This external body force directly adds to the total pressure drop within the liquid phase. Asias et. al. [48] demonstrated experimentally that axial accelerations up to $12g$ for a sintered wick copper-water heat pipe with high porosity cause significant changes in the temperature of the evaporator section as the maximum available capillary pressure is exceeded due to the body force. The temperature increases drastically in the evaporator section when an unfavorable acceleration of $3g$ is applied; however, the performance is more complex when the acceleration is favorable. In the latter case, although it is favorable, higher accelerations ($6g$ and higher) cause the evaporator temperature to increase and become oscillatory, yet at low accelerations ($3g$), the performance is enhanced through the reduction of the evaporator temperature. They also demonstrate that the initial performance is recoverable after supposed dryout of the evaporator wick. Asias et. al. also state that the heat pipe essentially begins to operate as a thermosiphon, where liquid pools in the evaporator and undergoes periodic, explosive boiling, ejecting slugs of liquid and vapor toward the condenser, called the geyser effect. This creates a distinct failure mode rooted in instability rather than simple capillary starvation, which is the explanation behind the oscillatory behavior. The results they obtain for the highest acceleration case can be seen in Figure 2.13, which shows the oscillatory behavior with a recovery of the steady state operation conditions.

Zaghdoudi & Sarno [49] further state that for a similar heat pipe, they suspect acceleration in the unfavorable direction causes dryout in the evaporator, and a liquid to build up on the condenser section, which escaped the wick. Furthermore, for an operating power of 40 W and acceleration of $10g$, they observe that the thermal resistance increases by 70%, and is not fully recovered after the acceleration is

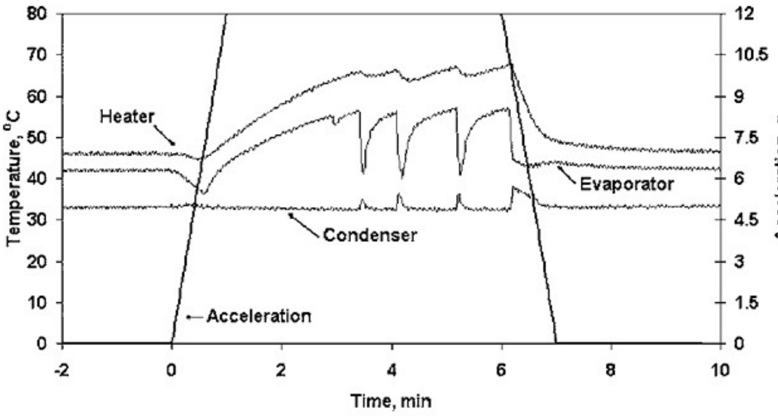

Figure 2.13: Results of Asias et. al. [48] for a sintered copper-water heat pipe at a longitudinal acceleration of $12g$

stopped. They wait for a shorter time after the acceleration is applied compared to Asias et. al., which could explain the different findings of returning to the initial state. Their results for a flat sintered copper-water heat pipe can be found in Figure 2.14. Voigt & Drossel [10] find that in the case of longitudinal acceleration of $0.5g$, the performance varies with respect to the inclination of the heat pipe and the wick type. For a screen-mesh heat copper-water heat pipe, they find that acceleration, higher operating power, and inclination have a negligible effect on the performance. For a sintered one, they find that there is an optimal range of operation, and continuously increasing heat input can become unfavorable, irrespective of the inclination (albeit the thermal resistance magnitudes are different as expected for different inclinations). Their most crucial finding is that for a grooved heat pipe, the thermal resistance decreases steadily for increasing heat input, irrespective of the inclination. This suggests that wick types play a role in the dynamic effects of sloshing. Their results in a horizontal setup for the grooved and sintered wick types can be found in Figure 2.15. Thomas et al. [50] similarly found that the performance of a helically grooved heat pipe improved significantly through acceleration. They observed that the capillary limit increased by a factor of five when radial acceleration was increased from 0 to $6g$. The helical structure effectively acted as a screw pump, creating a powerful centrifugal pumping action that significantly augmented the liquid return to the evaporator. This finding critically shows that the wick architecture can be engineered to turn a potentially detrimental force into a significant performance enhancement.

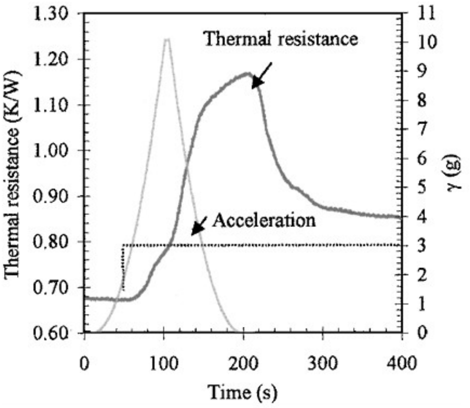

Figure 2.14: Results of Zaghdoudi & Sarno [49] for a flat sintered copper-water heat pipe at a longitudinal acceleration of $10g$, observing 70% increase in thermal resistance, and the steady-state performance is not fully recovered

The work of Charlton & Bowman [51] on a wrapped screen wick heat pipe subjected to transverse vibrations up to $5g$ at 1000 Hz found negligible effects on the capillary limit of the heat pipe. Huber & Bowman [52], investigating a wrapped screen wick heat pipe, found that a $2g$ longitudinal vibration at $30-50$ Hz caused a conclusive $6-10\%$ degradation in the capillary limit. They attributed this to

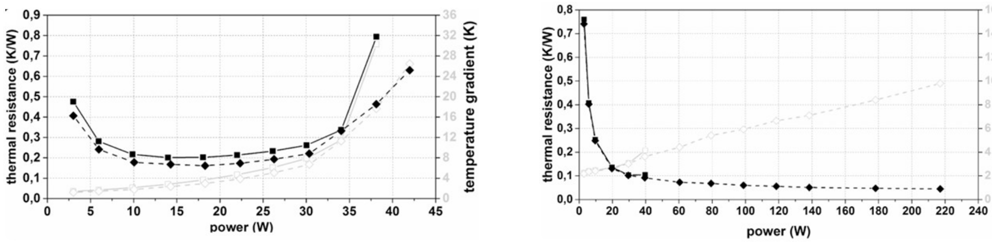

Figure 2.15: Voigt & Drossel [10], Left: horizontal sintered wick heat pipe, Right: horizontal grooved wick heat pipe. Steady State: black square straight line, Acceleration: black diamond dashed line

the mechanical agitation disrupting the liquid-vapor meniscus at the evaporator, which is the source of the capillary pumping pressure. This thus lowers the maximum sustainable heat load before dryout. In contrast, Deverall [53] found that it is possible that in inclined screen-mesh heat pipes, the escaped liquid that pools at one side can break up and re-wet the wick due to the vibrations more effectively. He found that the sinusoidal and random vibrations were thus not detrimental to the thermal performance. Alaei et al. [54] (for a wickless heat pipe) and Chen et al. [55] (for an axially grooved heat pipe) also show that at low frequencies $(0-30\ Hz)$ and amplitudes $(0.1-1g)$, longitudinal vibrations can enhance the thermal performance. Alaei et. al. also state that at low frequency vibrations, the most crucial factor for defining the thermal performance is the filling ratio of the heat pipe. Therefore, vibration can be stated to exhibit a dual nature: it can make a heat pipe operate more efficiently at nominal loads but cause it to fail at higher loads. Tournier & El-Genk [56] model in their transient study of a screen-mesh copper-water heat pipe, the build-up of a liquid pool at the condenser end during the start-up. They state that the development of this pool reduces the effective length of the condenser section and that the model accurately represents experimental values. This liquid build-up was experimentally shown by Merrigan et. al. [57] for a lithium heat pipe too, for which the liquid pool took up 10% of the total length of the heat pipe. The transient results of Tournier & El-Genk can be found in Figure 2.16 for the liquid pool developing and disappearing after favorable operating conditions are achieved in terms of temperature.

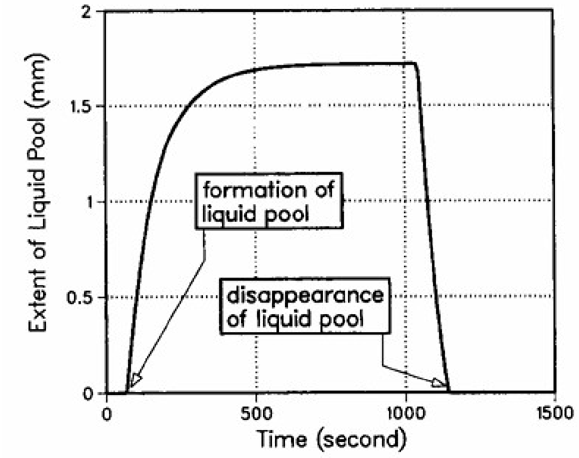

Figure 2.16: Results of Tournier & El-Genk [56] for the transient build-up of a liquid pool in the condenser section during start-up of a screen-mesh copper-water heat pipe.

The work of Baraya et al. [58] on transient thermal pulses demonstrated that once a dryout is initiated, the wick does not easily re-wet either. Even after the heat load was reduced to a level that was previously stable, the evaporator remained at an elevated temperature. Full recovery of the original low-resistance state required reducing the power to a level significantly below the initial capillary limit. They also found that if total dryout is attained, the thermal hysteresis is not recoverable, and the severity of the dryout affects the hysteresis magnitude as well. This effect is shown in Figure 2.17 for different durations of continuous dryout. The observations by Zaghdoudi & Sarno and Thomas et. al.

of difficult or incomplete re-priming after an acceleration event support this concept too. A brief but intense acceleration spike sufficient to cause a momentary dryout can de-prime the wick, leaving behind dry patches that create persistent high-resistance pathways. This means that the operational history of the heat pipe matters; a system subjected to transient g-loads may exhibit degraded performance that persists long after the mechanical event has passed. A brief overview of what these papers investigated, and their results can be shown in Table 2.1.

The findings of these researchers imply that dryout in a sintered wick is certainly possible for longitudinal accelerations, with magnitudes up to a few *g*'s. Furthermore, the rewetting of the wick is a complex process that is certainly dependent on the severity of the dryout as well as the history of previous dryouts. The frequency of the motion is also crucial, as higher vibrations result in observable degradation in the thermal performance, whereas low-frequency vibrations can enhance the re-wetting. The most crucial finding is that the wick type of the heat pipe is a fundamental factor in the dryout and re-stabilization of the heat pipe operation. It is seen in all of these numerical and experimental papers, however, that an equation or approach for modelling how or how much the liquid exits the wick is not given or discussed.

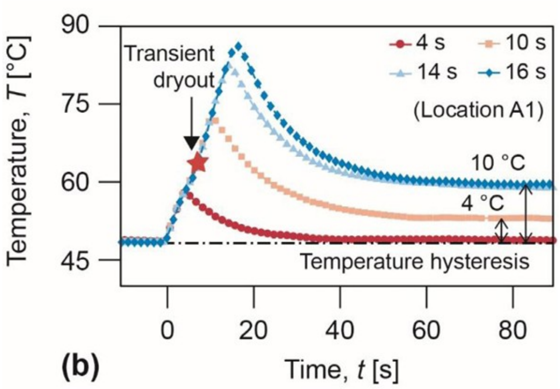

Figure 2.17: Results of Baraya et. al. [58] for a sintered copper-water observing thermal hysteresis for different durations of operation in dryout, Capillary Limit: 5.1 W

Table 2.1: Summarized literature findings on the dynamics of heat pipes

Research Group	Research Topic	Summarized Results
Asias et. al. [48]	Large Axial Accelerations	Large axial accelerations cause severe performance degradation in sintered wicks
Thomas et. al. [50]	Transverse Acceleration	Transverse acceleration of $6g$ for helically grooved heat pipes observe a five-fold increase in heat transfer limit
Voigt et. al. [10]	Longitudinal Acceleration	Longitudinal acceleration of $0.5g$ for sintered wick heat pipes cause small change in performance, and wick type is the most crucial factor
Zaghdoudi et. al. [49]	Longitudinal Acceleration	Such accelerations up to $10g$ cause evaporator dryout, liquid pooling, and up to 70% performance reduction
Alaei et. al. [54]	Low Frequency Vibrations	Low-frequency vibrations do not affect the heat pipe performance noticeably
Charlton et. al. [51]	Transverse Vibrations	Transverse vibrations have negligible effect on the heat pipe performance
Chen et. al. [55]	Small Longitudinal Vibrations	Low-frequency longitudinal vibrations are negligible or enhancing in terms of thermal performance
Deverall [53]	Sinusoidal/Random Vibrations	Such small amplitude vibrations are not detrimental, and could even enhance the re-wetting of the wick
Huber et. al. [52]	Longitudinal Vibrations	Longitudinal vibrations up to $2g$ can cause capillary transport limits
Baraya et. al. [58]	Hysteresis and Dryout	Hystheresis due to dryout increases with dryout severity, and might be irrecoverable
Merrigan et. al. [57]	Liquid Pooling	Liquid pooling during start-up can take up 10% of the total heat pipe length
Tournier et. al. [56]	Liquid Pooling	Liquid pooling during the start-up can take significant time to evaporate again

3

Description of the Models and Numerical Results

This first section of this chapter investigates the models built for analyzing the effects of sloshing on the heat pipe. These models are mathematical approaches aiming to define the multiphysical problems expected inside the heat pipe during a sloshing motion with a high acceleration magnitude. Numerical results for the mathematical models are presented where relevant, and they are discussed on their possible thermal effects. The second section defines a mathematical model for the steady state operation of the heat pipe and builds a computational model for the solution. The governing equations and boundary conditions are compared with literature models, and various results are analyzed thoroughly.

3.1. Mathematical Modeling of Dynamic Thermo-fluid Regimes: Leakout, Pool Build-up, and Rewetting of the Wick

This section of the thesis investigates the resulting thermo-fluid effects in a sintered powder wick copper-water heat pipe when an external axial acceleration is applied. Moreover, rather than a constant acceleration like gravity, a dynamic sinusoidal signal shown in Figure 3.1 is of interest, with a period of 50 ms ($f = 20Hz$), and a peak amplitude of 400 m/s^2.

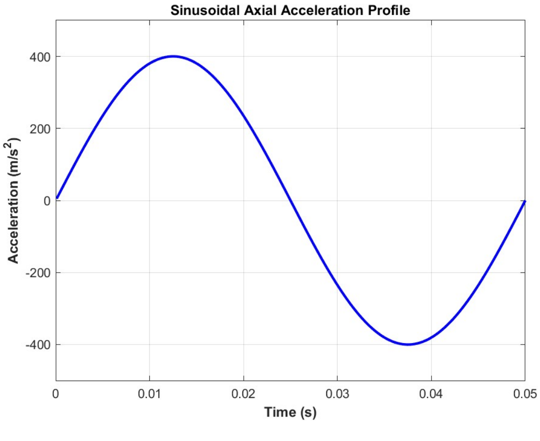

Figure 3.1: Visual of a sample sloshing motion

Such a signal exerting a peak acceleration larger than 40 times the magnitude of Earth's gravity is thought to cause possible different thermo-fluid behaviors inside this heat pipe, such as the ones researchers observed in chapter 2. To analyze these behaviors, a deeper dive into the fluid dynamics of what is assumed to be happening inside the heat pipe is necessary.

To begin, a simple thought experiment to intuitively visualize what might be happening inside can be presented as follows. A kitchen sponge, a highly porous and permeable material, is indeed a porous medium with liquid inside. When the sponge is highly saturated, any pressure applied to it causes a certain amount of liquid to be pushed out, such as the squeezing of the sponge, which is the application of mechanical pressure. Extending the idea, now consider a cylindrical sponge, kept upright on its circular surface. A certain amount of liquid might trickle down inside the sponge and leak out from the bottom surface. This time, the pressure is caused by the hydrostatic gradient, which is a result of Earth's gravity. If this ”sponge” is a hollow cylinder, made from a metal and enclosed on its outer surface, the result is not that far from a sintered wick heat pipe. When this described system is shaken at the given motion profile, the fluid response is expected to resemble liquid water getting squeezed out of a kitchen sponge.

The following subsections of the thesis thus theorize that the sintered wick has a certain amount of ”leakout” due to such an external force, and aim to model the leak through certain mathematical approximations. This leaked liquid then becomes a free fluid body inside the vapor core, which is shown in Figure 3.3. When the heat pipe is kept sloshing, the inertial movement of a free liquid body is also much faster than a porous flow. It is this inertial movement of the liquid that possibly re-wets the wick on the dried-out side, leading to rapid evaporation and enhanced heat transfer. The problem formulation with visuals will be presented to give a better understanding of the theorized behavior, qualitatively and quantitatively. Comments on the implications of the fluid behavior on the thermal response will be discussed, with possible comparisons to literature-observed results.

3.1.1. Problem Formulation

To begin, a geometry must be selected. The heat pipe investigated in this thesis is a sintered-powder wick copper-water cylindrical heat pipe. This heat pipe was simplified from a perfect cylinder into the image seen in Figure 3.2. The important domains in the geometry are selected as ”casing”, ”wick”, and ”vapor core”, and the end caps are neglected and approximated as walls.

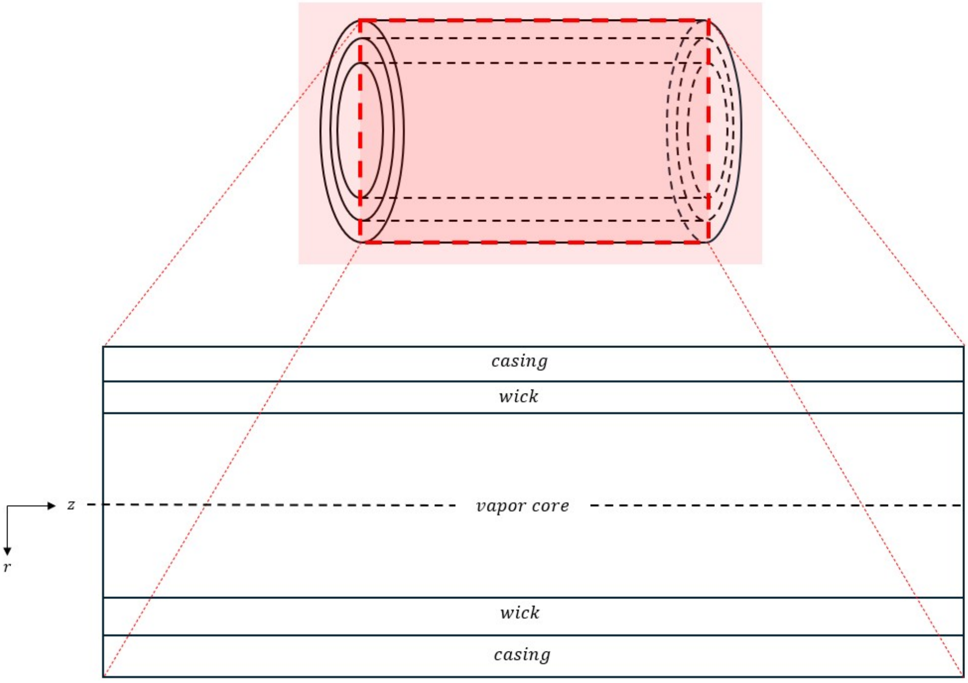

Figure 3.2: 2D cross-sectional cut of a cylindrical heat pipe

The model was conducted in 2D cylindrical coordinates, assuming axisymmetry. Thus, the ϕ component of the coordinate system was neglected. In the way to do so, a cross-sectional cut was made on a central rz-plane of the heat pipe, as seen in Figure 3.2. The final version of the geometry of interest can be seen in Figure 3.3.

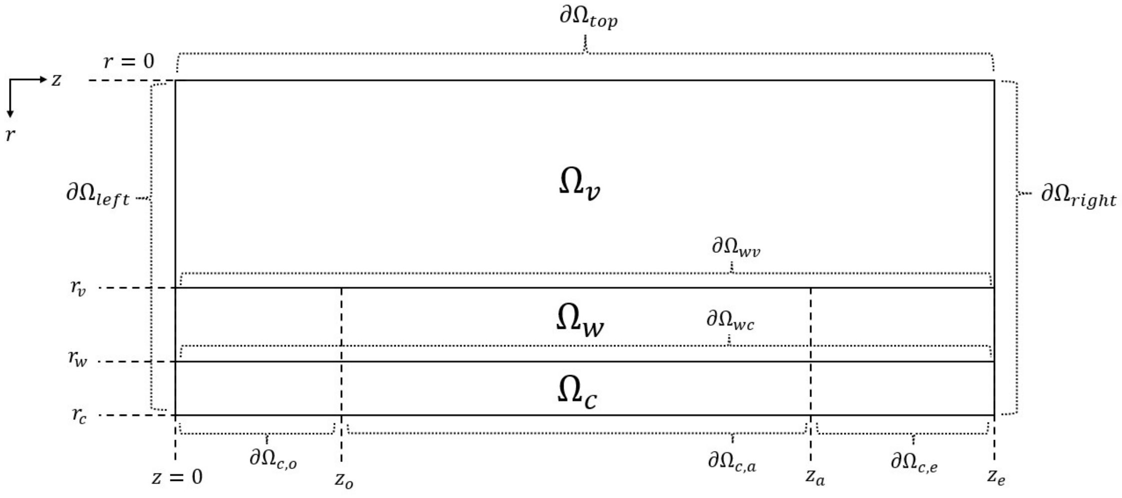

Figure 3.3: The full heat pipe geometry defined for the thesis

It can be observed that the geometry was split into multiple domains and boundaries in the r and z directions. The domains, Ω, represent the previously explained sections: casing, wick, and vapor core. The radial and axial distances with respect to the origin are denoted with subscripts for r and z. The boundary elements, $\partial\Omega$, are also clearly observed, with subscripts indicating their geometric locations. The dashed line at $r = 0$ represents the axis of symmetry. Relevant values of the heat pipe around $25°C$ and $2700\ Pa$ are presented in Table 3.1 for reference in certain equations and calculations.

Table 3.1: Relevant values of the heat pipe for mathematical modeling

Parameter	Meaning	Value
r_v	vapor core radius	$3.5\ mm$
r_w	wick radius	$3.75\ mm$
r_c	casing radius	$4\ mm$
z_o	end length of condenser zone	$75\ mm$
z_a	end length of adiabatic zone	$300\ mm$
z_e	end length of evaporator zone	$375\ mm$
ρ_l	liquid density	$997\ kg/m^3$
ρ_v	vapor density	$0.02\ kg/m^3$
μ_l	dynamic viscosity of the liquid	$1E-3\ kg/(m*s)$
μ_v	dynamic viscosity of the vapor	$1E-5\ kg/(m*s)$
σ	surface tension of water	$0.072\ kg/s^2$
ε	wick porosity	0.5

The first assumption to clarify is the axisymmetry. The geometry itself is inherently axisymmetric as it's a cylinder; however, the external conditions applied to the system are possible causes of asymmetry. These external conditions could be in the form of body forces, heat removal, mass addition, etc. In the case of this model, the only body forces applied are caused by the gravitational acceleration in the negative r-direction and the sloshing motion in the z-direction. Heating/cooling conditions are applied uniformly in the radial and axial directions of the heat pipe at the appropriate locations, and the wick is assumed to be homogeneous and isotropic. Evaporation/condensation is assumed to happen uniformly inside the heat pipe as well, and temperature distributions are also assumed to be uniform due to the high thermal conductivity of the material. Thus, what is left to analyze is the effect of gravity.

To do so, the Bond number was investigated. This number, which compares the effect of gravitational forces and surface tension forces, defined previously in Section 2.1.5, can be calculated to be in the order of 10^{-3}, meaning that the surface tension forces strongly dominate the gravitational forces. This means that the effects of gravity can be neglected, and justifies the assumption that axisymmetric modeling is valid.

Utilizing the results of the steady-state model, the Ca number can be calculated as $6 \cdot 10^{-6}$, and M as 2. The point this corresponds to lies in the transition region between stable displacement and capillary fingering as seen in Figure 3.4 with the red dot marking the expected flow regime of this model. This means that a perfectly sharp interface will not form inside the wick. However, the contact angle of water and steam at the expected temperature conditions is approximately 70°, which is similar to the experiments of Zhao [25], who had similar values of Ca and M. Thus, although a flat and stable front might not exist, a main ”saturation front” could be observed, as shown in Figure 2.6. Thus, it was decided that the thickness of the saturation front would not be thick enough to be considered compared to the length of the porous wick, and as such, from here on, the interface will be mathematically defined as a sharp line with zero thickness (images will aim to represent the interface figuratively).

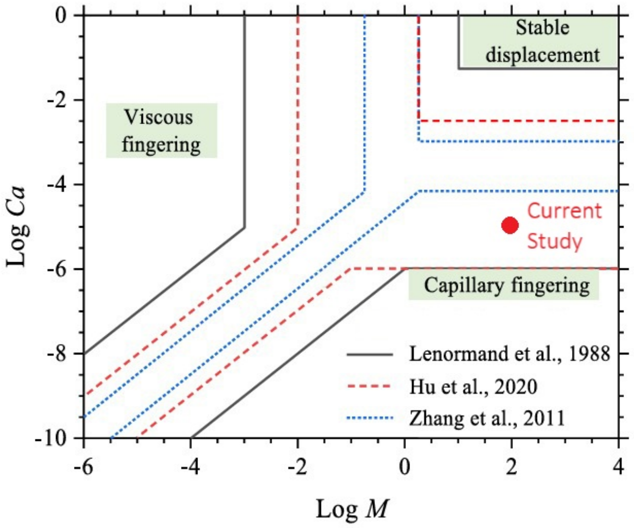

Figure 3.4: Expected flow regime of the current study, marked with the red dot

During the sloshing motion of the heat pipe, the main phase to investigate is the liquid, which is theorized to be leaking out of the wick. So, the wick domain must first be modeled. This domain can be visualized as in Figure 3.5, which is a section taken out from Figure 3.3.

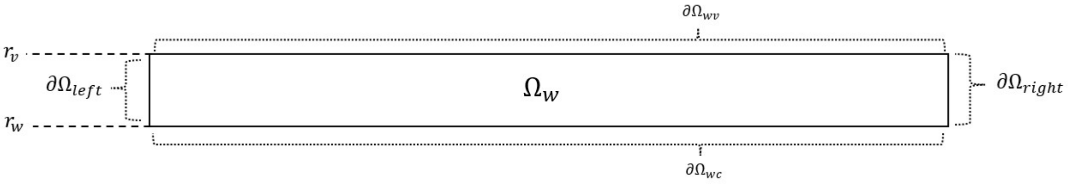

Figure 3.5: The wick domain of the heat pipe

It is important to first discuss the initial state of the wick. Under normal operating conditions, and as assumed in the previous section, the wick can be modelled as a fully saturated porous medium. Thus, at the interface between the vapor and liquid, there exists surface tension. For now, it is assumed that the heat pipe is not operating; such that there is no flow within the porous medium. When the sloshing motion is applied, an additional pressure gradient is generated along the z axis due to the external body force. If the liquid leaks out due to unbalanced pressures, an interface must form inside the porous medium between the liquid and the vapor, as the porous medium will not be fully saturated with the liquid phase anymore. The length of the liquid saturated porous media can be defined as $H(t)$, which is a function of time. Initially, $H(t) = l_{total}$; however, after leakout, $H(t) < l_{total}$ (labeled as cases ”a” and ”b” in Figure 3.6).

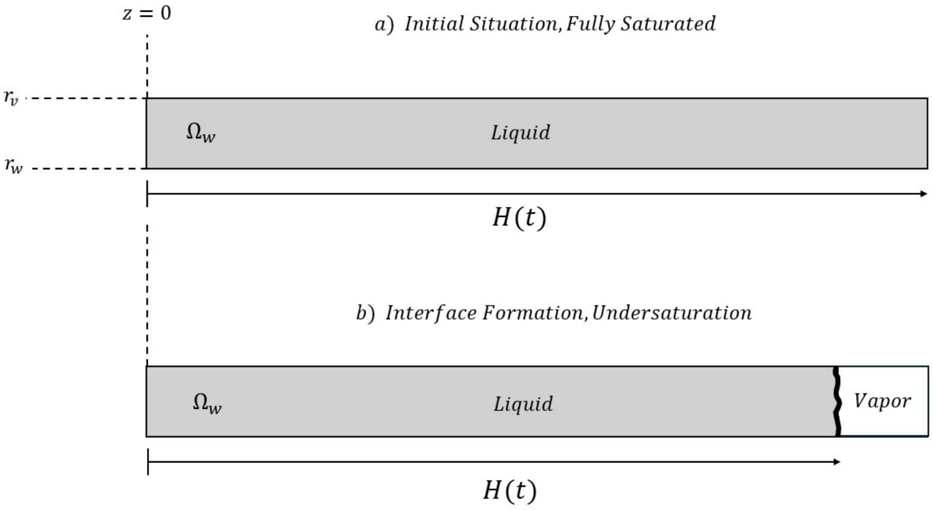

Figure 3.6: Interface formation due to leakout, a) represents the initial fully liquid saturated porous medium, b) represents the undersaturated porous medium with an interface formed between the two phases at length $H(t)$

To model the build-up of pressure that leads to this expected leakout, another length is defined, $L(t)$. This length is defined in the opposite direction of $H(t)$, and its dynamic datum point is the interface location. This continuously changing datum and the length $L(t)$ can be sketched as in Figure 3.7.

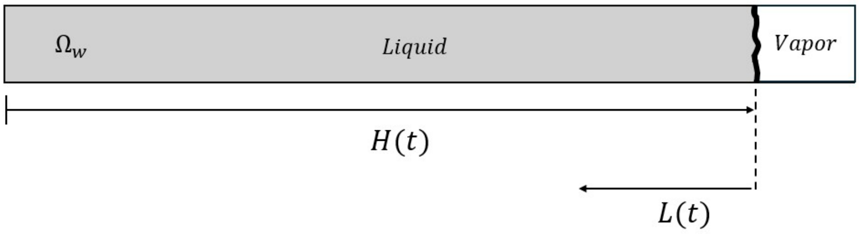

Figure 3.7: Length $L(t)$ defined for calculating pressure build-up

A simple analogy can now be made for a water column. The hydrostatic pressure of water in a column can be solved simply through Navier-Stokes, or in its simplified form, defined in Equation 2.6. In this case, acceleration $a(t)$ replaces gravity g, and $L(t)$ replaces the column height l. At a length L_{leak}, the pressure due to hydrostatics becomes equal to the surface tension pressure keeping the liquid inside. Furthermore, at a length $L(t) > L_{leak}$, hydrostatics will not hold anymore due to the resulting fluid movement. Converting this analogy to the current model, the pressure build-up at the point where the leakout theoretically starts with respect to the interface datum can be defined as

$$P_{leak} = \rho a(t) L(t) = \rho a(t) L_{leak} \tag{3.1}$$

The pressure at the interface between the liquid and vapor phases at the boundary Ω_{wv} can also be defined as Equation 2.10. The other boundaries have no-slip and no-penetration conditions, since they are solid walls: $u = w = 0$. At point $L(t) = L_{leak}$ where leakout begins, the liquid will break the interface, and at the final moment when the hydrostatic and surface tension pressures are balanced, it can be defined that for $\theta_e = 90°$ (perfect wetting)

$$\frac{2\sigma}{r_p} = \rho a(t) L(t) \tag{3.2}$$

This balance is the starting point of this chapter, and the following subsections will build on top of it. It is a simple approach to the deeply complex problem of multiphase interface physics in porous media, further complicated by dynamic body forces. However, it is considered necessary to start from such a point to obtain a representative, preliminary physical model that could generate insights into the full problem at hand. Possible behaviors theorized to occur within the heat pipe during dynamic motion after leakout are shown in Figure 3.8, where three cases are presented.

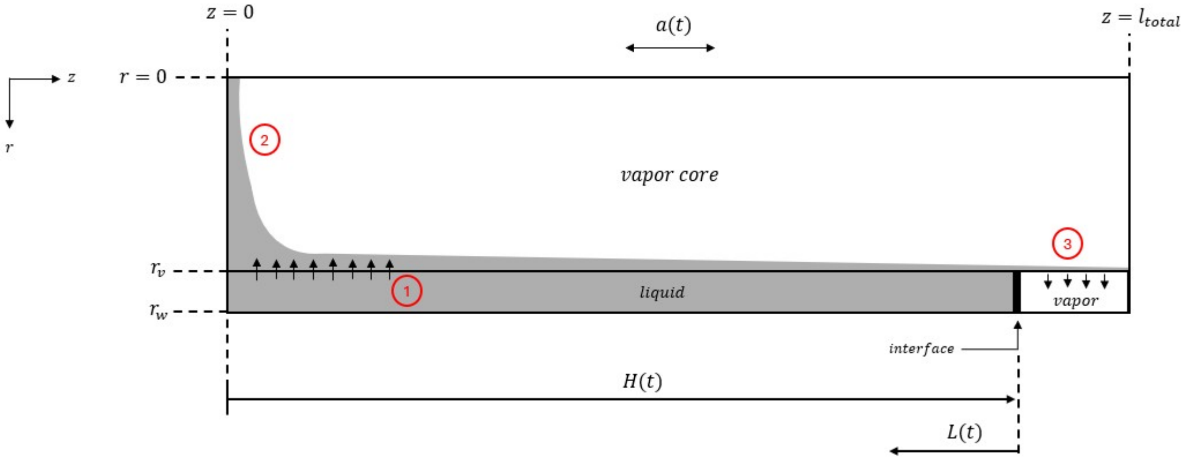

Figure 3.8: Visualization of the possible spontaneous internal view of the heat pipe after leakout

For the visualization of the dynamic behavior, only the wick and vapor core domains are required, as the casing is a pure solid. An arbitrary interface formed inside the wick has been visualized in Figure 3.8. These numbered cases can be summarized as follows, and will be further analyzed:

- **Case 1:** The sloshing motion causes a pressure build-up inside the wick, and if it becomes large enough, breakthrough happens on the wick-vapor core interface, and liquid leaks out.
- **Case 2:** The leaked out liquid mass forms a pool, building up on one end of the heat pipe during the movement, and new flow regimes develop for the free liquid.
- **Case 3:** Non-pooled liquid forms a film over the wick, possibly re-wetting the porous wick.

3.1.2. Case 1: Leakout

After any length $L(t) = L_{leak}$, the excess pressure is theorized to cause a certain amount of liquid to leak out. The total length that liquid will leak out through can thus be defined as $H(t) - L(t)$, seen in Figure 3.9, with a representation of the mass outflow.

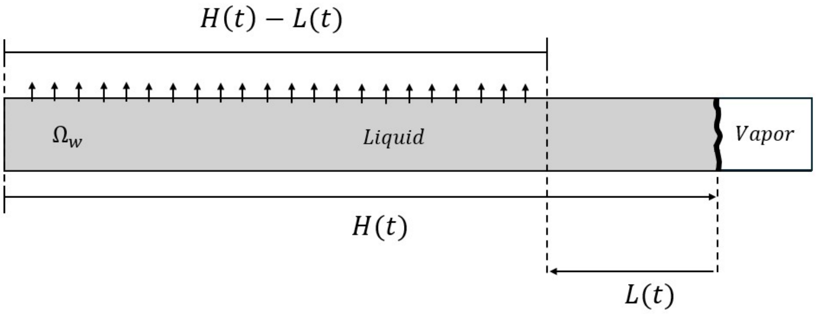

Figure 3.9: Total leakout length $H(t) - L(t)$, mass flow into the vapor core domain visualized with small black arrows

Here, the leakout start length $L(t)$ can be calculated as an inversely proportional function of the acceleration, as shown below, following Equation 3.1 and Equation 3.2. This is intuitive, as a higher acceleration will make the leakout more probable, which is also the consensus of literature researchers, as shown in the previous chapter. As $a(t)$ is defined, $L(t)$ can be known at any point in time through Equation 3.1 and Equation 3.2 as $L(t) = L_{leak} = 2\sigma/\rho r_p a(t)$. In the case that $L(t) < H(t)$, leakout will happen through the surface length $H(t) - L(t)$.

With this relationship, the existence of leakout can be analyzed at any time point. In the case that leakout exists, the leakout is caused by a pressure gradient that exceeds the surface tension pressure, which can be defined as $P_{excess} = \rho a(t)H(t)$. This is due to the fact that the whole liquid body is accelerated. This now-excess pressure gradient must be balanced through another pressure, along with surface tension. It is theorized that the leaking liquid can be characterized by a Darcy flux. The reasoning is that the pressure is assumed to vary linearly inside the wick, and the involvement of a porous medium makes the Darcy equation a simple but efficient tool to implement. The leakout, which exists in the surface length $H(t) - L(t)$, characterized by a Darcy pressure gradient with leak velocity $u_l(t)$, together with the surface tension which exists in the non-leaking section, is assumed to be in a continuous balance with the previously-excess pressure. Thus, this new balance can be written as

$$\frac{\mu u_l(t)\varepsilon[H(t) - L_{leak}]}{\kappa} + \frac{2\sigma}{r_p} = \rho a(t)H(t) \tag{3.3}$$

The leakout velocity, $u_l(t)$, can then be calculated as a function of $H(t)$. This leads to a system with two variables and a single equation. Thus, the system requires closure equations. It can be defined, however, that the mass leakout rate, $\dot{m}(t)$, is a function of the leakout velocity $u_l(t)$, and the leakout surface length $H(t) - L_{leak}$ as

$$\dot{m}(t) = \rho u_l(t) 2\pi r_v [H(t) - L_{leak}] \tag{3.4}$$

This introduces another equation and another variable. The crucial point to notice here is that the mass leakout rate $\dot{m}(t)$ is directly coupled with the change rate of the saturation length $\dot{H}(t)$. As mass flows out, the length of the saturated porous medium front, $H(t)$, will reduce, and the rate at which this length reduces is the closure equation for the system, defined as

$$\dot{H}(t) = \frac{\dot{m}(t)}{\varepsilon\rho\pi(r_w^2 - r_v^2)} \tag{3.5}$$

These three equations result in a first-order linear ordinary differential equation system for $H(t)$, for which the formulation can be found Equation A.3. It is evident that the solution of $H(t)$ crucially depends on the acceleration profile $a(t)$. Depending on the definition, a closed-form analytical solution might be impossible to find (such as the case of a sinusoidal profile, which requires a Bessel or Struve function). Furthermore, singularities may exist as $a(t)$ occurs in the denominator, which can be zero. For this reason, a numerical approach that utilizes the Forward Euler method to solve for $H(t)$ was implemented in MATLAB, defined in Appendix B, which makes the solution robust and protected against mathematical obstacles.

What is of critical interest is the variation of $H(t)$ with respect to the wick permeability, κ. As mentioned before, the wick permeability is a significant term of uncertainty. Depending on its value, the resulting leakout rate changes. Intuitively, a less permeable porous medium will hold its liquid strongly, and a more permeable one less so. As permeability is also related to the pore radius, the interplay between the wick characteristics and the leakout rate becomes complex. The current model aims to simplify this by investigating the direct relationship between $H(t)$ and varying κ. By doing so, the dryness of the wick can be known as a function of time with respect to its permeability value, and the total liquid that leaks out of the wick in one acceleration signal period can be calculated.

The results of the dryness of the wick after a single acceleration signal period can be found in Figure 3.10. Dryness is a simple ratio of $H(t)/H_0$, where H_0 is the initial length of the saturated front, equal to the heat pipe length.

It is observed that the critical region of the permeability lies between $\kappa = 10^{-13} - 10^{-11}\ m^2$. In this region, the dryness of the wick drastically increases with increasing permeability. Below the lower threshold, the wick stays mostly saturated, and values above the upper threshold certainly lead to almost total leakout of the liquid. This is a crucial finding that shows that the leakout phenomenon, modeled in the above-described method, is certainly possible. It is also seen that the dryness reaches a

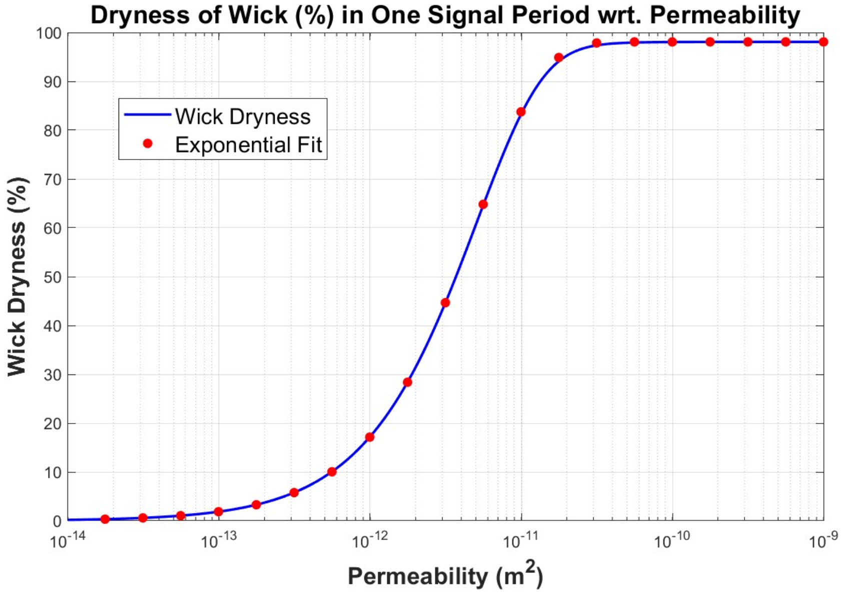

Figure 3.10: Dryness of the wick represented in percentage, $Dryness\ (\%) = 100 * H_{final}/H_{initial}$

limit at $\kappa = 10^{-10}\ m^2$, with a value of 98.07%. It is observed that the theoretical limit of 100% is not reached by the numerical solution. The possible reasons why will be discussed in the next chapter.

The total volume of liquid in the wick in the initial situation can be calculated simply by $m_{liquid,0} = \varepsilon \pi l_{total} \rho_l (r_w^2 - r_v^2)$ as 1.06 $grams$. Considering the heat pipe in the vertical orientation, the leaked liquid of this mass would result in a cylindrical column height of 26 mm, assuming the liquid does not flow back into the porous medium. This corresponds to approximately one-third of the condenser/evaporator sections, or 7% of the total heat pipe length, similar to the results of Merrigan et. al. [57] for the start-up of a heat pipe, for which they calculated a liquid pool corresponding to 10% of the total heat pipe length.

The evaporator section in the heat pipe considered in this thesis corresponds to 20% of the total length of the heat pipe. It is also analogous to consider that it corresponds to 20% of the total liquid volume. Assuming that leakout happens only at the condenser section, such that the liquid at the evaporator section is drained towards the condenser, a total leakout volume of 20% results in the total dryout of the evaporator, which corresponds to the leakout from a single acceleration signal period at a permeability of $\kappa = 10^{-12}\ m^2$. This situation is an operating limit, often observed as the boiling limit, described in the previous chapter. In the case that the evaporator section is dried out, there is no liquid to evaporate, which halts the operation of the heat pipe, and might cause lasting damage to the heat pipe if it lasts considerably long, as shown by Baraya et al. [58] in Figure 2.17.

To further define a relationship between the permeability and the dryness percentage, an exponential decay equation in the increasing form was fit to the values. This equation is given as

$$Dryness\ (\%) = 98.07(1 - e^{\zeta\kappa}), \quad \zeta = 1.933E^{11} \tag{3.6}$$

This equation results in the dryness of the wick by inserting a known value of the permeability, with an accuracy of 99.99%, which is an exceptionally accurate prediction. This equation can thus be used as a predictive measure of the expected leakout when considering the design of a sintered-powder wick in this configuration and parameters. The applicability of the equation will be discussed in more detail in the next chapter.

3.1.3. Case 2: Pool Build-up

The liquid that leaks out of the wick enters the vapor core, where it has more dynamic freedom. As the heat pipe is accelerated, the fluid will move inside the vapor core due to body forces. A passenger sitting in an accelerating car observes the same as they're pushed back into their seat, or in the inverse case, they are pushed forward towards the dashboard. Focusing solely on the vapor core during acceleration in the positive z-direction, this is visualized (exaggeratedly) in Figure 3.11.

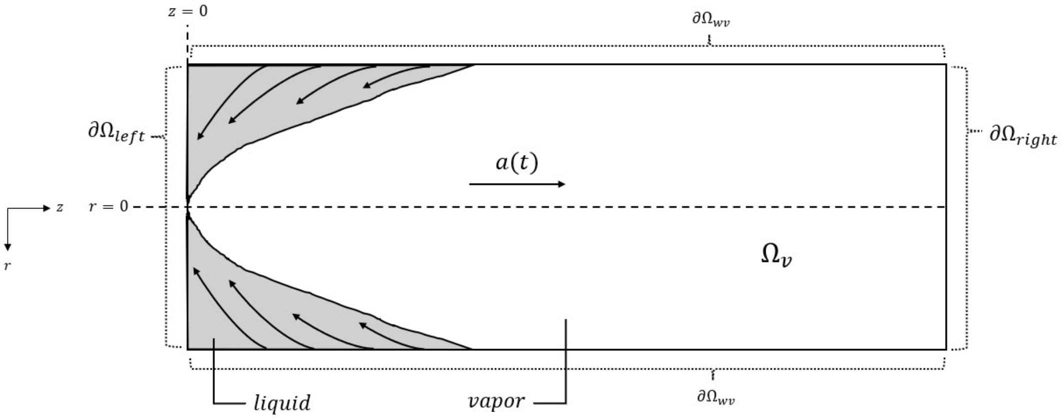

Figure 3.11: Pool build-up towards the back end during acceleration on the positive z-direction

In the figure, the arrows aim to visualize the movement of the liquid that is pushed out of the porous medium, and then pushed back into the end of the heat pipe due to inertia. As the heat pipe in this study has a characteristic length of 7 mm in the vapor core, there are different possibilities of what is happening to the liquid body when a large acceleration is applied. It is already known from the previous section that the liquid pool can reach a thickness of 26 mm in the z-direction, which is a substantial value. The dynamics of this pool will be investigated in the following subsections.

3.1.3.1. Reverse Axisymmetric Stagnation Flow

Consider a jet impinging on a wall, as shown in Figure 3.12. Here, the inertial fluid that encounters a discontinuous geometry has to spread outwards, assuming laminar flow. This flow regime is often called a stagnation flow.

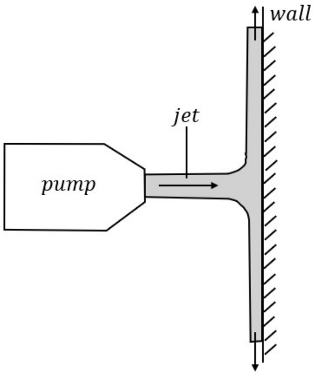

Figure 3.12: Jet impinging on a wall in 2D, "stagnation flow"

For the case of an axisymmetric (θ is negligible) flow, this phenomenon is then called an "axisymmetric stagnation flow". Such a flow was investigated by Scholle et. al. [59] in Cartesian coordinates, visualized in Figure 3.13. In the inverse of this phenomenon, such that streamlines converge in the center of a circle, an outward jet was theorized to possibly form, as visualized in Figure 3.14.

Assuming that the liquid leakout from the wick is uniform in the θ axis and gravity is negligible, the converging point is the center of the vapor core, visualized in Figure 3.11. Researchers such as Saddington et. al. [60] have investigated a similar phenomenon for short take-off, vertical landing (STOVL) aircraft with dual jets. In such cases where the aircraft is close to the ground, the dual jets impinge on the ground surface, similar to Figure 3.12. These two impinging jets then flow outwards,

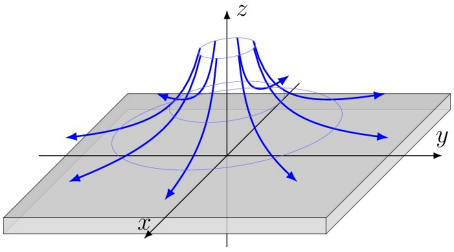

Figure 3.13: Axisymmetric stagnation flow in Cartesian coordinates [59]

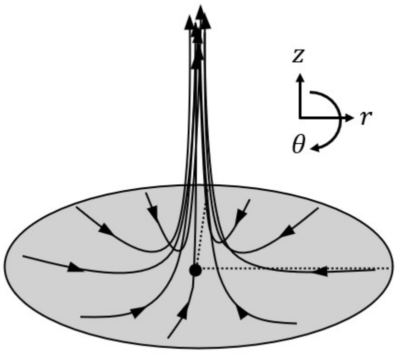

Figure 3.14: Reverse axisymmetric stagnation flow in cylindrical coordinates

and in the center, they impinge on each other and create a stagnation point, which results in an upward flow, called an ”upwash fountain flow”. This phenomenon can be shown as in Figure 3.15.

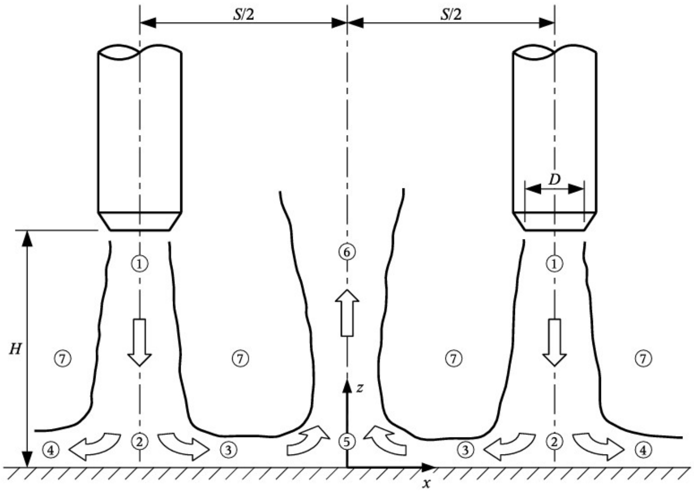

Figure 3.15: Impinging dual jets, creating an ”upwash fountain flow”, numbered as **6** [60]

This phenomenon, first shown by Whollebe et. al. [61], is deeply complex, and is related to many different parameters, such as the distance between the two jets, the angle of the jets, and the pressure ratios of the jets, investigated also by researchers such as Bhargav et.al. [62] and Zhang et.al. [63]. Due to the complexity, the phenomenon was not investigated thoroughly; however, the thought procedure behind the potential expected flow is visualized in Figure 3.16.

To understand the possible effects of this flow, consider a case where the permeability of the wick is $\kappa = 10^{-10}\ m^2$. This value results in a mass outflow of approximately 1 $gram$ of water as shown in Figure 3.10, in a time span of 50 ms. The average mass flow rate can thus be written as $\dot{m}_{avg} = 0.001/0.05\ [kg/s]$, which gives a result of 0.02 kg/s. The expected reverse axisymmetric stagnation flow

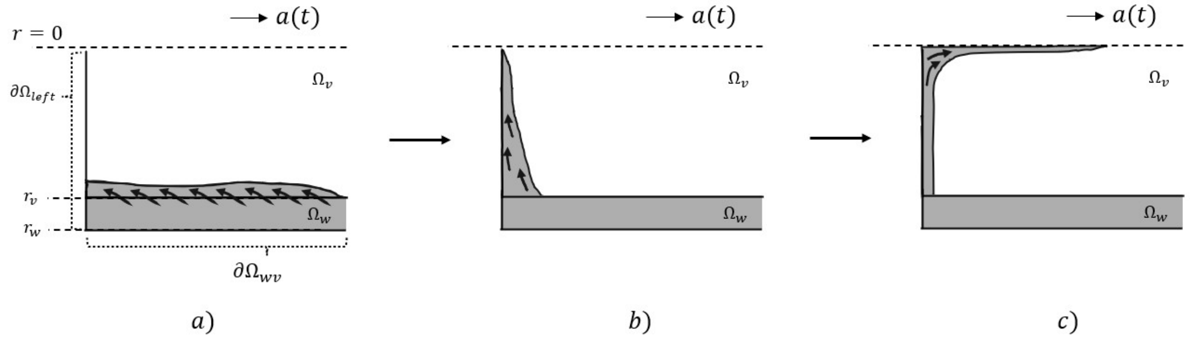

Figure 3.16: Theorized reversed axisymmetric stagnation flow: **a)** the liquid exits the wick **b)** free fluid is pushed back due to acceleration and travels towards the center of the core **c)** fluid converges in the center and develops a reversed axisymmetric stagnation flow

will have a complex shape both near the stagnation point, as well as the moving "upwash fountain" front. To simplify the problem, consider the geometry in Figure 3.17.

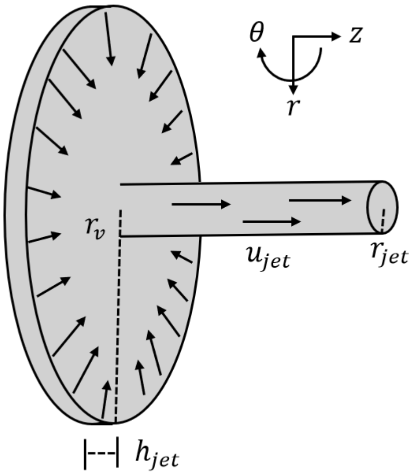

Figure 3.17: Simplified reverse axisymmetric stagnation flow

Here, a radial flow converges towards the stagnation point, after which it flows outwards, creating a "jet". For such a jet to form uniformly, the flow must be axisymmetric in the θ axis, and it must be laminar. The inflow velocity to the large "disk" can be defined as

$$\dot{m}_{avg} = \rho 2\pi r_v h_{jet} u_{in} \tag{3.7}$$

This shows that the inflow velocity is a dependent variable of h_{jet}. The Reynolds number can also be written for the disk as $Re_{disk} = \rho u_{in} h_{jet}/\mu$. Utilizing the above equation, the Reynolds number can be defined as $Re_{disk} = \dot{m}_{avg}/2\pi r_v \mu$, which can be calculated as approximately $Re_{disk} \approx 910$. This means that the flow can be assumed laminar. In this case, the stagnation flow will be smooth. The mass inflow to the jet is known as $\dot{m}_{avg}$; however, r_{jet} is unknown, and u_{jet} is a dependent variable of r_{jet}. A simple mass flow rate balance can be stated as

$$\dot{m}_{avg} = \pi \rho r_{jet}^2 u_{jet} \tag{3.8}$$

A similar approach to the Reynolds number of the jet reveals that the result is dependent on the jet radius, as $Re_{jet} = 2\dot{m}_{avg}/\pi r_v \mu$. As the jet is depicted to resemble a pipe, knowing that turbulence in pipe flow is expected for $Re > 4000$, the critical jet radius can be stated as 3.2 mm, which is approximately equal to the vapor core radius. A jet radius below this value is expected to result in a turbulent flow.

This line of reasoning is evidently flawed and depends on a multitude of assumptions and approximations. However, the aim is to understand if this hypothetical jet can travel a significant distance. In the case of a jet with radius $r_{jet} = 3.2\ mm$, the jet velocity u_{jet} can be found as $0.62\ m/s$. The time during free-fall from the center of the vapor core for the jet can simply be calculated as $\Delta t = \sqrt{2r_v/g}$, which gives $\Delta t \approx 27\ ms$. In this case, the jet travels $17\ mm$ as $\Delta x = u_{jet} * \Delta t$. It is already contradictory that the average mass flow rate is calculated through the total signal length, whereas the free-fall time of the jet is approximately half of that value. However, this shows that at the limit of laminar flow, the jet can travel a small distance. It is noticed that this length is shorter than the maximum pool thickness found in the previous section, which is $26\ mm$.

Following this extremely simplistic approach, it can be stated that the laminar jet is not expected to affect the performance considerably. In the case of a turbulent jet with a smaller jet radius, the jet can possibly travel a farther distance. In such cases, the liquid that reaches the dried evaporator will experience a much larger temperature than required to evaporate. Such a case will result in instantaneous evaporation and a larger pressure gradient due to the high-temperature vapor. This vapor will rapidly travel to the condenser section and condense, releasing its latent heat. This could potentially enhance the heat transfer efficiency of the heat pipe. In the case of sloshing or a jet, the velocity at which the liquid will reach the evaporator is much higher than the Darcy flow in the wick, and as it evaporates into a higher temperature vapor, the vapor flow is expected to be faster towards the condenser. This shortened timescale of the vapor flow is the main reason behind the possible enhancement of the thermal performance. Yet, under the light of the possibilities investigated in this subsection, a reverse axisymmetric stagnation flow does not seem to yield promising results for the heat transfer enhancement of the heat pipe under large axial accelerations.

3.1.3.2. Rayleigh-Taylor Instability

The pool build-up section investigated the liquid behavior when the heat pipe was accelerating in the positive z-direction, and the liquid was pooling on the back end of the acceleration direction. Consider the case where the inertial forces on the fluid are not sufficient to cause the reverse axisymmetric stagnation flow. In this case, there exists a finite thickness liquid layer covering the left boundary $\partial\Omega_{left}$ due to the leaked liquid. This subsection investigates the sudden deceleration of the heat pipe in this configuration.

When the vapor core with a body of liquid at one end starts decelerating, the two fluids are suddenly in a position that can generate instabilities. The Atwood number (A) is a dimensionless number for analyzing the stability of a two-phase system, in this case, a liquid-vapor system. This number is given by $A = (\rho_l - \rho_v)/(\rho_l + \rho_v)$. In a reference frame where the heavy fluid is on top of the lighter fluid, if the acceleration $(a(t))$ is downwards, the state is deemed unstable. In such an unstable case, any perturbation on the interface of the liquid-vapor phases will start growing in magnitude. This instability growth is often defined by the Rayleigh-Taylor Instability (RTI). Such instabilities are most often characterized by a rising (in this case, falling) plume. More recent papers investigating these instabilities obtain CFD results with visuals such as Figure 3.18. Sharp [64] states that for Atwood numbers close to 1, the characteristic shape of the plumes will resemble round-topped bubbles, whereas lower numbers close to 0 will resemble interpenetrating bubble fingers. Sharp's calculations for an Atwood number of 0.6 can also be found in Figure 3.19.

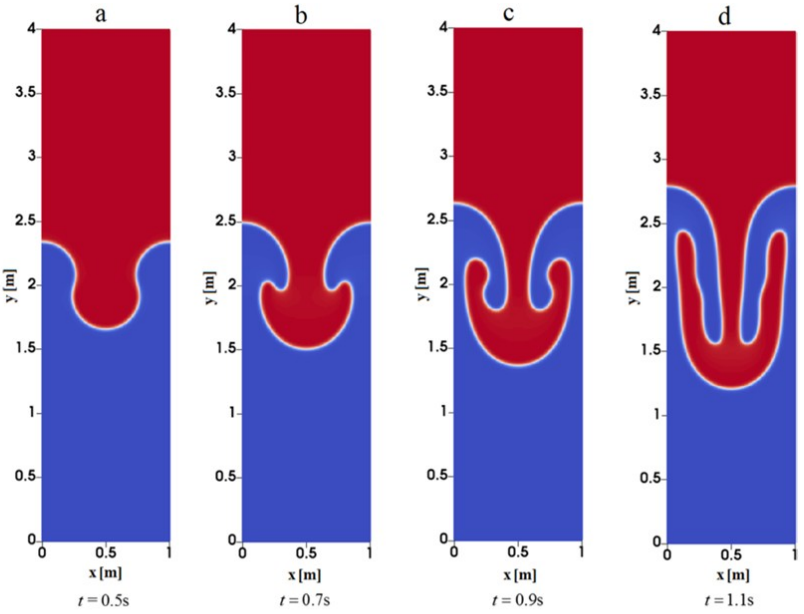

Figure 3.18: Time evolution of an RTI for an Atwood number of 0.5 [65], bubble shaped plumes in **b**

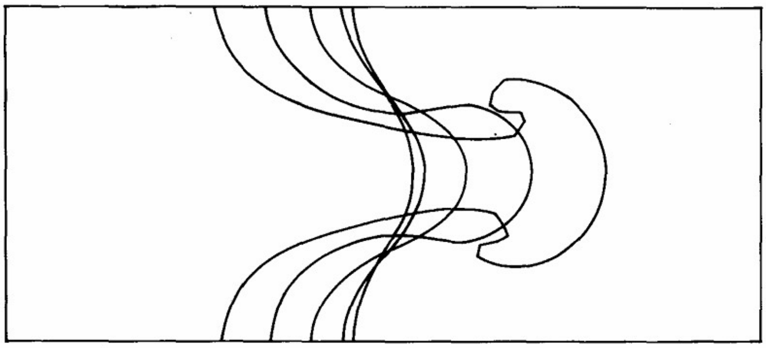

Figure 3.19: Growth of a perturbation, calculated by Sharp [64] for $A = 0.6$

The growth of such instabilities is attempted to be stabilized by surface tension forces (σ), if their effects are relevant. This relevancy can be checked through the Weber number, which was defined previously. The growth rate of these instabilities, Σ, given by Sharp [64], is defined as

$$\Sigma^2 = \frac{\rho_l - \rho_v}{\rho_l + \rho_v} a(t) K - \frac{\sigma K^3}{\rho_l + \rho_v} \tag{3.9}$$

Here, K is the wavenumber of the instability. This equation indirectly shows that the instabilities grow under the condition that the wavenumber K is smaller than the critical wavenumber, K_c, which is also given by Sharp [64], defined as

$$K_c = \sqrt{\frac{(\rho_l - \rho_v) a(t)}{\sigma}} \tag{3.10}$$

What is crucial to check is whether these instabilities are possible or not in the heat pipe. For values of $\rho_l = 997$ (kg/m^3), $\rho_v = 0.02$ (kg/m^3), $\sigma = 0.072$ (N/m), the range of possible values for K_c can be found for varying $a(t)$. As the absolute magnitude of $a(t)$ is between 0 and 400 (m/s^2), the critical wavenumber varies between 0 and 2353 (m^{-1}). Knowing the wavelength of a perturbation λ is $\lambda = 1/K$, the minimum wavelength perturbation that can grow in the heat pipe is 0.4 mm. As this value is smaller than the heat pipe diameter of the vapor core, it is certainly possible that RTIs can form and grow. A mathematical analysis of Σ^2 with respect to K shows that the maximum growth rate is obtained for $K_{max} = K_c/\sqrt{3}$ (derived in Appendix A.2). Inserting this into Equation 3.9 gives that the maximum instability growth rate, Σ_{max}, which is

$$\Sigma_{max} = \sqrt{\frac{2\sigma}{\rho_l - \rho_v}\left[\frac{(\rho_l - \rho_v)a(t)}{3\sigma}\right]^{3/2}} \tag{3.11}$$

In such small wavelengths mentioned above (0.4 mm), multiple simultaneous instabilities could generate in the vapor core. In this case, it is theorized that the interface between the fluids evolving through time can resemble the depiction in Figure 3.20.

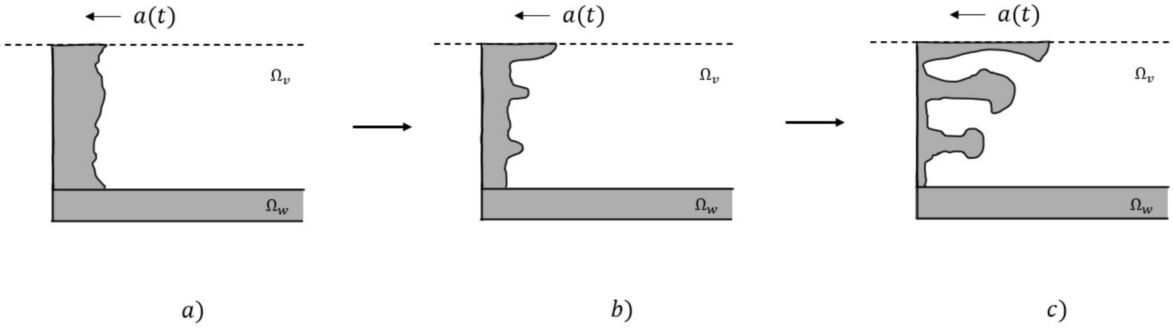

Figure 3.20: Possible generation and growth of perturbations in the heat pipe: **a)** a finite thickness liquid pool exists at one of the heat pipe walls **b)** acceleration in the direction that can generate RTIs is applied, possible perturbations occur **c)** initial perturbations grow in bubble-shaped plumes rapidly

As the RTI case considers the acceleration profile purely when the system is in an unstable configuration, the half sine wave where the acceleration is negative in Figure 3.1 must be investigated. The average value of a half sine is given by $2W_{max}/\pi$, where W_{max} is the maximum amplitude of the sine. In this case, taking into account the wave given in Figure 3.1, the average is approximately 255 m/s^2, for a duration of 25 ms, which is approximately equal to the free-fall time of a fluid at the center of the vapor core. Inserting this average sine value into Equation 3.11 along with standard values for water at 25°C results in a maximum average growth rate of approximately $\Sigma_{max} = 430\ s^{-1}$.

Consider a case where the instability caused by a perturbation on the surface grows exponentially. The characteristic time is given by $\chi = 1/\Sigma_{max}$, which gives $\chi = 2.32\ ms$. In the case of exponential growth, this means that any perturbation with initial amplitude M_0 will grow by a factor of e every 2.32 ms, which is extremely small. Furthermore, applying the exponential growth equation, $M_{final} = M_0 e^{\Sigma_{max} t}$, shows that during the half sine wave of 25 ms, the initial perturbation will grow in magnitude by a factor of $e^{\Sigma_{max} t}$, which is equal to 46630. This means that if an initial perturbation on the flat surface between the two phases has an amplitude larger than 8 μm, the perturbation will grow to a size larger than the total length of the heat pipe.

Although it is a simple calculation with multiple assumptions and simplifications, such as the exponential growth of the perturbation with no resisting forces, this shows that even a small perturbation can grow immensely large in a very short time span. The average velocity of such an instability growth can be defined as $u_{RTI} = l_{total}/\Delta t = 15\ m/s$, which results in a Reynolds number of $Re_{RTI} = \rho u_{RTI} 2 r_v/\mu = 104700$, which is strong evidence that the flow is turbulent in this simplified case. As the fluid travels to the other side of the heat pipe, rapid evaporation is expected to happen at the dried-out wick surface, and the resulting vapor will possibly move towards the condenser, where it releases the latent heat. The values calculated in this subsection suggest that the instabilities can travel significant distances, which makes the enhancement of heat transfer in the heat pipe possible. Furthermore, the turbulent mixing inside the vapor core between the two phases can further enhance heat transfer, as turbulence is known to increase the heat transfer rate. Although these enhancements may take place for the heat pipe thermal performance, this highly turbulent multiphase flow is deeply complex, and a definitive statement cannot be made.

3.1.4. Case 3: Rewetting of the Wick

The liquid pool, which might form and then break up in various ways, some of which were investigated in the previous subsection, will inevitably come in contact with the porous wick. In the case that the wick is dry, i.e., saturated with vapor, and there is a liquid film with finite thickness over it, the expected instantaneous configuration can be found in Figure 3.21.

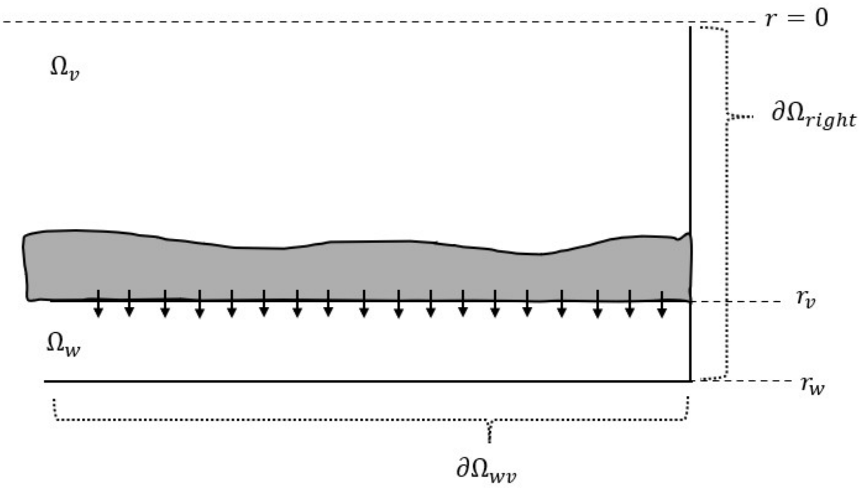

Figure 3.21: Possible state after dryout where a liquid film exists over the dry wick, black arrows representing imbibition

In such a case, the liquid film can impregnate the porous medium while pushing the vapor out, and the porous medium can be rewetted. The porous medium can be simplified and approximated as a collection of capillary tubes, with a radius equal to the pore radius. Knowing that the permeability of the wick, κ, can be calculated semi-empirically through Equation 2.5, results in the relation $\kappa \propto r_p^2$. Thus, a very simple analogy to apply is the capillary rise in a tube, characterized by the Lucas-Washburn equation (LWE) [66], given by

$$D^2(t, \kappa) = \frac{\sigma r_p \cos\theta}{2\mu} t \tag{3.12}$$

This describes the relation between the penetration depth $D(t)$ into a capillary tube with respect to time t, in a case where gravitational effects are negligible and the radius of the capillary tube is constant. This relation is characterized by $D \propto \sqrt{t}$, meaning that the liquid starts penetrating rapidly, and then slows down. de Gennes et. al. [66] state that this is a physical limitation of the equation, as the original derivation of the Lucas-Washburn equation neglects inertia, and thus, the relationship is inaccurate in the early stages of impregnation. They further state that during the early inertial regime, an equation in the form below is a better representation of the capillary rise, calculated by Quere [67] as

$$D(t, \kappa) = t \left(\frac{2\sigma \cos\theta}{\rho r_p} \right)^{1/2} \tag{3.13}$$

Quere also states that before a time $\chi = \rho r_p^2 / 4\mu$, the inertial regime is the dominant regime, as the viscous flow must be developed, which can be calculated as 0.625 ms. This is the parabolic solution to the force balance he defines. A simple comparison of the two equations for the system that is investigated can be shown below in Figure 3.22. In the figure, it is observed that the two regimes indeed cross at $t = 0.625$ ms for the configuration of the wick in this thesis, with a pore radius of 50 μm. This results agrees with Quere's calculations. Furthermore, it is seen that the inertial regime is expected to take approximately 0.25 ms to fully impregnate the wick, whereas the viscous regime has a value closer to 0.1 ms. This further shows that the viscous regime possibly undershoots the expected time for the penetration of a capillary tube.

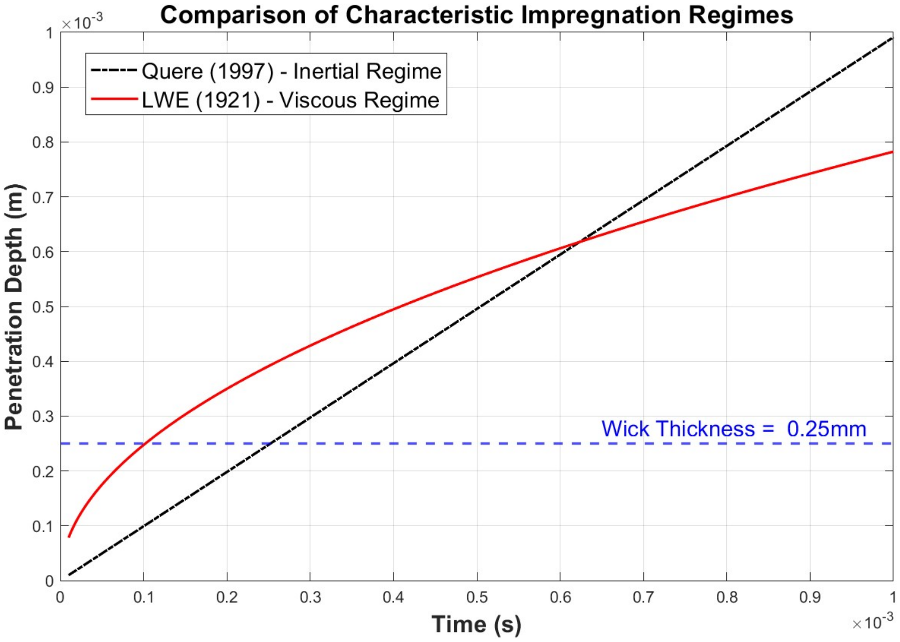

Figure 3.22: The two mathematical approaches to the impregnation of the porous medium of pore radius 50 μm, with the maximum penetration depth shown in blue

One important behavior to point out is that the parabolic solution timescale, where the regimes are equal to each other, varies with $\chi \propto r_p^2$. On the other hand, for the same penetration depth, the inertial regime duration varies with $t \propto r_p^{0.5}$, and the viscous regime varies with $t \propto r_p^{-1}$, shown in the above equations. As $\kappa \propto r_p^2$, a reduction in the pore radius results in a lower expected permeability, and thus, a shorter duration where the inertial regime is prominent compared to the viscous regime (smaller χ). This means that the viscous regime is expected to take over faster in low-permeability wicks. Moreover, a smaller r_p means that the time required for impregnation is larger in the viscous regime. The combined effect is that in lower-permeability wicks, re-wetting is much more difficult compared to higher-permeability wicks, giving a relation between the impregnation time and permeability as $\kappa \propto t^{-2}$. This is expected as lower-permeability wicks resist leakout more, so, intuitively, they will resist re-wetting as well.

These calculations overall show that it is certainly possible that the leaked liquid will rewet the dry wick, as the timescale of the possible rewetting is in the order of 10^{-4} s, whereas the sloshing motion has a characteristic timescale in the order of 10^{-2} s. This shows that the rewetting action is a quicker process compared to the leakout. As the previous cases also emphasized, rewetting of the wick can re-establish the thermal performance of the wick rapidly, or at least improve it. The re-supplying of liquid to the dried wick is crucial for the continuation of evaporation, and any means that accomplish this is expected to aid the heat pipe. It is, however, stressed that the rewetting case is investigated using simple analogies in 1D, and although the results imply rewetting will take place, uncertainties exist, especially due to the cylindrical geometry of the actual heat pipe.

This section of the thesis investigated different fluid flow scenarios, and obtained numerical results in each case. These results are presented briefly in Table 3.2 for an overview of the findings. The possible effects on the thermal performance of the heat pipe are also estimated alongside these obtained results. The overall estimates suggest that the sintered-powder wick can experience significant leakout at permeability values above $\kappa = 10^{-12}$ m^2. Yet, above these values, the sloshing motion of the heat pipe can generate liquid flows that can resupply liquid to the dried wick, with timescale shorter than the leakout timescales. The rapid rewetting of the wick due to the liquid flow is expected to support the heat pipe in terms of thermal operation, and can enhance its performance.

Table 3.2: Summarized findings of the mathematical models developed in this section

Flow Case	**Estimated Dynamics of the Fluid**	**Expected Thermal Effects**
1) Leakout	Liquid leaks out of the wick due to large axial accelerations, causing pressure gradients high enough to push liquid out of the porous medium	Permeability of the wick crucially affects the resulting dryness, which affects the thermal performance as the drying of the evaporator section drastically restricts the operation
2) Pool Build-up	A reverse axisymmetric stagnation flow develops and forms a jet due to the inertial movement of the fluid	The jet velocity in a laminar case is not high enough to travel large distances, thus, the effect is possibly negligible
	Rayleigh-Taylor instabilities form due to the unstable configuration of the two fluid phases, which grow rapidly	RTI's grow extremely rapidly, possibly traveling the total length of the heat pipe, and resulting in the rapid evaporation of the sloshed liquid that reaches the dry sections, enhancing performance
3) Rewetting of the Wick	The wick is rewetted due to impregnation of the porous medium by the liquid, which happens on a short timescale	The wick can be rewetted due to capillary action in a short timescale, which suggests that the sloshed liquid in the vapor core can effectively re-saturate the wick, possibly enhancing operation

3.2. A Computational Model for Steady-State Operation

This section will dive into the mathematical and computational model built for the steady-state operation of the heat pipe. This will be done by defining important governing equations and boundary conditions, compared with models in the literature. Justifications for certain assumptions will be made, and the numerical solution method will be explained in detail. The results obtained from the computational simulation will be presented and discussed in detail, literature comparisons will be made where possible, and the overall convergence will be justified.

The heat pipe investigated in the thesis was explained in the previous section. The steady-state model was conducted in 2D cylindrical coordinates, assuming axisymmetry as before. The geometry is shown again to be referenced in Figure 3.23.

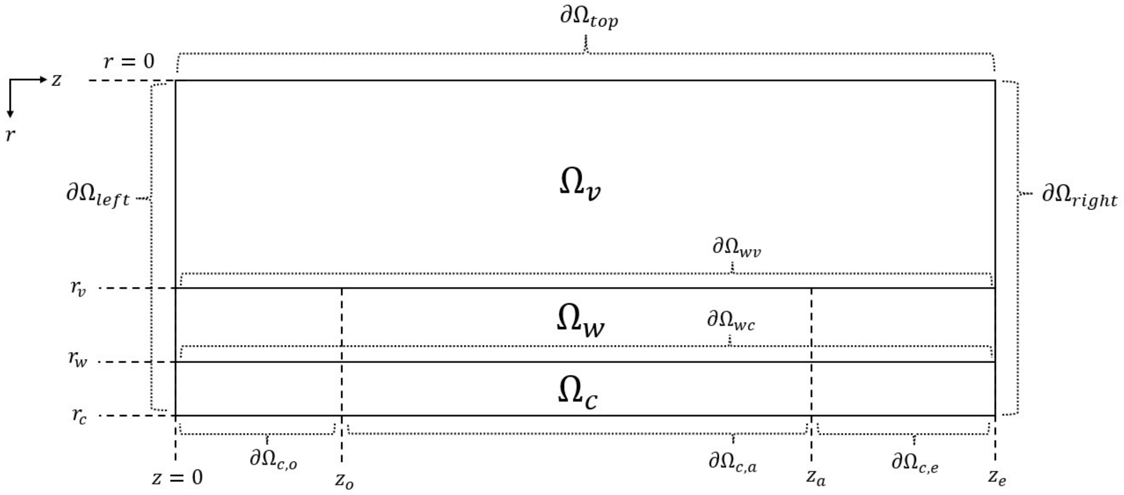

Figure 3.23: Geometry of interest for the steady-state model

The geometrical regions for the steady-state model have certain properties, and for water vapor, the properties are strong functions of temperature and pressure. For all purposes, the constant parameters used in the steady state formulation can be found in Table 3.3, and the varying properties are interpolated from the NIST database, Saturation Properties[1] for water.

3.2.1. Formulation

The first assumption that is critical to the formulation was axisymmetry, which was justified in the previous chapter. Another important assumption for the steady-state model was the saturation level of the wick. Under real operating conditions, an interface between the liquid and gas phases could occur inside the wick rather than the surface of the wick, and imply that a certain section is dried out, as investigated previously. The effects of multiphase flow were discussed in the previous chapter as well, but these are out of the scope of this part of the thesis, and the wick was assumed to be fully saturated during steady state operation.

The other fluid in the domain that must be investigated in a preliminary manner is the vapor. It is assumed that the vapor flow is laminar in the core, and the way to check if this assumption is valid is the dimensionless Reynolds number, Re. The maximum velocity of the gas from the results, $u_{max} = 23.6\ m/s$, is inserted retrospectively into the equation of calculating the Reynolds number, and the properties are chosen at the saturation conditions when the pressure is 2700 Pa. The characteristic length is the diameter of the vapor core, which is 7 mm, resulting in $Re = 330$. Although this is not a small value, $Re < 2400$ corresponds to laminar flow. As there is a vapor phase inside the system, two other crucial numbers must also be checked. The first one is the compressibility factor, Z, calculated as for saturation conditions at 2700 Pa as $Z = 1.0007$. This means that the ideal gas assumption holds valid at these conditions. The other number to check is the Knudsen number, Kn. At this pressure level, the speed of sound is 424 m/s, resulting in a Mach number of 0.06. The Knudsen number is then

---

[1] https://webbook.nist.gov/chemistry/fluid/

Table 3.3: Parameters of steady state formulation

Parameter	Meaning	Constant Value
r_v	vapor core radius	$3.5\ mm$
r_w	wick radius	$3.75\ mm$
r_c	casing radius	$4\ mm$
z_o	end length of condenser zone	$75\ mm$
z_a	end length of adiabatic zone	$300\ mm$
z_e	end length of evaporator zone	$375\ mm$
ρ_w	effective wick density	$4980\ kg/m^3$
ρ_l	liquid density	$997\ kg/m^3$
ρ_c	casing density	$8960\ kg/m^3$
c_{p_w}	effective wick heat capacity at constant pressure	$2285\ J/(kg*K)$
c_{p_c}	casing heat capacity at constant pressure	$385\ J/(kg*K)$
k_w	effective wick thermal conductivity	$40\ W/(m*K)$
k_c	casing thermal conductivity	$400\ W/(m*K)$
κ	wick permeability	$5E-10\ m^2$
ε	wick porosity	0.5
R_s	specific gas constant (water)	$461.5\ J/(kg*K)$
p_{ref}	reference pressure level (absolute)	$2621\ Pa$
T_{ref}	reference temperature level (absolute)	$295.1\ K$

calculated as $Kn = 2.6 \cdot 10^{-4}$. For $Kn < 0.01$, continuum mechanics holds strongly; thus, the physical approach is also justified.

The final assumption to include in the formulation is defining the vapor flow as compressible, rather than incompressible. It is already shown that $Ma = 0.06$, which theoretically justifies incompressible flow; however, as many other recent studies have considered compressible flow, this study will also go on with the consideration of the effects of density changes, and the results of it will be presented. It is also important to mention that by assuming compressible flow, the terms in the energy conservation equation become coupled. This has certain effects on the thermal results, which will also be discussed.

With all the justifications and assumptions made, the relevant equations regarding the conservation of mass, momentum, and energy will be defined. To enclose the system, an equation of state for the gas, which is the ideal gas law, is included. All necessary boundary conditions to solve the system are also presented. These equations and conditions were coupled and solved numerically in COMSOL Multiphysics 6.2. The computational approach will be discussed later in this section, after the mathematical modeling is presented. All the relevant results, as well as the comparisons to available literature results, will be presented in this section as well.

3.2.1.1. Governing Equations

Referring back to the geometrical depiction of the heat pipe in Figure 3.23, the governing equations and boundary conditions are put forward in this subsection. For building the system, multiple literature-based models were considered when defining the equations and conditions. The relevant ones can be listed as seen in Table 3.4, which the model of this thesis will be compared with. The relevant studies have been selected as they built their models depending on different assumptions, such as the inclusion of a liquid phase, the heat pipe type, and the system state. This provides a wide range of possible approaches to the problem, such that an accurate synthesis can be made when building the model, which is explained below.

The casing is a pure solid; thus, there is no momentum or mass conservation equation to solve for, and the Laplace equation is solved for the temperature. FA & PA use the same equation in its transient form as they conduct a transient study, whereas FB, TH, and LI use the same equation as this thesis. FC does not disclose the equation they've used, but states that they solve a pure conduction problem

Table 3.4: Related literature-based models

Research Group	Reference	Vapor	Liquid	Heat Pipe	Materials	State
Faghri & Chen [33]	FH	Compressible	No	Cylinder	Copper-Water	Steady
Faghri & Cao [68]	FA	Compressible	Yes	Cylinder	Copper-Water	Transient
Faghri & Buchko [34]	FB	Compressible	Yes	Cylinder	Copper-Water	Steady
Nat et. al. [69]	TH	Compressible	Yes	Cylinder	Copper-Water	Steady
Pan et. al. [18]	PA	Compressible	No	Cylinder	Steel-Sodium	Transient
Li et. al. [70]	LI	Incompressible	Yes	Loop	Copper-Water	Steady

for the casing and the wick sections. For the wick, the incompressible mass conservation equation is solved together with the Darcy equation in two dimensions. FB, TH, FA, and LI formulate the liquid flow through the full Navier-Stokes without neglecting the inertial terms and with the addition of the Darcy term, $u\varepsilon\mu/\kappa$. However, when the Reynolds number is low, the inertial terms can be neglected as viscous effects are dominant. Retrospective calculations show that the Reynolds number in the wick is in the order of 10^{-1} or lower, and thus, the inertial terms were neglected in this thesis for the liquid flow. For solving the heat transfer in the wick, FH and PA implement pure conduction; however, this thesis, as well as the other four studies, which include liquid flow, utilize the energy equation in a form accounting for both convection and conduction.

All six groups calculate the density and specific heat capacity of the wick through the method given in Eq.2.12. Other than LI, who calculates the effective thermal conductivity of the wick through a similar form of Eq.2.15, all research groups calculate the effective thermal conductivity of the wick through Chi's formulation given in Eq.2.14. This study does not calculate this value as it is already known; however, the closest approximation is Eq.2.15. The compressible Navier-Stokes equations were used in the same way in all research groups except LI, who consider the vapor to be incompressible. These equations were coupled with the ideal gas law in all six studies. The heat transfer in the vapor core was assumed to have the viscous dissipation term in all studies except FB and TH. FA, FH, and PA also consider work done by pressure change, which was also included in the thesis model.

Energy Conservation

$$\nabla^2 T = 0 \quad in \;\; \boldsymbol{\Omega_c} \tag{3.14}$$

$$\rho c_p \mathbf{u} \cdot \nabla T = k \nabla^2 T \quad in \;\; \boldsymbol{\Omega_w} \tag{3.15}$$

$$\rho c_p \mathbf{u} \cdot \nabla T = k \nabla^2 T + \mathbf{u} \cdot \nabla p + \boldsymbol{\tau} : \nabla \mathbf{u} \quad in \;\; \boldsymbol{\Omega_v} \tag{3.16}$$

Mass & Momentum Conservation

$$\left.\begin{aligned} \nabla \cdot \mathbf{u} &= 0 \qquad (3.17) \\ \nabla \cdot (-p\mathbf{I}) - \frac{\mu}{\varepsilon\kappa}\mathbf{u} &= 0 \qquad (3.18) \end{aligned}\right\} \; in \;\; \boldsymbol{\Omega_w}$$

$$\left.\begin{aligned} \nabla \cdot (\rho \mathbf{u}) = 0 \qquad (3.19) \\ \rho(\mathbf{u} \cdot \nabla)\mathbf{u} - \nabla \cdot \left(-p\mathbf{I} + \mu \left[\nabla \mathbf{u} + (\nabla \mathbf{u})^T - \frac{2}{3}(\nabla \cdot \mathbf{u})\mathbf{I} \right] \right) = 0 \qquad (3.20) \\ p = \rho R_s T \qquad (3.21) \end{aligned}\right\} \; in \;\; \boldsymbol{\Omega_v}$$

3.2.1.2. Boundary Conditions

The right and left boundaries are impermeable and adiabatic, the adiabatic section of the casing outer wall also has an adiabatic condition, and the axis of symmetry has symmetry conditions. These are commonly used conditions throughout all studies except LI, as their study investigated a loop heat pipe. The Dirichlet temperature condition at the condenser section is not used throughout the researched literature. Still, it is known that the Peltier element in a real system can sustain this temperature[2]. The heating through conduction condition is utilized in the studies of FB and PA. The other researchers define this condition as a heat flux in the form of Fourier's law rather than a heat rate, which COMSOL automatically calculates for. The no-slip condition is coupled with a continuous heat flux in the wick and casing domains, which must have the same temperature at the interface. The no-slip condition at this boundary is used by FA, TH, and PA only. FB uses a no-slip condition, too, but only for the z-component velocity. FH, FA, PA, and TH define heat flux continuity at this boundary, but FH is the only study to state that the temperatures on both sides of the boundary must be equal.

The Clausius-Clapeyron (CC) equation was used in this thesis as a condition to define pressure at the liquid-vapor interface, which in turn develops the flow field through COMSOL's $backflow$ option. PA also uses the CC equation in this pressure form for sodium, and LI calculates the slope of the CC equation to define a separate relationship and obtain a formula for the pressure drop that resembles Cotter's. All the other researchers use the CC equation to define the temperature at the interface instead of pressure. By doing so, they must close the system with velocity inlet/outlet conditions. These conditions in each of the studies are given in the form of

$$T^v_{wv} = \frac{1}{\frac{1}{T_{sat}} - \frac{R_s}{h_{fg}} \ln \frac{p^v_{wv}}{p_{sat}}}$$

$$u_v = \frac{k_v \frac{\partial T^v}{\partial r} - k_{eff} \frac{\partial T^l}{\partial r}}{\rho_v h_{fg}}$$

These conditions define that the temperature of the vapor at the interface location must be equal to the saturation temperature of the fluid at that pressure, and that the heat flux difference on both sides of the liquid-vapor interface must result in the phase-change mass flow rate $\dot{m}$. The latter condition restricts the flow field, and a more robust condition, given as the CC equation, was used in this study, which aims to relax the condition and give more freedom to the solver. The effects will be discussed later in this chapter. This study also takes into account the heat addition/subtraction due to phase change, depending on the signs of the velocity components. The second part of Eq.3.29 was used in FA, LI, and PA's models, which calculates the liquid flow velocity at the interface through the conservation of mass flux at the boundary. The first part, however, was only included in the study of TH. Following the formulation of the mathematical model, the computational implementation that solves this system will be put forward.

Table 3.5: Subscripts & superscripts of the boundaries and the conditions

Subscript	Meaning
v	vapor
w	wick
c	casing
e	evaporator
a	adiabatic
o	condenser
wv	wick-vapor interface
wc	wick-casing interface
p	pore

Superscript	Meaning
v	evaluated at the vapor side
w	evaluated at the wick side
c	evaluated at the casing side

---

[2] Will be mentioned in chapter 4

$$\partial\Omega_{left}\ \&\ \partial\Omega_{right}:\quad u = w = \frac{\partial T}{\partial z} = 0 \tag{3.22}$$

$$\partial\Omega_{top}:\quad \frac{\partial w}{\partial r} = u = \frac{\partial T}{\partial r} = 0 \tag{3.23}$$

$$\partial\Omega_{c,o}:\quad T = 295.15K \tag{3.24}$$

$$\partial\Omega_{c,a}:\quad \frac{\partial T}{\partial r} = 0 \tag{3.25}$$

$$\partial\Omega_{c,e}:\quad k_c 2\pi r_c (z_e - z_a)\frac{\partial T}{\partial r} = 20W \tag{3.26}$$

$$\partial\Omega_{wc}:\quad T^w_{wc} = T^c_{wc}\ ,\quad k_w\frac{\partial T^w_{wc}}{\partial r} = k_c\frac{\partial T^c_{wc}}{\partial r}\ ,\quad u = w = 0 \tag{3.27}$$

$$\partial\Omega^v_{wv}:\quad p^v_{wv} = p_{sat}\cdot exp\left[-\frac{h_{fg}}{R_s}\left(\frac{1}{T^v_{wv}} - \frac{1}{T_{sat}}\right)\right] \tag{3.28}$$

$$\partial\Omega^w_{wv}:\quad p^w_{wv} = p^v_{wv} - \frac{2\sigma}{r_p},\quad \mathbf{u_w} = \mathbf{u_v}\frac{\rho_{vapor}}{\rho_{liquid}} \tag{3.29}$$

$$\partial\Omega_{wv}:\quad k\frac{\partial T}{\partial r} = \rho h_{fg}|\mathbf{u}| \tag{3.30}$$

3.2.2. Implementation in COMSOL

The equations and boundary conditions given above were solved in COMSOL Multiphysics 6.2. This software is a common simulation package, especially powerful in multiphysics calculations. The geometry shown in Figure 3.3 was built in a 2D Axisymmetric environment in COMSOL. The properties of copper and water were imported directly from COMSOL's interface, and the porous material properties, shown in Table 3.3, were entered manually. The properties of steam (dynamic viscosity, density, heat capacity at constant pressure, and thermal conductivity) at the temperature range of interest were taken from the NIST database and then fitted into a second-order polynomial function of temperature with a 95% confidence level, which was then used for calculating the properties at the necessary conditions in COMSOL.

For the vapor flow, a *Laminar Flow* (*spf*) interface was used with the *Compressible Flow* option enabled. The boundary condition Eq. 3.15 was implemented as an $Inlet-Pressure$ condition with the *Suppress Backflow* option unchecked, which allows for mass to flow in and out freely. The liquid flow was modelled with the *Brinkman Equations* (*br*) interface, which solves for the velocity and pressure fields, whereas the $Darcy's\ Law$ (*dl*) interface solves only for the pressure field. This makes the former interface capable of coupling with $Non-isothermal\ Flow$, which is essential. For the heat transfer interface, $Heat\ Transfer\ in\ Porous\ Media$ (*ht*) is used; however, it should be noted that any (*ht*) interface is capable of solving the system as long as the correct domains are inserted. The porous medium is modelled with the *Equivalent thermal conductivity* node for heat transfer, assuming local thermal equilibrium between the solid and liquid phases. The two fluid flow interfaces were then coupled with the heat transfer interface through two separate $Non-isothermal\ Flow$ Multiphysics nodes, where the *Laminar Flow* interface has $Viscous\ Dissipation$ and $Kinetic\ Energy$ options enabled. For the meshing, a mapped method is used to generate rectangular elements, with boundary layers generated at the interfaces between the domains. The above-described system was solved with a *Stationary* study. This study node of COMSOL utilizes different types of solvers, in terms of linear and non-linear, and they are sometimes used together. The following subsections will go into the solution mechanism of COMSOL and the underlying fundamentals.

3.2.2.1. Finite Element Methods

The Finite Element Method, or FEM for short, is a numerical method for solving partial differential equation (PDE) systems, such as the one described in the governing equations part. This is achieved by discretizing the space domain into finite elements, which are called cells, and this is most often called ”meshing”. In these cells, the field variables are solved for, such as velocity (u). For linear problems, the system to solve generally looks like the form $[K][u] = [F]$, where $[u]$ is the velocity field to solve for, $[K]$ are the coefficients, and $[F]$ are the results. Combining multiple equations that involve multiple fields, however, most often leads to nonlinear phenomena as some fields can be coupled together, such as such as density being a function of pressure and temperature in ideal gases. This results in a nonlinear system of equations that looks like $[K(u)][u] = [F(u)]$, which most often cannot be solved in a single step of calculation like the one described above. These nonlinear problems, called system of PDEs, require a framework to be solved iteratively, which is essentially the purpose of COMSOL.

3.2.2.2. Solver Framework

The main framework of the *Stationary* study in COMSOL can be described in a few steps, as shown below, which will be defined in more detail afterward.

1. **Start:** Make an initial guess of all field variables, using the *Initial Value* nodes.
2. **Iterate**
    - **Non-linear Solver:** Calculate the residual of the whole solution with the current guess through Newton-Raphson iterations, and rebuild the Jacobian matrix
    - **Pass to Linear Solver:** The resulting Residual and Jacobian matrices are passed on to the linear solver for calculations
    - **Linear Solver:** The linearized system is solved for, and the approximate correction factor to the guessed solution is calculated
    - **Pass back to Nonlinear Solver:** The correction factor is passed back to the Nonlinear Solver, and the loop starts again
3. **Convergence:** Check at the end of each loop if the correction factor is smaller than the set error:
    - **Yes:** System has converged and found a solution
    - **No:** Repeat the ”Iterate” step

3.2.2.3. Nonlinear Solver

For the Nonlinear Solver, the Newton method was utilized, which is more commonly known as Newton-Raphson iterations. This is a root-finding algorithm that aims to approach the solution to a real-valued function by successively updating the approximation. A differentiable continuous function, f, dependent on the variable x, can be defined as $f(x)$. The first-order linear approximation to the value of this function, by defining a tangent line at the point $(x_{n+1}, f(x_{n+1}))$, can be defined as

$$f(x_{n+1}) \approx f(x_n) + f'(x_n)(x_{n+1} - x_n) \tag{3.31}$$

This is a fundamental equation for most solver algorithms, and is used throughout many different approaches, either directly or as a starting point. At the $x - intercept$ of this function, which means that $f(x_{n+1}) = 0$ (i.e., the root of a function), the equation can be written as $x_{n+1} = x_n - f(x_n)/f'(x_n)$. With an initial guess of x_n, often defined as x_0, the solution to the linear approximation can be calculated iteratively, assuming that the function value as well as the derivative value can be analytically calculated. When multiple variables, i.e., fields, are required to be solved for in a system, the same number of equations must be provided. This, in turn, results in a system of equations to be solved for simultaneously. This can be written as $\boldsymbol{x_{n+1}} = \boldsymbol{x_n} - \boldsymbol{F(x_n)/F'(x_n)}$.

Furthermore, the matrix $\boldsymbol{F'(x_n)}$ can be written as $\boldsymbol{J(x_n)}$, which is called the Jacobian matrix. This matrix has the first-order partial derivative of every function with respect to every variable, defined as $\boldsymbol{J(x_n)} = [\frac{\partial \boldsymbol{f}}{\partial \boldsymbol{x_n}}]$, and the above equation can thus be written as $\boldsymbol{J(x_n)}(\boldsymbol{x_{n+1}} - \boldsymbol{x_n}) = -\boldsymbol{F(x_n)}$.

This is the linearized system of equations that can be solved for with the linear solver of choice until the desired convergence is achieved, which means minimizing the difference $\boldsymbol{x_{n+1}} - \boldsymbol{x_n}$ at each iterative step. COMSOL further improves the method by reducing the step size between the iterations by an adaptive ”dampening factor”, which protects the system from diverging quickly from the roots when the problem is highly nonlinear.

3.2.2.4. Linear Solver

The linear solver of the system was PARDISO (Parallel Direct Solver). As seen in Eq. 3.21, the system highly resembles the definition $[K(u)][u] = [F(u)]$, which is essential to the linear solver. Here, the matrix K is the Jacobian, provided by the Nonlinear Solver. By completing the matrix multiplication, the new value of F can be calculated. However, these matrices are often very large and have to be manipulated. The PARDISO solver does this by applying a LU decomposition to the Jacobian matrix. This means that the original matrix is defined by the multiplication of two matrices, which are lower (L) and upper (U) triangular matrices. This can be defined simply for a 3 by 3 matrix as

$$\boldsymbol{K} = \boldsymbol{LU} = \begin{bmatrix} L_{1,1} & 0 & 0 \\ L_{2,1} & L_{2,2} & 0 \\ L_{3,1} & L_{3,2} & L_{3,3} \end{bmatrix} \begin{bmatrix} U_{1,1} & U_{1,2} & U_{1,3} \\ 0 & U_{2,2} & U_{2,3} \\ 0 & 0 & U_{3,3} \end{bmatrix} \tag{3.32}$$

By doing so, the multiplication procedure can be manipulated. As the matrix multiplication is now $[\boldsymbol{L}][\boldsymbol{U}][\boldsymbol{u}] = [\boldsymbol{F(u)}]$, the first step is to state that $[\boldsymbol{U}][\boldsymbol{u}] = [\boldsymbol{y}]$, and solve $[\boldsymbol{L}][\boldsymbol{y}] = [\boldsymbol{F(u)}]$. This is much simpler to solve for $[\boldsymbol{y}]$ when $\boldsymbol{L}$ is a lower triangular matrix, as it can be done through forward substitution. After $[\boldsymbol{y}]$ is calculated, $[\boldsymbol{U}][\boldsymbol{u}] = [\boldsymbol{y}]$ is solved for using back substitution, due to $[\boldsymbol{U}]$ being an upper triangular matrix. PARDISO further increases the efficiency of this method by parallelizing the separation of the matrices and calculation of the multiplications into multiple computer cores. One thing to consider is the capabilities of the computer, as the size of the matrix grows with the degrees of freedom for the system, and rapidly becomes a constraining factor in computational methods.

3.2.2.5. Convergence of the Spatial Discretization

As space is discretized in FEM models, it is important to understand at what level space has been discretized ”enough”. Most often, a mesh convergence study must be done to prove that the results do not depend on the spatial discretization any further. To do so, the system is meshed with a certain detail and solved for. As the mesh quality is increased iteratively, the solution accuracy is expected to increase as well. At one point, a higher mesh quality will ideally not give a significant increase in solution accuracy, and thus, the mesh can be assumed to have converged. The solution accuracy is usually chosen as a variable in the system, which is a value of interest to the user.

Before any results are put forward, it should first be justified that the simulation is accurate enough to represent the given system. To do so, the simulation was completed for 9 different mesh sizes. The value that is most essential to heat pipes is the temperature difference between the two sections where heat is transferred, the condenser and the evaporator. The average temperature at the outer walls of these sections, at $\partial\Omega_{c,o}$ and $\partial\Omega_{c,e}$, was calculated through COMSOL, which sums the temperature over each mesh node and divides by the node count. Calling this value ΔT, the change of it versus the mesh size can be shown as in Table 3.6.

Table 3.6: Value of averaged ΔT wrt. mesh elements, final mesh for the results is mesh #7

Mesh Number	Mesh Elements	ΔT	Relative Change (%)
1	2775	0.3051	—
2	5000	0.3010	1.34
3	10000	0.2978	1.06
4	13000	0.2971	0.24
5	24375	0.2966	0.17
6	41250	0.2960	0.20
7	**85500**	**0.2955**	**0.17**
8	172500	0.2954	0.034
9	308000	0.2954	0

This mesh convergence study result is crucial to have, as it shows that the iterative increase in result accuracy does not change significantly after the 7th mesh level, and the spatial discretization can be assumed to have converged. For efficient calculation time and result accuracy, this was the chosen mesh, which was used for obtaining the results of the following subsections.

3.2.2.6. Convergence of the Nonlinear Solver

By repeating the information transfer and matrix multiplications mentioned previously, the solver aims to find the solution to the fields of the system. Evidently, for nonlinear systems, finding a solution by hand is simply too difficult in most cases, which is why FEM methods are utilized. Inherently, these methods will have finite error as the solution is an approximation, which was first mentioned in the $Nonlinear\ Solver$ subsection, and a criterion for stopping the calculations must be defined. This is called the ”error” or ”tolerance”, and has many different alternatives for calculating. For convergence criteria, it is most often defined as

$$e_r = \frac{x_{n+1} - x_n}{x_n} \tag{3.33}$$

This method of calculating error is called the relative error, as the magnitude of error is independent of the magnitude of the variables, which is a more robust and consistent way of calculating error.

At the mesh quality defined in the previous subsection, the convergence of the simulation can be seen as in Figure 3.24. Clearly, the relative error reaches a value of approximately 10^{-5} descending rapidly from It. 12 to It. 16. The convergence condition given to the system was 10^{-4}, and the system reached an even lower value, which implies successful convergence. These two convergences show that the mesh and the solver have reached a reasonably accurate level; thus, the results are justifiably correct with respect to the model built.

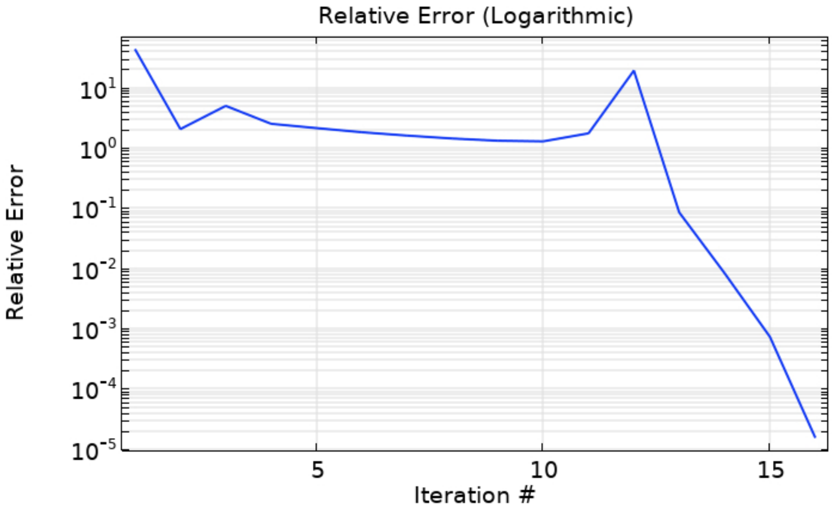

Figure 3.24: Relative error at each iteration for Mesh #7, for the nonlinear solver

3.2.3. Numerical Results

The main results to investigate are the temperature, velocity, and pressure profiles. Certain line plots are also necessary to understand the behavior of the compressible vapor flow and the flow inside the wick. These findings will first be presented and compared with the literature, qualitatively and quantitatively, when possible. Before the results of the simulation of the heat pipe this thesis investigates is put forward, a validation study must be completed. This ensures that the model is in good agreement with other models in the literature, and can be assumed to be accurate.

3.2.3.1. Literature Validation Study and Results

For a quantitative comparison, the heat pipe that Faghri & Chen's computational model [33] investigates was implemented, which is a copper-water sintered wick heat pipe. Their study investigated a heat pipe that was heated in two locations rather than one, i.e., it has two evaporator sections. The relevant parameters that were used in the validation study can be found in Table 3.7. As seen, the two evaporator sections exist at the locations between $z = 0$ and $z_{e1,end}$, and $z_{e2,start}$ and $z_{e2,end}$, respectively. The condenser section exists between $z_{c,start}$ and $z_{c,end}$. The total length of the heat pipe is thus 1500 mm.

Table 3.7: Important parameters of the literature validation study

Parameter	Value in Validation Model
r_v	11 mm
r_w	11.76 mm
r_c	13.36 mm
k_{eff}	240 $W/(m * K)$
ε	0.3
κ	$1E - 7$ m^2
$z_{e1,end}$	100 mm
$z_{e2,start}$	500 mm
$z_{e2,end}$	600 mm
$z_{c,start}$	900 mm
$z_{c,end}$	1500 mm
Q_{e1}	200 W
Q_{e2}	800 W
Q_c	-1000 W

The differences in the governing equations and boundary conditions between the current study and Faghri & Chen's study were discussed previously. Their results investigate the pressure change at the liquid-vapor interface, although it is noted that they do not have a liquid phase. They also present the wall temperature at the outer surface of the casing. The results obtained by them, compared with the results obtained from the model presented in this chapter, can be found in Figure 3.25 and Figure 3.26.

As seen from the first figure, the pressure results match exceptionally well. Until the end of the second evaporator section, the values are approximately the same, and the total pressure drop in the second adiabatic section has a visible difference. This difference is not reconciled in the condenser section, but the difference does not increase throughout that section either. As both studies solved for the vapor phase as an ideal gas and compressible flow, considering viscous dissipation, the strong correlation is expected. In the second figure, however, certain mismatches are observed. The general trend, as well as the peak locations, fit well, yet the values do not. Still, the relative error between the peak values is 0.2%, which is negligible. It is important to note that the figure provided by Faghri & Chen is not high in quality, and is objectively difficult to interpolate values. Certain noisy behavior, especially observed in the second adiabatic section, could perhaps be due to the plot digitalizing scheme used.

Although the authors do not share the velocity field result, the current model calculates the vapor velocity magnitude as in Figure 3.27. It is crucial to further emphasize the governing mechanism of

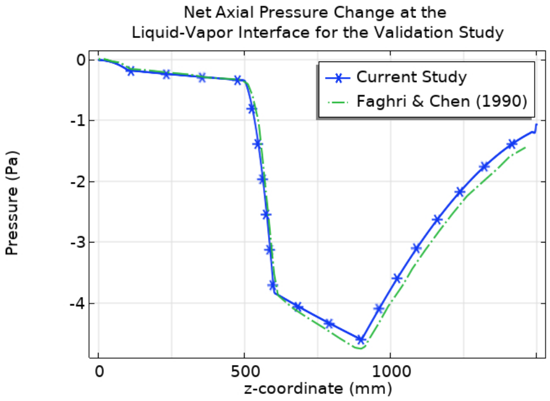

Figure 3.25: Pressure result comparison of the validation

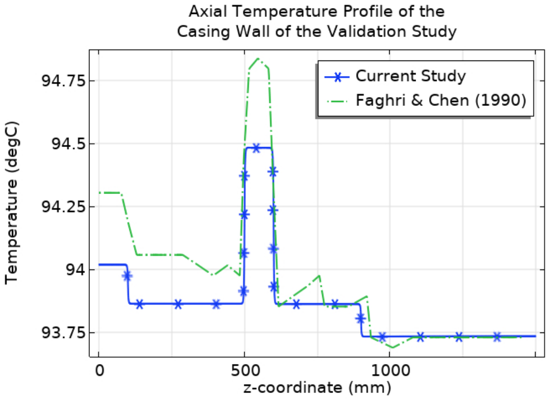

Figure 3.26: Temperature result comparison of the validation

heat pipes, which is the phase change phenomenon. In the second evaporator section, which has 4 times higher heat flux input than that of the first evaporator section, the velocity of the vapor reaches its peak value. This peak velocity is much lower than the one found for the heat pipe this thesis considered, but it is expected, as the vapor core diameter is approximately 3.15 times larger, leading to a mass flow area that is approximately 10 times the heat pipe of this thesis. Furthermore, the temperature level is also much closer to atmospheric conditions, which leads to densities that are up to 20 times the results of this thesis. The combined effect of denser vapor and larger flow area leads to a much slower vapor flow velocity; however, it is also worth mentioning that the total heat input is 50 times that of this thesis's heat pipe. The combined effect leads to a rough estimate that the vapor velocity should be one-fourth of the value of this thesis's results. The actual value is closer to one-fifth, yet it shows that even a back-of-the-envelope calculation can give a rough estimate that is not too far off from the values of the respective simulations.

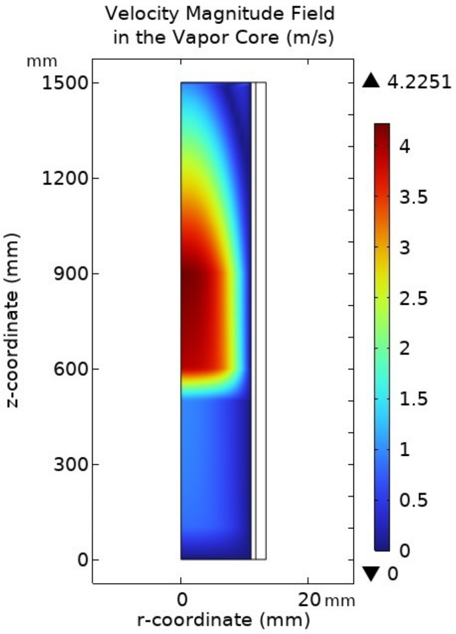

Figure 3.27: Velocity field of the validation study

3.2.3.2. Temperature, Velocity, and Pressure Field Results of the Heat Pipe of this Thesis

The original aspect ratio of 94:1 for the heat pipe is not sufficiently visible and clear for presenting the results. Thus, the result figures that contain the geometry of the heat pipe in 2D have been changed in aspect ratio by a factor of 1:25 in the radial direction, such that a comprehensive understanding is possible (final aspect ratio is 4.6785:1).

The two main result fields important to the study are the temperature and velocity fields, especially in the vapor core. As seen from Figure 3.28, the evaporator section observes the highest temperature overall. The condenser observes approximately the lowest temperature as well, which would've been expected. However, an interesting point to mention is that the coldest temperature is not observed at the condenser but at the vapor core. At approximately where $r = 0$, $z = 75mm$, the flow is at its peak velocity magnitude, seen in Figure 3.29. Due to conservation of energy, the increase in velocity, which increases the kinetic energy of the local vapor, must be reconciled through the reduction of internal energy, governed by the temperature of the vapor. Due to this balance, the vapor cools down considerably in the core of the heat pipe. This effect will be investigated later in this subsection.

The average temperature at the outer wall of the casing at the evaporator is $22.295°C$, and the condenser temperature is known to be $22°C$ as it is a Dirichlet condition. Following Eq.1.1, the thermal resistance of the heat pipe with an input of 20 W is found to be $R_{hp} = 0.0148\ K/W$. The effective thermal conductivity of the heat pipe can also be calculated through Equation 1.2, assuming Δx is the effective length l_{eff}, which results in approximately $k_{hp} = 404\ kW/(m * K)$.

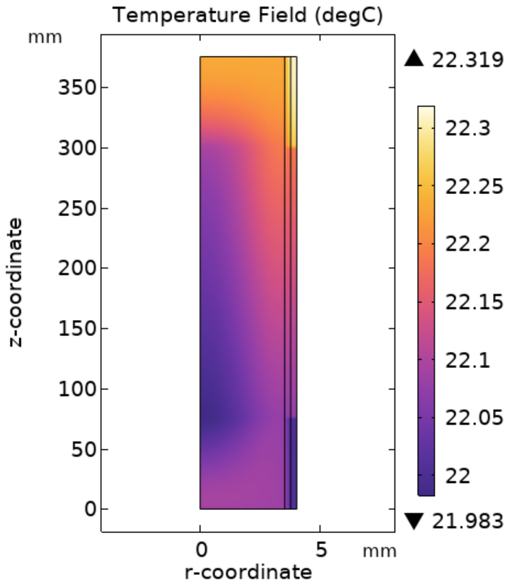

Figure 3.28: Temperature field

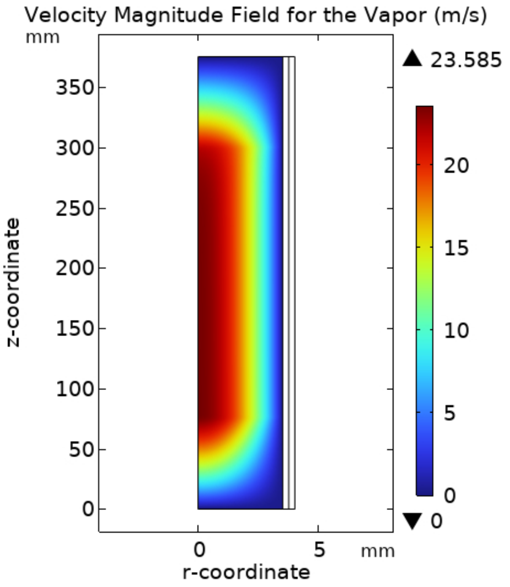

Figure 3.29: Velocity magnitude field for the vapor

The vapor velocity profile also strongly resembles a Poiseuille flow, especially in the adiabatic section. This was expected, especially when compared with the literature formulations presented in Section 2.1. The slender profile of the heat pipe allows the flow to fully develop, and the reduction in velocity, especially near the ends where the vapor is accelerated/decelerated, is clearly observed. As mentioned in the subsection where boundary conditions were presented, defining an inlet and outlet velocity for the interface is commonplace in the literature. It is seen in Figure 3.30 that defining a pressure condition instead through the CC equation, while allowing backflow in COMSOL, essentially results in the same velocity profile. The noisy behavior at the end sections is possibly due to the sharp corners in the geometry, which cause minor stability issues. It is also observed that where the condenser and evaporator sections are connected to the adiabatic section, the velocity gradient is not an infinitely sharp increase but a curve. Defining a strict velocity condition requires a gradient change instead, which can cause stability issues and lead to non-convergence.

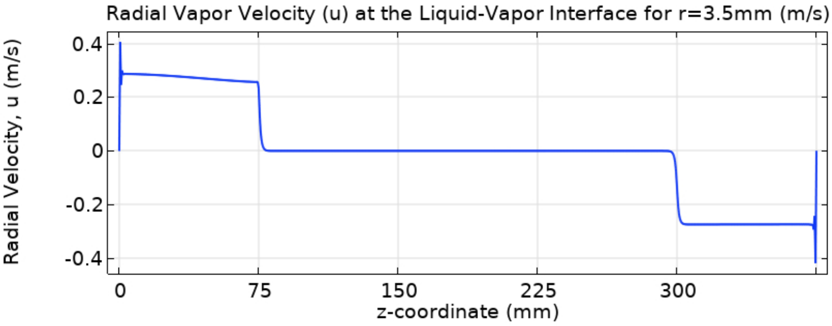

Figure 3.30: Vapor velocity at the liquid-vapor interface

When Figure 3.31 is investigated, the pressure drop in the evaporator section can be found as 6.45 Pa, and the recovery in the evaporator can be found as 1.3 Pa, giving a recovery of 20%. Cotter's theory suggested that the pressure drop observed in the evaporator can only be recovered approximately 40% in the condenser section. Cotter gave this theoretical limit for pressure recovery for $Re \gg 1$. The radial Reynolds number at the evaporator section exit is 1.9, which fits with Cotter's Reynolds number limit, yet the recovery does not match his expectation of 40%, and is approximately half of it. The pressure drop of the vapor phase, calculated through Equation 2.7 for $\dot{m} = \dot{Q}/h_{fg} = 8.85E-6\ kg/s$, can be found as 22.52 Pa. As seen from Figure 3.31, the vapor core has a total pressure drop of 23.25 Pa, which shows that the approximation is accurate in this case. Cotter's formulation Equation 2.8 results in a value of 17.5 Pa, which is farther off than the commonly used formula. This can be explained by the fact that the heat pipe is very slender; thus, the dominant pressure drop is a linear Hagen-Poiseuille pressure drop, which is closer to Equation 2.7. Plugging in the calculated Re_r into Bankston & Smith's calculations in Figure 2.8 gives an expected result of 9 Pa, which is the farthest prediction among all. Their results were fitted for a wider range of possible radial Reynolds numbers, which might lead to the underlying reason for being the most inaccurate prediction overall.

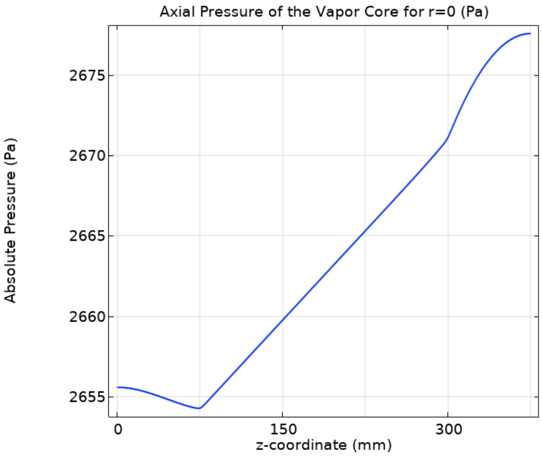

Figure 3.31: Vapor core pressure

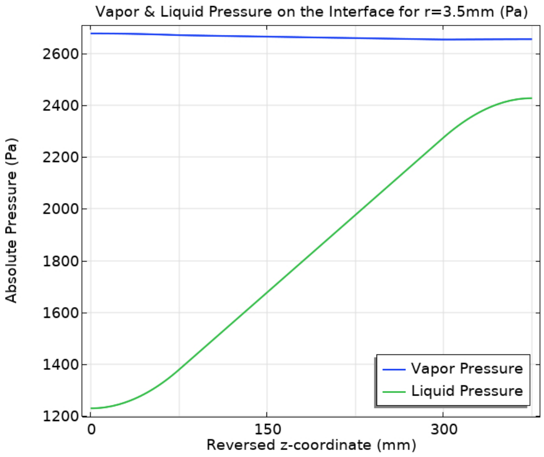

Figure 3.32: Pressure jump at the interface

The resulting pressure profiles for both phases at the interface can be seen in Figure 3.32. The profiles match the theoretical expectations well, corresponding to Figure 2.11. There must exist a pressure gap between the two phases due to the existence of surface tension. By setting a pressure jump at the point of maximum capillary pressure difference, the results can give a crucial understanding of the system. Evidently, from the governing equations and boundary conditions, the phase change phenomenon is included in a simplified way, rather than a full modeling of the molecular kinetics. By doing so, the crucial condition to have satisfied is that the liquid pressure must not be higher than the vapor pressure at any point, although it is possible in cases with very high Re_r, which Bankston & Smith have investigated [27]. This thesis successfully satisfies this condition, and there still exists a gap between the two phases, even at the condenser section. As shown in Section 2.1.5, the surface tension pressure jump at the condenser is often neglected (or approximated as zero), which in most physical cases, will not be the case, especially for wetting phases. This pressure jump fits the depiction in Figure 2.11 accurately, and it also implies that the permeability of the wick could essentially be lower, which would result in a higher liquid pressure drop.

It is seen that the liquid pressure drop is approximately 800 Pa in the simulation. The result of calculating Equation 2.3, however, gives 887 Pa. The underlying reason is that the Darcy law approach gives a constant velocity profile for a certain length, in this case l_{eff}. Yet, there are entry effects at the evaporator and condenser sections that will not be fully reconciled through such an approximation, which possibly contribute to this reduced pressure drop in the simulation. Furthermore, when investigating Figure 3.33, it is seen that the velocity resembles an internal Poiseuille flow, especially after $z = 75\ mm$. This is due to the no-slip condition at the interface between the casing wall and the wick, and the velocity coupling between the vapor and liquid phases at the liquid-vapor interface, which essentially serves as a no-slip condition too. The velocity, ramping up over the condenser section, is also observed clearly. Knowing that the heat transfer dominant sections will observe different flow profiles than the rest of the system is an accurate assumption of the literature approximation l_{eff} for certain calculations. It can be stated that it is a practical tool for preliminary analyses; however, it has an inherent inaccuracy. The maximum velocity of the liquid in the wick is 2 mm/s, which results in a Reynolds number much lower than 1, as mentioned before, which essentially justifies the assumption of creeping flow, and thus the neglecting of the inertial terms.

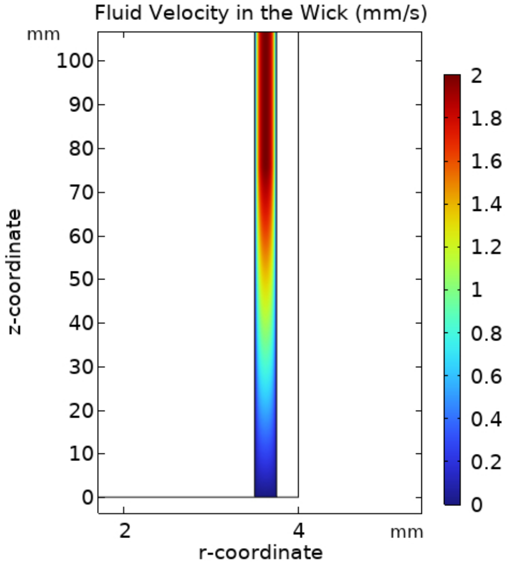

Figure 3.33: Liquid flow profile in the condenser section of the wick

Operating Limits As explained in Section 2.2.5, the operating limits of a heat pipe are also crucial to understand. By investigating Figure 3.32, it is seen that the limits are not reached. Utilizing Equations 2.17-2.20, the limits can be calculated as functions of temperature, and the capillary limit is calculated through the manipulation of Equation 2.11. By doing so, and multiplying the heat fluxes with the correct surface areas, Figure 3.34 is obtained. This figure shows the various limits and their behavior with respect to temperature. As seen, the plot resembles the arbitrary heat pipe performance map, given by Figure 2.12. One factor that stands out is the level of the capillary limit. This limit, calculated through the values this thesis utilized, is a severe restriction on the operation of the heat pipe. At the conditions of 298 K, the capillary limit is approximately 43 W. Even though this value is above the operating power of 20 W, the limit being considerably close to the operating power becomes a significant concern, especially in the case of possible sloshing.

Furthermore, the permeability value of the wick is uncertain. As shown in the figure, an order of magnitude increase in the permeability relaxes the operating limits significantly. However, an order of magnitude reduction basically renders the heat pipe inoperable. This emphasizes the importance of the capillary limit and how crucial the wick is to the operation of the heat pipe.

A more qualitative analysis of the limits, without considering the capillary limit, shows that the boiling limit is the constraining factor at high temperatures, and the viscous and sonic limits at low temperatures. This is certainly expected and is a verification of the theoretical analysis of heat pipes.

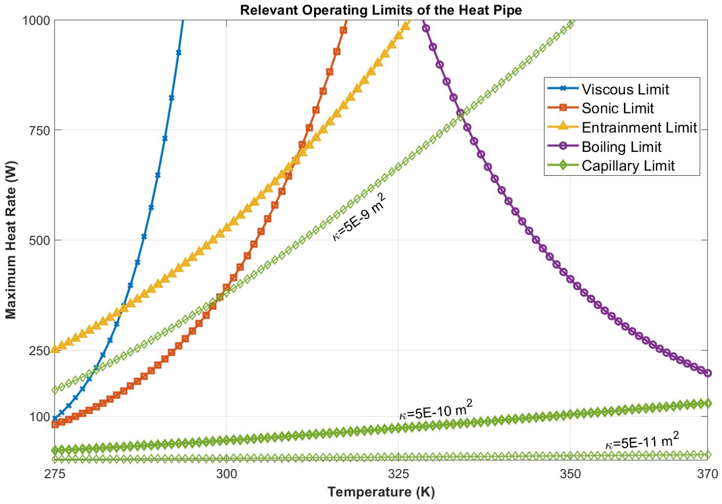

Figure 3.34: Operating limits of the heat pipe of the thesis

As mentioned for the temperature results, the cold temperature in the heat pipe vapor core must be analyzed further. In the aim of doing so, the relationship between the Mach number and the temperature at the core of the heat pipe was visualized. The results can be seen in Figure 3.35. The Mach number is inversely correlated to the temperature of the fluid, which is evident in the figure. Only at the end of the condenser section is the relation different, which is possibly an end effect of having a sharp corner. Pan et. al. have studied a sodium heat pipe with different dimensions, with the same analysis for the Mach number and temperature in the vapor core axis of symmetry, as seen in Figure 3.36.

The qualitative comparison shows that the peak velocity is indeed achieved for the coolest vapor temperature in both studies. Pan's shorter adiabatic section, compared with the other sections in their heat pipe, results in a shorter transition region between the increasing and decreasing sections of the figure. The overall comparison of the two results matches well, and although Pan et. al. do not go deeper into their result, this effect is noted to be caused by the conservation of energy. This occurs as the sum of the kinetic energy of the gas, governed by velocity, and internal energy, governed by temperature, must be constant. Thus, a higher velocity gas results in a colder temperature, and vice versa.

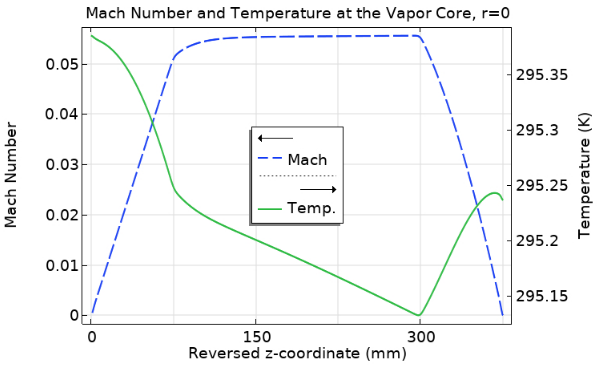

Figure 3.35: Results of this thesis

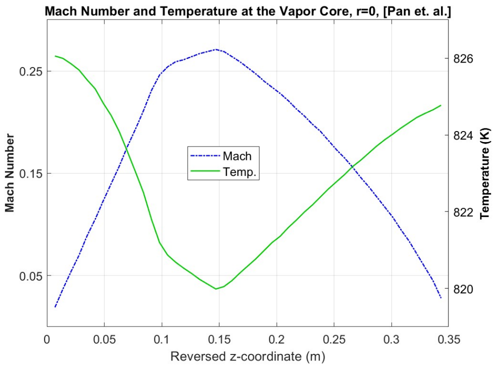

Figure 3.36: Results of Pan et. al. [18]

4

Conclusions & Recommendations

The thermal effects of large axial accelerations on heat pipes are a topic of interest in the literature. Researchers experimentally found complex and varying evidence on the different effects of such accelerations. One of the most crucial factors that affected the results in these studies was the wick configuration. Although experimental results that display these effects are abundant in the literature, a state-of-the-art modeling of the underlying physics that outputs the observed effects has not been done.

This thesis splits the larger problem of explaining these literature observations into two sub-problems. The first sub-problem builds a mathematical model to explore the reason why liquid leaks out of a sintered-powder wick under the effects of a sinusoidal acceleration profile, i.e., sloshing. Following the reasoning of this "leakout", possible fluid flow regimes for the leaked liquid inside the heat pipe were mathematically defined and analyzed. The estimated thermal effects of such flow regimes were also discussed. The lack of modeling and investigation in the literature posed a multitude of difficulties and limited the level of accuracy of these mathematical models.

The second sub-problem builds the steady-state operation model of a heat pipe mathematically and implements it computationally in COMSOL. This model aimed to be validated against the literature and give insight into the inner multiphysical operation of heat pipes. It also serves the purpose of being the starting point of the computational model that would accurately represent the dynamics of a sloshing heat pipe.

This chapter of the thesis summarizes the key results of the previous chapter, discussing key findings. The implications for research on heat pipes are presented, along with the difficulties, limitations, and shortcomings of the models. Recommendations for future studies, in terms of the next steps to follow, and possible experimental works which could shed light on this pioneering topic are also listed.

4.1. Overview of Key Findings

This section puts forward the main findings of this thesis. These are ordered to answer the research objectives defined in chapter 1, and the findings are supported by the results of the previous chapter.

4.1.1. Estimated Thermo-fluid Effects of Sloshing on Heat Pipes (RO1)

The dynamics of the system due to a sloshing motion were investigated. Sloshing was induced by a sinusoidal acceleration applied to the heat pipe with a magnitude of 400 m/s^2, and a period of 0.05 s. Important timescales were obtained for leakout and rewetting through mathematical models. These findings are summarized as follows:

1. **Leakout:** Permeability of the wick and the leaked liquid mass are positively correlated. A mathematical relation that accurately captures the dryness of the wick with respect to the permeability, κ, was obtained, given by $Dryness\ (\%) = 98.07(1 - e^{-\zeta\kappa})$, for $\zeta = 1.933 * 10^{11}$ $[m^{-2}]$. For permeability values of the wick above $1 * 10^{-12}$ m^2, the evaporator section of the wick possibly experiences complete dryout due to sloshing. A permeability value over $3 * 10^{-11}$ m^2 potentially

causes complete dryout of the entire wick. The relevant timescales of these drying phenomena are in the order of 10^{-2} s. Dryout of the evaporator is expected to cause a severe performance reduction, and complete dryout of the wick could be catastrophic to the heat pipe.

2. **Pool Build-up:** The liquid that leaks out of the wick could develop into a reverse axisymmetric stagnation flow in the center of the vapor core wall, and create a jet in the direction of the acceleration. Assuming a cylindrical laminar flow for this flow regime does not result in high velocities for the jet. This limits the distance the liquid can travel and is not expected to have a significant impact on performance. Rayleigh-Taylor instabilities could generate during the deceleration phase due to an unstable base state of the fluid phases. These instabilities could grow exponentially in timescales of 10^{-3} s. The expected Reynolds number of the instabilities in the order 10^5 suggests a turbulent flow in the vapor core. Due to possible turbulent mixing, thermal performance can be improved compared to the complete dryout state, and the inertial movement of the liquid can aid in the rewetting of the wick.
3. **Rewetting of the Wick:** The dried wick can be rewetted by the liquid movement in the vapor core, potentially enhancing the heat pipe operation and re-establishing the thermal performance. The rate at which this happens is found to crucially depend on the wick permeability. A simple proportional relation between the change of rewetting time and the permeability is found as $\kappa \propto t^{-2}$. For a permeability value of order 10^{-12} m^2, the rewetting timescale of the wick is found to be in the order of 10^{-4} s. A trade-off between rewetability and proneness to leakout is observed, rooted in the wick permeability.

The relevant timescales indicate that the leaking phenomenon is a slower process compared to rewetting and instability growth. These findings overall suggest that the leaked liquid can support the thermal performance of the heat pipe when it is subjected to leakout.

4.1.2. Steady-State Modeling of a Heat Pipe (RO2)

The mathematical model built for the steady-state operation of a sintered-wick copper-water heat pipe considered the solid casing, the liquid flow inside the wick, which was modeled as a porous medium with a Darcy flow, and the laminar compressible vapor flow inside the vapor core. The model aimed to relax and improve the system of equations by applying the Clausius-Clapeyron equation as a pressure condition at the liquid-vapor interface. This approach replaced the temperature and velocity boundary conditions at the same interface that literature models utilized. The inclusion of the pressure jump due to surface tension was also implemented at the evaporator section.

The model was ensured to converge both in terms of the spatial discretization scheme and in the residual error of the nonlinear solver. A quantitative literature validation of the model was done, and the results between this thesis and the literature values are in very good agreement, as shown in Figure 3.25 and Figure 3.26. A qualitative analysis of the fluid phase pressures with respect to theory also matches well, comparing Figure 3.32 and Figure 2.11.

The overall agreement of the results with respect to the literature supports the modeling improvements made in this thesis for heat pipes in steady-state operation. The results also show that the overall thermal resistance of the heat pipe is $R_{hp} = 14.8$ mK/W, and the effective thermal conductivity is $k_{hp} = 404$ $kW/(mK)$. These values further support the claim of using heat pipes in industry, although the values are noted to be ideal.

4.1.3. Coupled Dynamic Model of a Heat Pipe under the Effects of Sloshing (RO3)

The third research objective aimed to combine the validated steady-state model and incorporate the expected dynamic effects into it, such that a transient model representing the thermal effects of sloshing was obtained. However, the coupling between the two main research objectives was not achieved, as will be explained in the section going through the limitations of the study. It is, however, expected that the results of the first research objective, described above, will shed some light on the topic and give an initial understanding of what to expect from the future completion of this research objective.

4.2. Implications for Heat Pipes

The findings show a pathway to heat pipe wick configurations that can sustain thermal performance in adverse acceleration conditions. The work done in this thesis also challenged certain conventional methods of heat pipe modeling in steady-state to identify possible improvements. These have possible applications in the heat pipe research area.

4.2.1. Choosing a Heat Pipe Wick

One of the most significant contributions of this thesis is the exponential relation obtained between the permeability and the expected leakout amount. It is noted that this fit is accurate only for this type of wick; however, the form of the equation suggests that it can be fit for any wick, given that the model and its results are correct. The existence of a possible leakout due to the interface between the liquid-vapor phases being broken through is justified to be plausible for sintered-powder wicks, caused by large axial accelerations. To prevent significant leakout, a low permeability value must be chosen, which is also proportional to smaller pore sizes in a porous wick. This inhibits a leakout behavior and lowers the possibility of the existence of the dynamic scenarios investigated in this thesis. However, it is noted that a lower permeability directly affects the pumping pressure of the liquid and the capillary limit, which are crucial terms to control.

Another important contribution of this thesis is the investigation of the timescales related to leakout, instability growth, and rewetting. The proportional relation between the permeability and rewetting time suggests that if a sintered-powder wick is to be used, a high-permeability wick should be chosen when the system is exposed to large axial accelerations, while taking into account the capillary pumping pressure. This allows for a shorter rewetting time, which can aid the heat pipe in returning to optimal operating conditions. In such a situation, however, the wick essentially loses its purpose as the main liquid pumping mechanism. The shorter timescale of instability growth compared to leakout also suggests that the vapor core fluid regimes can support the rewetting of the wick.

Under the light of these suggestions, it is evident that the choice of the wick is crucial to the heat pipe's operation in the presence of sloshing. The opposing behavior of the wick permeability with respect to proneness to leakout and rewetting time indicates that a best-of-both-worlds solution cannot be found for sintered-powder wicks. Wickless heat pipes, for example, can be a good candidate as they allow for complete freedom of the liquid movement, known as thermosiphons. The results of Thomas et. al. [50] also show promising behavior for helically grooved heat pipes under large accelerations, which is also recommended to be investigated further.

4.2.2. Building a Steady-State Heat Pipe Model

It was demonstrated that the pressure Clausius-Clapeyron equation, given in Eq.3.28, serves as a successful substitute for the conventional velocity condition at the liquid-vapor interface, which is commonly used in computational models of heat pipes. It also simultaneously handles the saturation condition relation between temperature and pressure at the interface. Thus, it is a recommended alternative boundary condition as it relaxes the system and provides more freedom to the computational solver, while also resulting in the same expected behavior in terms of the velocity and temperature profiles. It is noted that the model was built in COMSOL, utilizing a specialized flow node called $backflow$.

The inclusion of the surface tension pressure jump at the evaporator section, given in Eq.3.29, also resulted in pressure profiles that qualitatively agree with literature representations. This boundary condition can further serve as a verification of the capillary limit in heat pipes, as a higher-pressure liquid will not allow vapor to flow towards it in the condenser section, and the simulation will not converge, implying that the heat pipe will not operate at the given conditions.

These two conditions that were implemented in the mathematical formulation build on the common literature models found in the steady-state modeling of heat pipes. Their combined utilization can possibly increase the physical accuracy of the simulations and reveal behaviors not considered previously. Thus, they are recommended for consideration and implementation, where applicable.

4.3. Limitations of the Thesis

The work done in the thesis was limited by a set of obstacles and crucial modeling decisions. These are necessary to understand as they define the limits and suggest further possible work. As the thesis investigated two sub-problems, the relevant limitations will be covered separately.

4.3.1. Mathematical Modeling of the Dynamics

The mathematical modeling of the effects of sloshing was severely limited. Firstly, the calculations and modeling were done purely in 1D, further simplifying the axisymmetric assumption of the heat pipe geometry. The definition of the pressure terms that formulate the leakout phenomenon stems from simple physical analogies, and because hydrostatics will not hold for a moving fluid, the formulation of the mathematical model could be completely mistaken. The definition of a flat interface between the two fluid phases is also a strong simplification, as the point that corresponds to the expected flow regime inside the porous medium lies close to capillary fingering, which is a much more complex flow regime compared to the one this thesis investigated.

The resulting leakout mass flow, modeled with a Darcy term, assumes uniform velocity at the exit of the porous medium; however, velocity might not be uniform. Specifically, it makes more sense that the leakout velocity is higher where the pressure is higher in the fluid, which was not taken into account. The leakout was also considered to happen only and always at the condenser section, irrespective of the acceleration sign. The existence of an interface inside the wick suggests that, along with leakout, there could be a low-velocity Darcy flow towards the evaporator, which is essentially the working principle of the heat pipe. This was neglected, along with the fluid flow that would be included if the heat pipe were operating.

The effects of temperature were not considered either, which could lead to changes in the fluid properties. These effects would be significantly increased if the operation of the heat pipe were included, too. Even more so, if the temperature of the wick increased significantly during dryout due to the lack of phase-change heat transfer, evaporation at a section other than the evaporator can be observed; this was not modeled. There is also a possibility that the increasing temperature of the wick due to dryout, and subsequently the vapor core, will increase the vapor pressure. This changes the saturation conditions and, more importantly, the vapor density. All of these factors, which crucially depend on the temperature of the system, were not considered.

The script that solves for $H(t)$, and correspondingly the dryness, utilizes a Forward Euler time-stepping scheme and a simple loop. It was observed that the time discretization level, dt, gives consistent results at the current level in the script, and this limit does not change with changing the time step size, dt, nor with higher permeability values. It was observed, however, that for higher permeability values, smaller dt values are required, which otherwise leads to dryness reaching values over 100%, which are nonphysical. The issue with the script not being able to reach the theoretical limit of 100% could not be resolved either. Possible reasons are that the time-stepping scheme is not accurate enough, and higher order schemes must be utilized, such that the truncation error is reduced. Another possible reason is that the formulation is bounded by a solution that results in the current limit, which was not straightforward to the eye if true.

The thought experiment of the jet formation is also an extremely limited model, taking into account the multitude of assumptionss such as laminar flow, constant uniform mass flow rate, and a geometrical approximation of the fluid flow. A reverse axisymmetric stagnation flow has not been modeled in the literature; thus, its existence is inherently questionable. The radial disk and cylinder that govern the estimated flow profile also pose strong physical inconsistencies, such as the sharp edges at the base of the cylinder. The dynamics of a free body of liquid inside a thin circular geometry could be very different than the estimate defined in the respective sub-section, which makes the obtained results certainly unrealistic.

The Rayleigh-Taylor instability considered in this thesis is a very specific phenomenon in the topic of multiphase flow, and although the calculated values do imply that it is a strong possibility, a definite conclusion cannot be made on whether they will exist or not. Relevant knowledge on RTIs in thin geometries or time-dependent accelerations was also not researched in the literature enough, which makes the foundations of the thought experiment questionable. The model also did not consider the effect of mass conservation, as the instabilities can only grow as long as there exists enough mass to support the growth. The resulting model is thus only a predictive element that gives a base understanding of the timescale of the possible movement of the liquid inside the vapor core.

The rewetting case investigated purely the two simple equations provided by the literature to define an estimated timescale of rewetting. These equations are developed for the rise in a capillary tube with a thin radius, and the mathematical model approximates the porous wick as a collection of capillary tubes. This is an inaccurate depiction of the possible configuration of a sintered-powder wick, as in real life, there are effects of varying pore sizes, as well as chaotic and discontinuous pathways. Although the results show that the timescale of rewetting is shorter than the leakout's, the dynamic effects of inertial movement must be considered. The provided equations consider a semi-infinite liquid pool that provides the necessary mass for impregnation. If the flow velocity of the liquid is fast enough, there is certainly a possibility that the inertia will inhibit imbibition into the porous medium, which was not considered.

The scope of these fluid dynamics scenarios is deeply flawed and strongly simplified. They lack certain crucial elements, such as the effects of mass conservation and temperature. The resulting expected thermal effects for each of the flow regimes were also put forward based on intuitive engineering knowledge and literature synthesis, rather than a validated physical basis. Thus, the conclusions made for the first section of the modeling of heat pipes subject to sloshing must be considered to have large uncertainties.

4.3.2. Computational Steady-State Modeling

An inevitable obstacle in computational modeling is the availability of computational power. Simply put, a computer equipped with higher computational capacity can handle more detailed calculations. The simplification from a 3D study into a 2D axisymmetric study was necessary for obtaining results in a time-efficient manner. However, this prohibited the study from investigating a more detailed set of results for the steady state operation, such as the minor effects of gravity and the possible dependence of the flow profile on the angular axis ϕ.

The geometry presented for both modeling sections disregarded the end caps of a real-life heat pipe, which are normally half-spherical geometries with a wick. Instead, geometries found in the literature were adopted, and although the effects of the end caps were expected to be minor, this was not verified in this thesis through an alternative model.

The model considered the solid phase of the porous wick to be made of perfect spheres of constant size with an even distribution, and the resulting pathways of constant radius capillary channels. The calculation of the effective properties also did not consider any uncertainties. Furthermore, the effective thermal conductivity and wick permeability were not calculated through the given relevant equations, but considered as known values from a specific heat pipe product in reality. These values have inherent uncertainties and could be wrong, especially in terms of the wick permeability, which was not considered. The temperature of the condenser section was also assumed to be constant at $20°C$ by a Peltier element in real life, which might not be exactly possible, and slight fluctuations could occur.

The model also did not consider the possible occurrence of an interface at a location other than the surface of the porous medium, and assumed that the interface between the liquid and vapor phases was at a thermodynamic equilibrium, leading to the utilization of the Clausius-Clapeyron equation. This is untrue, as a net flow of mass towards one phase from the other implies non-equilibrium conditions. The consideration of the total heat pipe length can justify overall mass conservation; however, local effects could be lost due to this assumption.

Surface tension pressure jump was assumed to exist only at the evaporator as well, and although there possibly exists a jump at the condenser section, it was not considered. This means that the full implementation of surface tension was not done in the thesis. Even though the results show a pressure difference between the two phases exists at the condenser section, this is not a result of taking into account the pressure jump in that section, and only indicates that the capillary limit is not reached.

Lastly, the validation model results of this thesis did not match the literature results of FH perfectly. Minor differences were observed for the pressure results, with good agreement of the curves obtained. However, the temperature results showed larger differences. The peak locations and the overall curves agree, yet the peak magnitudes did not agree to a full extent. It is noted that the results in the literature validation paper were also not fully visible and clear, and the obtained curve is an approximation. The qualitative comparison of the Mach number and temperature with respect to PA's results also has a certain discrepancy. Their results show a large change in the Mach number, inversely proportional to the temperature change. This thesis found that the Mach number did not change drastically compared to the change in temperature. These show that although the general results match well, there are still points that are possibly not resolved in the model of this thesis.

4.3.3. Coupling the Two Models

The two models built in the third chapter of the thesis could not be coupled due to time limitations. However, to start building a transient model, a Time-Dependent study in COMSOL was attempted. This transient model was unsuccessful and did not converge. A possible reason could be that the time and space discretization were not small enough, which could lead to a further computational limitation. The initial values chosen for the transient model were also taken from the converged steady-state values of the heat pipe. Yet, researchers such as PA show that the transient start-up of the heat pipe does not behave the way the steady-state model does. Thus, the initial values chosen for a transient study become ever more crucial, which has not been thoroughly investigated.

This transient model did not include any axial acceleration and aimed only to model the heat pipe operation with respect to time, such that a base time-dependent model was obtained. It is not fully known how to implement the effects of sloshing into the formulation of the heat pipe, and this requires a much deeper analysis before any models are built.

4.4. Recommendations for Future Work

The previous section provided considerable information on the limitations and shortcomings of the thesis, which correspondingly imply possible routes for future work. The following set of recommendations aims to build a more robust steady-state model and define ways to approach the dynamic effects of sloshing on heat pipes. Along with modeling recommendations, possible future experimental work is given, considering the most crucial findings of this thesis.

4.4.1. Steady State Modeling

Further studies that model heat pipe operation steady state are recommended to include:

1. A three-dimensional study of the heat pipe, coupled with the effect of gravity. Depending on the difference of the results between the 2D axisymmetric no-gravity simulation of this thesis and a full 3D simulation, a comprehensive conclusion of the dimensionality and the effects of gravity can be made.
2. A temperature-dependent surface tension pressure jump between the liquid and vapor phases at the interface, which models an important aspect of heat pipes. This fully captures the effect of surface tension and will also shed light on the method and importance of applying surface tension as a boundary condition.
3. An uncertainty study on the parameters that are effective properties, rather than directly inserting values. A range can be supplied for these parameters, and the most crucial variables are the effective thermal conductivity of the wick, which possibly varies between two orders of magnitude, and the permeability of the wick, which can vary drastically as well. This is a rigorous, but accurate, approach to defining the possible range of the heat pipe operation.
4. The more accurate modelling of the phase change phenomenon at the liquid-vapor interface, which can take into account the non-equilibrium thermodynamic behavior lost by the implementation of the Clausius-Clapeyron equation. This is a vast area of research, and it is not recommended as a first step, as the Clausius-Clapeyron equation is already a common and justifiably accurate solution to the modeling of phase change at the interface.

4.4.2. Effects of Sloshing

To develop a more robust and critical understanding of the effects of sloshing on heat pipes, it is recommended to first investigate:

1. A three-dimensional model that simulates the effects of sloshing of a liquid in a thin cylinder. This will provide a very intuitive and important understanding of the expected behavior of the liquid inside the vapor core when leakout occurs. The possible generation of a jet or growing RTIs can be observed. Furthermore, a flow regime that was not considered in this thesis could also occur, which makes this investigation ever more crucial.
2. The leakout phenomenon in different literature areas, such as soil science. Although a model or physical interpretation was not found in the literature that could support the claims of this thesis, relevant analogies could exist, which can prove to be useful.
3. The imbibition of a liquid into an enclosed gas-saturated porous medium, which essentially captures the rewetting phenomenon. This will give a deeper understanding of how the liquid phase replaces the gaseous phase in a wick, where the gas phase can exert a significant resistance, especially at small pore radii. This could affect the found timescale of rewetting, and reveal if rewetting is a realistic expectation or not.

Under the light of these improvements and investigations, the coupling of the two models can be attempted. To do so, a transient model must certainly be built. Literature comparisons and validations must also be conducted. This will reveal the start-up behavior of the heat pipe, which can provide crucial information on certain operating limits. The sloshing effects can be included through COMSOL Physics nodes if possible, or a decoupled model can be built, which connects and relates the liquid phase movement between the vapor core and wick domains.

4.4.3. Experimental Work

Along with the possible improvements to the modeling work done in this thesis, it is recommended that certain experiments be done. These are ordered in terms of the expected importance and impact:

1. **Sloshing of a rectangular liquid-saturated porous medium.** A rectangular cross-section of a porous medium can be made and enclosed in a glass container. By filling the porous medium with liquid, the base state of a heat pipe wick can be obtained. Connecting this setup to an accelerating stage will effectively result in a sloshing porous medium that is visible. The main problem of heat pipes is that they are enclosed on all ends with a metal, which makes observing the inner mechanisms impossible. With the glass container, at least the leakout behavior can possibly be showcased, with particle-image velocimetry (PIV) if needed. This can reveal behavior not thought of previously, or support the claims of this thesis.
2. **Investigation of the permeability of a sintered-powder copper wick.** This can be done through enclosing a porous medium, ad connecting the two open ends into a liquid flow chamber. Measure the pressure drop between the entrance and exit, and the volumetric flow rate, the terms can be inserted into the Darcy equation, and the permeability can be calculated. This experiment will be immensely helpful to understand the range of uncertainty of the possible values of the wick permeability. A reference study by Ababneh et. al. [71] can be investigated, which shows a drastic difference between Chi's formulation of sintered-powder wicks, and the real-life permeability value.
3. **Measuring the thermal conductivity of a sintered-powder wick.** A simple experiment of applying a certain heat rate on one end of a porous wick, and measuring the temperatures at two ends can analytically give the thermal conductivity of the wick. However, a more detailed experiment would require carefully saturating the wick with water, and redoing the experiment. Abnaneh et. al. conduct a laser flash experiment which agrees with the Maxwell equation in their case, given by Equation 2.13. However, it is noted that this is a more advanced test. Understanding the effective thermal conductivity of the wick is essential to defining the steady state operation and would result in a more accurate model.

It should also be pointed out that although the recommended future work topics cover the research area of heat pipes, the inner physics of heat pipes is made up of very popular but important, elementary physics, such as flow in porous media and phase-change phenomena. Further work in these areas will inevitably influence different research areas and generate deeply valuable scientific knowledge.

References

[1] URL: `https://www.precedenceresearch.com/thermal-management-market`.

[2] H. Xie, A. Ali, and R. Bhatia. "The use of heat pipes in personal computers". In: *ITherm'98. Sixth Intersociety Conference on Thermal and Thermomechanical Phenomena in Electronic Systems (Cat. No.98CH36208)*. 1998, pp. 442–448. DOI: `10.1109/ITHERM.1998.689600`.

[3] J. G. Mukuna and J. Gryzagoridis. "The effect of different working fluids and internal geometries on the efficiency of evacuated tube heat pipe solar collectors". In: *Journal of Energy in Southern Africa* 4 (2020), pp. 16–25. DOI: `10.17159/2413-3051/2020/v31i4a8480`.

[4] H. Jouhara et al. "The performance of a novel flat heat pipe based thermal and PV/T (photovoltaic and thermal systems) solar collector that can be used as an energy-active building envelope material". In: *Energy* 108 (2016), pp. 148–154. DOI: `https://doi.org/10.1016/j.energy.2015.07.063`.

[5] P. van Kappen et al. *High-tech industry in 2040 [White paper]*. 2024. URL: `https://www.tno.nl/en/newsroom/papers/high-tech-industry-2040/`.

[6] URL: `https://www.statista.com/statistics/1239480/united-states-leading-states-by-tech-contribution-to-gross-product/`.

[7] M. Khalili and M.B. Shafii. "Experimental and numerical investigation of the thermal performance of a novel sintered-wick heat pipe". In: *Applied Thermal Engineering* 94 (2016), pp. 59–75. ISSN: 1359-4311. DOI: `https://doi.org/10.1016/j.applthermaleng.2015.10.120`.

[8] A. Brusly Solomon, M. Sekar, and S.H. Yang. "Analytical expression for thermal conductivity of heat pipe". In: *Applied Thermal Engineering* 100 (2016), pp. 462–467. ISSN: 1359-4311. DOI: `https://doi.org/10.1016/j.applthermaleng.2016.02.042`. URL: `https://www.sciencedirect.com/science/article/pii/S1359431116301855`.

[9] G. Grover. URL: `https://patents.google.com/patent/US3229759A/en`.

[10] I. Voigt and W. -G. Drossel. "Experimental investigation of heat pipe performance under Translational Acceleration". In: *Heat and Mass Transfer* 58.2 (2021), pp. 209–219. DOI: `10.1007/s00231-021-03106-w`.

[11] J. Xiang et al. "Thermal Performances Investigation of Anti-Gravity Heat Pipe with Tapering Phase-Change Chamber". In: *Energies* 13.19 (2020). ISSN: 1996-1073. DOI: `10.3390/en13195036`.

[12] R. J. McGlen D. A. Reay. P. A. Kew. *Heat Pipes Theory, Design and Applications*. 6th ed. Elsevier, 2014. ISBN: 978-0-08-098266-3. URL: `https://www.sciencedirect.com/book/9780080982663/heat-pipes`.

[13] B. Zohuri. *Heat Pipe Design and Technology*. Springer, 2016. DOI: `https://doi.org/10.1007/978-3-319-29841-2`.

[14] X. Chen et al. "A review of small heat pipes for electronics". In: *Applied Thermal Engineering* 96 (2016), pp. 1–17. DOI: `https://doi.org/10.1016/j.applthermaleng.2015.11.048`.

[15] J. H. Jang et al. "Mathematical Modeling and Analysis of Heat Pipe Start-Up From the Frozen State". In: *Journal of Heat Transfer* 112.3 (1990), pp. 586–594. ISSN: 0022-1481. DOI: `10.1115/1.2910427`.

[16] A. Faghri. *Heat Pipe Science and Technology*. Global Digital Press, 2016. ISBN: 9780984276011. URL: `https://books.google.nl/books?id=5n2kAQAACAAJ`.

[17] Y. Suzuki and T. Inoue. "Heat Transfer Performance of Ammonia-Charged Oscillating Heat Pipe (Constant Heat Flux Heating Condition)". In: *Thermal Science and Engineering* 27.1 (2019), pp. 35–41. DOI: `10.11368/tse.27.35`.

[18] R. Pan et al. "Heat transfer characteristics analysis of heat pipe based on COMSOL". In: *Annals of Nuclear Energy* 204 (2024), p. 110549. ISSN: 0306-4549. DOI: `https://doi.org/10.1016/j.anucene.2024.110549`.

[19] David Reay, Peter Kew, and Ryan Mcglen. *Heat Pipes: Theory, Design and Applications: Sixth Edition*. Elsevier, Nov. 2013, pp. 1–251. URL: `https://www.sciencedirect.com/book/9780080982663/heat-pipes`.

[20] Roland Lenormand, Eric Touboul, and Cesar Zarcone. "Numerical models and experiments on immiscible displacements in porous media". In: *Journal of Fluid Mechanics* 189 (1988), pp. 165–187. DOI: `10.1017/S0022112088000953`.

[21] Yingxue Hu and Anindityo Patmonoaji and. "Experimental study on the displacement patterns and the phase diagram of immiscible fluid displacement in three-dimensional porous media". In: *Advances in Water Resources* 140 (2020), p. 103584. ISSN: 0309-1708. DOI: `https://doi.org/10.1016/j.advwatres.2020.103584`. URL: `https://www.sciencedirect.com/science/article/pii/S0309170819306839`.

[22] Changyong Zhang et al. "Influence of Viscous and Capillary Forces on Immiscible Fluid Displacement: Pore-Scale Experimental Study in a Water-Wet Micromodel Demonstrating Viscous and Capillary Fingering". In: *Energy & Fuels* 25.8 (2011), pp. 3493–3505. DOI: `10.1021/ef101732k`. eprint: `https://doi.org/10.1021/ef101732k`. URL: `https://doi.org/10.1021/ef101732k`.

[23] Xianxian Lyu et al. "Influence of Initial Oil Saturation, Injection Velocity and Wettability on Microscopic Characteristics in CO_2-Oil-Water Displacement System". In: *Rock Mechanics and Rock Engineering* (June 2025). DOI: `10.1007/s00603-025-04710-6`.

[24] Osamu Nishizawa et al. "Rock physics research with application to CO2 geological storage i: Co2 behavior in capillary-dominated region and effects of multi-scale heterogeneity on CO2 trapping". In: *BUTSURI-TANSA (Geophysical Exploration)* 69.2 (2016), pp. 127–147. DOI: `10.3124/segj.69.127`.

[25] Benzhong Zhao, Christopher W. MacMinn, and Ruben Juanes. "Wettability control on multiphase flow in patterned microfluidics". In: *Proceedings of the National Academy of Sciences* 113.37 (2016), pp. 10251–10256. DOI: `10.1073/pnas.1603387113`. URL: `https://www.pnas.org/doi/abs/10.1073/pnas.1603387113`.

[26] T. P. Cotter. "Theory of Heat Pipes". In: 1965. URL: `https://api.semanticscholar.org/CorpusID:134109471`.

[27] C A Bankston and H J Smith. *INCOMPRESSIBLE LAMINAR VAPOR FLOW IN CYLINDRICAL HEAT PIPES.* Tech. rep. Los Alamos Scientific Lab., N. Mex., Oct. 1972. DOI: `10.2172/4691028`. URL: `https://www.osti.gov/biblio/4691028`.

[28] {George Em} Karniadakis, Ali Beskok, and {Narayan R.} Aluru. *Microflows and Nanoflows Fundamentals and Simulation.* Interdisciplinary Applied Mathematics. Germany: Springer, 2005.

[29] en:user:cutler. URL: `https://commons.wikimedia.org/wiki/File:Spherical_meniscus.PNG`.

[30] Z. Hashin and S. Shtrikman. "A variational approach to the theory of the elastic behaviour of multiphase materials". In: *Journal of the Mechanics and Physics of Solids* 11.2 (1963), pp. 127–140. ISSN: 0022-5096. DOI: `https://doi.org/10.1016/0022-5096(63)90060-7`. URL: `https://www.sciencedirect.com/science/article/pii/0022509663900607`.

[31] J. C. Maxwell. *A Treatise on Electricity and Magnetism.* Cambridge Library Collection - Physical Sciences. Cambridge University Press, 2010. DOI: `https://doi.org/10.1017/CBO9780511709333`.

[32] Hideaki Imura, Hiroaki Kozai, and Kazusuke Takashima. "The Effective Thermal Conductivity of Screen Wicks". In: *Transactions of the Japan Society of Mechanical Engineers Series B* 54 (Oct. 1988), pp. 2905–2910. DOI: `10.1299/kikaib.54.2905`.

[33] Ming-Ming Chen and Amir Faghri. "An analysis of the vapor flow and the heat conduction through the liquid-wick and pipe wall in a heat pipe with single or multiple heat sources". In: *International Journal of Heat and Mass Transfer* 33.9 (1990), pp. 1945–1955. ISSN: 0017-9310. DOI: `https://doi.org/10.1016/0017-9310(90)90226-K`. URL: `https://www.sciencedirect.com/science/article/pii/001793109090226K`.

[34] A. Faghri and M. Buchko. "Experimental and Numerical Analysis of Low-Temperature Heat Pipes With Multiple Heat Sources". In: *Journal of Heat Transfer* 113.3 (Aug. 1991), pp. 728–734. ISSN: 0022-1481. DOI: `10.1115/1.2910624`. eprint: `https://asmedigitalcollection.asme.org/heattransfer/article-pdf/113/3/728/5553208/728_1.pdf`. URL: `https://doi.org/10.1115/1.2910624`.

[35] Mohammed Noorul Hussain and Isam Janajreh. "Numerical Simulation of a Cylindrical Heat Pipe and Performance Study". In: 2015. URL: `https://api.semanticscholar.org/CorpusID:156050713`.

[36] S. W. Chi. *Heat pipe theory and practice.* 1976.

[37] Vlodek R. Tarnawski and Wey H. Leong. "Advanced Geometric Mean Model for Predicting Thermal Conductivity of Unsaturated Soils". eng. In: *International journal of thermophysics* 37.2 (2016), pp. 1–42. ISSN: 0195-928X.

[38] Geoffrey Vaartstra et al. "Revisiting the Schrage Equation for Kinetically Limited Evaporation and Condensation". In: *Journal of Heat Transfer* 144.8 (May 2022), p. 080802. ISSN: 0022-1481. DOI: `10.1115/1.4054382`. eprint: `https://asmedigitalcollection.asme.org/heattransfer/article-pdf/144/8/080802/6882851/ht_144_08_080802.pdf`. URL: `https://doi.org/10.1115/1.4054382`.

[39] Van P. Carey. "Liquid-Vapor Phase-Change Phenomena: An Introduction to the Thermophysics of Vaporization and Condensation Processes in Heat Transfer Equipment, Third Edition". In: 2020. URL: `https://api.semanticscholar.org/CorpusID:93195474`.

[40] I.W. Eames, N.J. Marr, and H. Sabir. "The evaporation coefficient of water: a review". In: *International Journal of Heat and Mass Transfer* 40.12 (1997), pp. 2963–2973. ISSN: 0017-9310. DOI: `https://doi.org/10.1016/S0017-9310(96)00339-0`. URL: `https://www.sciencedirect.com/science/article/pii/S0017931096003390`.

[41] Manohar Bongarala et al. "A figure of merit to characterize the efficacy of evaporation from porous microstructured surfaces". In: *International Journal of Heat and Mass Transfer* 182 (2022), p. 121964. ISSN: 0017-9310. DOI: `https://doi.org/10.1016/j.ijheatmasstransfer.2021.121964`. URL: `https://www.sciencedirect.com/science/article/pii/S0017931021010693`.

[42] David T. Jamieson. "Condensation Coefficient of Water". In: *Nature* 202 (1964), pp. 583–583. URL: `https://api.semanticscholar.org/CorpusID:4158212`.

[43] Tor Ytrehus. "MOLECULAR-FLOW EFFECTS IN EVAPORATION AND CONDENSATION AT INTERFACES". In: *Multiphase Science and Technology* 9 (1997), pp. 205–327. URL: `https://api.semanticscholar.org/CorpusID:119631039`.

[44] C.A. Busse. "Theory of the ultimate heat transfer limit of cylindrical heat pipes". In: *International Journal of Heat and Mass Transfer* 16.1 (1973), pp. 169–186. DOI: `https://doi.org/10.1016/0017-9310(73)90260-3`.

[45] E. K. Levy. "Theoretical Investigation of Heat Pipes Operating at Low Vapor Pressures". In: *Journal of Engineering for Industry* 90.4 (1968), pp. 547–552. DOI: `10.1115/1.3604687`.

[46] Marcus B. D. "Theory and design of variable conductance heat pipes". In: (Apr. 1972). URL: `https://ntrs.nasa.gov/citations/19720016303`.

[47] Y. Y. Hsu. “On the Size Range of Active Nucleation Cavities on a Heating Surface”. In: *Journal of Heat Transfer* 84.3 (Aug. 1962), pp. 207–213. ISSN: 0022-1481. DOI: `10.1115/1.3684339`. eprint: `https://asmedigitalcollection.asme.org/heattransfer/article-pdf/84/3/207/5559712/207_1.pdf`. URL: `https://doi.org/10.1115/1.3684339`.

[48] A. Asias et al. “Instability of Heat Pipe Performance at Large Axial Accelerations”. In: *Journal of Heat Transfer* 129.2 (Apr. 2006), pp. 137–140. ISSN: 0022-1481. DOI: `10.1115/1.2402177`. eprint: `https://asmedigitalcollection.asme.org/heattransfer/article-pdf/129/2/137/5632494/137_1.pdf`. URL: `https://doi.org/10.1115/1.2402177`.

[49] M. C. Zaghdoudi and C. Sarno. “Investigation on the Effects of Body Force Environment on Flat Heat Pipes”. In: *Journal of Thermophysics and Heat Transfer* 15.4 (2001), pp. 384–394. DOI: `10.2514/2.6640`. URL: `https://doi.org/10.2514/2.6640`.

[50] S. K. Thomas, K. S. Klasing, and K. L. Yerkes. “The Effects of Transverse Acceleration-Induced Body Forces on the Capillary Limit of Helically Grooved Heat Pipes”. In: *Journal of Heat Transfer* 120.2 (May 1998), pp. 441–451. ISSN: 0022-1481. DOI: `10.1115/1.2824269`. eprint: `https://asmedigitalcollection.asme.org/heattransfer/article-pdf/120/2/441/5557888/441_1.pdf`. URL: `https://doi.org/10.1115/1.2824269`.

[51] MARK CHARLTON and W. BOWMAN. “Effect of transverse vibration on the capillary limit of a wrapped screen wick copper/water heat pipe”. In: *28th Thermophysics Conference* (1993). DOI: `10.2514/6.1993-2734`. eprint: `https://arc.aiaa.org/doi/pdf/10.2514/6.1993-2734`. URL: `https://arc.aiaa.org/doi/abs/10.2514/6.1993-2734`.

[52] Neil F. Huber and W. Jerry Bowman. “Longitudinal vibration effects on a copper/water heat pipe’s capillary limit”. In: *Journal of Thermophysics and Heat Transfer* 10.1 (1996), pp. 90–96. DOI: `10.2514/3.757`. eprint: `https://doi.org/10.2514/3.757`.

[53] J. E. Deverall. “The Effect of Vibration on Heat Pipe Performance”. In: (Oct. 1967).

[54] Amir Alaei, Morteza Hasanzadeh Kafshgari, and Shahab Kashani Rahimi. “A vertical heat pipe: An experimental and statistical study of the thermal performance in the presence of low-frequency vibrations”. In: *Heat and Mass Transfer* 49.2 (Aug. 2012), pp. 285–290. DOI: `10.1007/s00231-012-1057-z`.

[55] Rong-Horng Chen, Yung-Jen Lin, and Chi-Ming Lai. “The Influence of Horizontal Longitudinal Vibrations and the Condensation Section Temperature on the Heat Transfer Performance of a Heat Pipe”. In: *Heat Transfer Engineering* 34.1 (2013), pp. 45–53. DOI: `10.1080/01457632.2013.694776`. URL: `https://doi.org/10.1080/01457632.2013.694776`.

[56] J.-M. Tournier and M.S. El-Genk. “A heat pipe transient analysis model”. In: *International Journal of Heat and Mass Transfer* 37.5 (1994), pp. 753–762. ISSN: 0017-9310. DOI: `https://doi.org/10.1016/0017-9310(94)90113-9`. URL: `https://www.sciencedirect.com/science/article/pii/0017931094901139`.

[57] M A Merrigan, E S Keddy, and J T Sena. “Transient performance investigation of a space power system heat pipe”. In: Los Alamos National Lab., NM (USA). Dec. 1985. DOI: `10.2514/6.1986-1273`. URL: `https://www.osti.gov/biblio/5707982`.

[58] K. Baraya, J. A. Weibel, and S. V. Garimella. “Heat pipe dryout and temperature hysteresis in response to transient heat pulses exceeding the capillary limit”. In: *International Journal of Heat and Mass Transfer* 148 (2020), p. 119135. ISSN: 0017-9310. DOI: `https://doi.org/10.1016/j.ijheatmasstransfer.2019.119135`.

[59] M. Scholle and F. Marner. “A generalized Clebsch transformation leading to a first integral of NavierStokes equations”. In: *Physics Letters A* 380.40 (2016), pp. 3258–3261. ISSN: 0375-9601. DOI: `https://doi.org/10.1016/j.physleta.2016.07.066`. URL: `https://www.sciencedirect.com/science/article/pii/S0375960116305205`.

[60] A. J. Saddington, K. Knowles, and P. M. Cabrita. “Flow Measurements in a Short Takeoff, Vertical Landing Fountain: Parallel Jets”. In: *Journal of Aircraft* 45.5 (2008), pp. 1736–1743. DOI: `10.2514/1.32599`. URL: `https://doi.org/10.2514/1.32599`.

[61] F. A. Wohllebe and M. J. Siclari. “Fountain and Upwash Flowfields of Multijet Arrangements”. In: *Journal of Aircraft* 15.8 (1978), pp. 468–473. DOI: `10.2514/3.58392`. URL: `https://doi.org/10.2514/3.58392`.

[62] Vikas N. Bhargav et al. “Effect of relative jet momentum in supersonic dual impinging jets”. In: *Experiments in Fluids* 63.10 (Oct. 2022). DOI: `10.1007/s00348-022-03513-7`.

[63] Xiang Zhang and Ramesh K. Agarwal. “Numerical Simulation of Fountain Formation due to Normal and Inclined Twin-Jet Impingement on Ground”. In: *Fluids* 5.3 (2020). ISSN: 2311-5521. DOI: `10.3390/fluids5030132`. URL: `https://www.mdpi.com/2311-5521/5/3/132`.

[64] D.H. Sharp. “An overview of Rayleigh-Taylor instability”. In: *Physica D: Nonlinear Phenomena* 12.1 (1984), pp. 3–18. ISSN: 0167-2789. DOI: `https://doi.org/10.1016/0167-2789(84)90510-4`. URL: `https://www.sciencedirect.com/science/article/pii/0167278984905104`.

[65] Nazia Talat et al. “Phase field simulation of RayleighTaylor instability with a meshless method”. In: *Engineering Analysis with Boundary Elements* 87 (2018), pp. 78–89. ISSN: 0955-7997. DOI: `https://doi.org/10.1016/j.enganabound.2017.11.015`. URL: `https://www.sciencedirect.com/science/article/pii/S0955799717304009`.

[66] Pierre-Gilles de Gennes, Françoise Brochard-Wyart, and David Quéré. *Capillarity and wetting phenomena drops, bubbles, pearls, waves.* Springer New York, 2004. DOI: `https://doi.org/10.1007/978-0-387-21656-0`.

[67] D. Quéré. “Inertial capillarity”. In: *Europhysics Letters* 39.5 (Sept. 1997), p. 533. DOI: `10.1209/epl/i1997-00389-2`. URL: `https://doi.org/10.1209/epl/i1997-00389-2`.

[68] Y Cao and A Faghri. “Transient two-dimensional compressible analysis for high-temperature heat pipes with pulsed heat input”. In: *Numerical Heat Transfer, Part A: Applications; (USA)* 18:4 (Dec. 1989). ISSN: ISSN NHAAE. URL: `https://www.osti.gov/biblio/5773134`.

[69] Nat Thuchayapong et al. “Effect of capillary pressure on performance of a heat pipe: Numerical approach with FEM”. In: *Applied Thermal Engineering* 32 (2012), pp. 93–99. ISSN: 1359-4311. DOI: `https://doi.org/10.1016/j.applthermaleng.2011.08.034`. URL: `https://www.sciencedirect.com/science/article/pii/S1359431111004649`.

[70] Hui Li et al. “Numerical analysis on heat transfer of a complete anti-gravity loop-shaped heat pipe”. In: *International Journal of Heat and Mass Transfer* 109 (2017), pp. 824–834. ISSN: 0017-9310. DOI: `https://doi.org/10.1016/j.ijheatmasstransfer.2017.02.067`. URL: `https://www.sciencedirect.com/science/article/pii/S0017931016322037`.

[71] Mohammed Ababneh et al. “Thermal-Fluid Modeling For High Thermal Conductivity Heat Pipe Thermal Ground Planes”. In: *Journal of Thermophysics and Heat Transfer* 28 (Apr. 2014), pp. 270–278. DOI: `10.2514/1.T4107`.

A

Appendix I: Derivations of Equations

A.1. Ideal Gas Clausius-Clapeyron Equation

The state postulate states that a closed single-substance system is fixed by two intensive properties. This way, an extensive property can be defined as the total differential of the two intensive properties. Such a property is the molar entropy $s = (S/n)$, defined by the molar volume $v = (V/n)$ and temperature:

$$s = s(v, T)$$

Then, the total differential becomes:

$$ds = \left(\frac{\partial s}{\partial v}\right)_T dv + \left(\frac{\partial s}{\partial T}\right)_v dT$$

At equilibrium, the substance is at constant temperature and pressure; thus, the partial derivative of temperature is zero, leading to:

$$ds = \left(\frac{\partial s}{\partial v}\right)_T dv$$

The Helmholtz free energy equation states that:

$$df = sdT + Pdv$$

As for any equation in this form, it can be written that:

$$\left(\frac{\partial f}{\partial T}\right)_v = s$$

$$\left(\frac{\partial f}{\partial v}\right)_T = P$$

Furthermore, the symmetry of the second derivatives applies to functions with continuous second derivatives when the partial derivatives are mixed. Thus, it can be stated that:

$$\frac{\partial}{\partial T}\left(\frac{\partial f}{\partial v}\right)_T = \frac{\partial}{\partial v}\left(\frac{\partial f}{\partial T}\right)_v$$

Inserting s and P into the above equation, utilizing their partial derivative expressions, gives the Maxwell relation:

$$\left(\frac{\partial s}{\partial v}\right)_T = \left(\frac{\partial P}{\partial T}\right)_v$$

This expression can then be inserted into the ds equation, which results in:

$$ds = \left(\frac{\partial P}{\partial T}\right)_v dv$$

As the pressure and temperature of such a closed system are constant at equilibrium, the partial derivative can be written as a total derivative, and rearranging gives:

$$\frac{ds}{dv} = \frac{dP}{dT}$$

The Gibbs free energy equation states that:

$$dg = -sdT + vdP$$

As the system is closed, the Gibbs free energy of the system will not change at two different equilibrium positions, 1 and 2:

$$dg_1 = dg_2$$

$$-s_1 dT + v_1 dP = -s_2 dT + v_2 dP$$

By rearranging the terms, it can be shown that:

$$(s_2 - s_1)dT = (v_2 - v_1)dP$$

Stating that between the two equilibrium conditions, the change in molar entropy and molar volume are Δs and Δv, the above equation can be written as (also utilizing the ds/dv expression:

$$\frac{\Delta s}{\Delta v} = \frac{dP}{dT}$$

The molar enthalpy equation (derived from the first law of thermodynamics) is given by:

$$dh = Tds + vdP$$

At constant pressure and temperature during phase change, the molar enthalpy equation can be rewritten similarly:

$$ds = \frac{dh}{T}$$

$$\Delta s = \frac{\Delta h}{T}$$

In the case of phase change, the molar enthalpy is substituted by the molar latent heat L (J/mol) for a molar mass M (kg/mol) and latent heat of vaporization h_{fg} (J/kg) as:

$$\Delta h = L = Mh_{fg}$$

Thus, the Clausius-Clapeyron equation is given by:

$$\frac{dP}{dT} = \frac{L}{T\Delta v}$$

This equation relates the slope of the coexistence curve of the two phases to the molar change of volume between the phases, the equilibrium temperature, and the molar latent heat.

When the relevant phase change is between liquid and gas phases, most often, at temperatures way below the critical temperature of the substance, the molar volume of the gas phase is much larger than the liquid phase; thus, it can be stated that:

$$\Delta v = v_g - v_l \approx v_g$$

At such temperatures, if the pressure is also low, the ideal gas law can most often be applied:

$$v_g = \frac{RT}{P}$$

Substituting the two equations into the Clausius-Clapeyron equation gives:

$$\frac{dP}{dT} = \frac{LP}{RT^2}$$

Rearranging the term L/R into the specific gas constant ($R_s = R/M$) and latent heat of vaporization gives:

$$\frac{dP}{P} = \frac{h_{fg}}{R_s}\frac{dT}{T^2}$$

The latent heat of vaporization is a function of temperature; however, assuming that it is constant at low temperatures, the equation can be integrated between two points:

$$\int_{P_1}^{P_2} \frac{1}{P} dP \approx \frac{h_{fg}}{R_s} \int_{T_1}^{T_2} \frac{1}{T^2} dT$$

$$\ln\left(\frac{P_2}{P_1}\right) \approx \frac{h_{fg}}{R_s}\left(\frac{1}{T_1} - \frac{1}{T_2}\right) \tag{A.1}$$

This is the Clausius-Clapeyron equation for Ideal Gases at low temperatures and pressures, assuming constant latent heat of vaporization. Choosing point 1 such that the values P_1 and T_1 are known, one can approximate the pressure or temperature at point 2 on the coexistence curve with great accuracy, granted that the other value is known.

A.2. Maximum RTI Growth Rate

The squared growth rate of a Rayleigh-Taylor instability with surface tension is given by:

$$\Sigma^2 = \frac{\rho_l - \rho_v}{\rho_l + \rho_v} a(t) K - \frac{\sigma K^3}{\rho_l + \rho_v}$$

This equation, in the form $ax^3 - bx = y^2$, shows that the function has two roots, the local maximum and minimum. Taking the derivative with respect to K, $\frac{d\Sigma^2}{dK}$ is:

$$\frac{d\Sigma^2}{dK} = \frac{\rho_l - \rho_v}{\rho_l + \rho_v} a(t) - \frac{3\sigma K^2}{\rho_l + \rho_v}$$

To find the maximum of this equation, the left-hand side is set to zero, such that it is a second-order polynomial for K.

$$\frac{\rho_l - \rho_v}{\rho_l + \rho_v} a(t) = \frac{3\sigma K^2}{\rho_l + \rho_v}$$

$$K = \pm\sqrt{\frac{(\rho_l - \rho_v) a(t)}{3\sigma}}$$

It is also seen that the coefficient of the K term is negative in the first equation, which automatically means that the positive root is the local maximum due to the negative second derivative:

$$\frac{d^2\Sigma^2}{dK^2} = -\frac{6\sigma K}{\rho_l + \rho_v}$$

$$K = K_{max} = \sqrt{\frac{(\rho_l - \rho_v) a(t)}{3\sigma}}$$

Knowing that the instability only occurs for positive Σ^2, the maximum for the function is found as K_{max}. This root can then be inserted into the first equation to find the maximum growth rate as:

$$\Sigma_{max} = \sqrt{\frac{2\sigma}{\rho_l - \rho_v} \left[\frac{(\rho_l - \rho_v) a(t)}{3\sigma}\right]^{3/2}} \tag{A.2}$$

A.3. First-Order ODE for H(t)

For calculating the leakout, the equation system that must be solved is given by the following

$$L_{leak} = 2\sigma/\rho a(t) r_p$$
$$\frac{\mu u_l(t)\varepsilon[H(t) - L_{leak}]}{\kappa} + \frac{2\sigma}{r_p} = \rho a(t) H(t)$$
$$\dot{m}(t) = \rho_l u(t) 2\pi r_v [H(t) - L_{leak}]$$
$$\dot{H}(t) = \frac{\dot{m}(t)}{\varepsilon\rho\pi(r_w^2 - r_v^2)}$$

For the simplification of calculations, certain coefficients will be defined as

$$A = \mu\varepsilon/\kappa,\ B = 2\sigma/\rho r_p,\ C = 2\sigma/r_p,\ D = \rho,\ E = \rho 2\pi r_v,\ F = 1/\varepsilon\rho\pi(r_w^2 - r_v^2)$$

The above equation system can thus be rewritten as

$$A u_l(t) \left[H(t) - \frac{B}{a(t)}\right] + C = D a(t) H(t)$$
$$\dot{m}(t) = E u_l(t) \left[H(t) - \frac{B}{a(t)}\right]$$
$$\dot{H}(t) = F\dot{m}(t)$$

By defining a term $X(t) = u_l(t)[H(t) - B/a(t)]$, the system can be rewritten as

$$A X(t) = D a(t) H(t) - C$$
$$\dot{m}(t) = E X(t)$$
$$\dot{H}(t) = F\dot{m}(t)$$

The first equation can be rewritten as

$$X(t) = \frac{D a(t) H(t) - C}{A} = \frac{D}{A} a(t) H(t) - \frac{C}{A}$$

Which can be inserted into the second equation to find

$$\dot{m}(t) = \frac{DE}{A} a(t) H(t) - \frac{CE}{A}$$

This expression for $\dot{m}$ can be inserted to the third equation to give

$$\dot{H}(t) = \frac{DEF}{A} a(t) H(t) - \frac{CEF}{A}$$

By stating that $-DEFa(t)/A = p(t)$ and $-CEF/A = q(t)$, the first order ordinary differential equation for $H(t)$ can be defined as

$$\dot{H}(t) + p(t) H(t) = q(t)$$

Such equations have a known solution, which is found by defining the integration factor $I(t)$

$$I(t) = e^{\int p(t)dt}$$

Which is used for finding the solution to $H(t)$, with S being the constant of integration as

$$H(t) = \frac{1}{I(t)} \left(\int I(t)q(t)dt + S \right)$$

The solution strongly depends on the initial condition of $H(t)$, and the functions $I(t)$ and $q(t)$. In this problem, $q(t)$ is a constant, thus, it does not have to be integrated. However, in the case that $a(t)$ is a sinusoidal function, $H(t)$ does not have a closed-form solution. Defining $G = -DEF/A$ and $a(t) = Msin(wt)$ where w is the angular frequency, with a constant of integration N, the integration factor is

$$I(t) = e^{\int GMsin(wt)dt} = e^{-\frac{GM}{w}cos(wt)+N}$$

Which can be inserted into the solution of $H(t)$ as

$$H(t) = \frac{q}{e^{-\frac{GM}{w}cos(wt)+N}} \left(\int e^{-\frac{GM}{w}cos(wt)+N} dt + S \right) \tag{A.3}$$

The crucial point to notice here is that the integral

$$\int e^{-\frac{GM}{w}cos(wt)+N} dt$$

Results in a non-elementary integral, which can only be expanded through special functions such as a Bessel function. This means that although an analytical expression can be written, a closed-form solution that can give $H(t)$ at any time t does not exist. Thus, the solution requires the utilization of a numerical method.

B

Appendix II: MATLAB Script for Leakout

```matlab
r_p = 5e-5; % Pore Radius in the Wick [m]
r_w = 3.75e-3; % Radius of the Wick Domain [m]
r_v = 3.5e-3;  % Radius of the Vapor Core Domain [m]
l_t = 0.375; % Total Heat Pipe Length [m]
sigma = 0.072; % Surface Tension of Water [kg/s^2]
rho = 997; % Density of Water at Standard Conditions [kg/m^3]
mu = 1e-3; % Dynamic Viscosity of Water Standard Conditions [kg/(m*s)]
eps = 0.5; % Porosity of the Wick
dt = 1e-5; % Time Step Size [s]
t = 0.0001:dt:0.050; % Time Range of the Signal [s]
a = 400*sin(2*pi*(1/0.050).*t); % Acceleration Signal [m/s^2]
L = 2*gamma/rho./abs(a)/rp; % Calculating L_{leak} at any point in time
k_vec = logspace(-4,-13,1000); % Value Range for Permeability [m^2]
leakout_comparison = zeros(1,length(k_vec));
for f = 1:length(k_vec)
    % Initialize u, m, and H vectors
    H = 0.375*ones(1,length(a)+1);
    m = zeros(1,length(a)+1);
    u = zeros(1,length(a));
    k = k_vec(f);  % Define Permeability
    for i = 1:length(a) % Loop through the signal at each time step
        if L(i) < H(i) % If leakout exists, calculate leak velocity
            u(i) = rho*k*H(i)*abs(a(i))/mu/eps/(H(i)-L(i))-2*gamma*k/(
               mu*eps*r_p*(H(i)-L(i)));
        else % If there is no leakout, the leak velocity is zero
            u(i) = 0;
        end
        % Calculate delta m over delta t, giving time-discretized m_dot
        m(i+1) = m(i) - dt*(H(i)-L(i))*rho*2*pi*r_v*u(i);
        % Calculate time-discretized H_dot through m_dot
        H(i+1) = H(i)+(m(i+1)-m(i))/(eps*rho*pi*(r_w^2-r_v^2));
    end
    % Append total leaked mass into the comparison vector
    leakout_comparison(f) = m(end);
end
% Calculate the ratio of leaked mass with respect to the initial mass
total_dryout_ratio = -leakout_comparison/(eps*rho*pi*(r_w^2-r_v^2)*l_t)
```